# Miniaturized Pumps and Gauges for Ultra-High Vacuum Microsystems

by

Shiyang Deng

A dissertation submitted in partial fulfillment
of the requirements for the degree of
Doctor of Philosophy
(Electrical Engineering)
in the University of Michigan
2017

Doctoral Committee:

Professor Yogesh B. Gianchandani, Co-Chair
Assistant Research Scientist Scott R. Green, Co-Chair
Professor John E. Foster
Professor Mark J. Kushner

Shiyang Deng

kevindsy@umich.edu

ORCID Id: 0000-0002-9900-9229

# ACKNOWLEDGEMENTS

The work described in this dissertation would not have been possible without financial support from the Defense Advanced Research Projects Agency (DARPA) and Ferran Technology. I was also supported by a fellowship from the Department of Electrical and Computer Engineering at the University of Michigan.

Firstly, I am especially thankful to my advisor Prof. Yogesh Gianchandani for offering me the opportunity to work with him and with the talented people in his group. His extensive experience, endless passion, and unique perspective on research have guided and taught me through both my doctoral study and life in general. I am also heartily thankful to Dr. Scott Green. He always showed the greatest patience in explaining concepts and solving problems with me, no matter how trivial this might have looked to him. I would also like to thank the other committee members, Prof. Kushner and Prof. Foster, for their guidance and suggestions on this research and dissertation. Although they were not part of my committee, I benefitted from discussions with Dr. East in solving transmission line problems with regard to RF characterizations of my devices, and insightful modeling results of the RF electron traps provided by Dr. Markosyan enabled the experimental development of this work.

I would like to take this opportunity to thank my group members and 2001 office mates, including Tao, Xin, Yutao, Venkat, Yushu, Yu, Andy, Alex, Qisen, Jiqing, Neeharika, Ramprasad, Ryan, Jonathan, Robin, Tal, Stacey, Amin, Ali, Yi, Christopher, Farzad, Sajal, Donguk. Thank you all for the encouragement and support in both study and personal life.

At last, nobody has been more important to me in pursuing the Ph.D. than my parents. I would like to thank my mom for her endless love even when she is fighting against disease, and to my dad for taking care of her and supporting the whole family. Most importantly, I wish to express thanks to my one and only – Yuwei, who provides unending love and inspiration to me.

# TABLE OF CONTENTS

# LIST OF FIGURES

# LIST OF TABLES

# LIST OF ACRONYMS AND SYMBOLS

| | |
|---|---|
| 2D | two-dimensional |
| 3D | three-dimensional |
| $\boldsymbol{a}$ | acceleration of the electron |
| $A_p$ | electrode surface area |
| $\boldsymbol{B}$ | magnetic flux density |
| $B_c$ | critical magnetic flux density |
| $\boldsymbol{B_r}$ | remanent magnetic flux density |
| $B_t$ | tangential magnetic field at cathode surfaces in Design P.C |
| $B_{tran}$ | transition magnetic field between the LMF and the HMF |
| BAG | Bayard-Alpert gauge |
| $c$ | speed of light |
| $C$ | DC blocking capacitor |
| $C_{1\_p}$ | parasitic capacitance of the $L_1$ |
| $C_{L2}$ | capacitor in the equivalent circuit model of the $E^3$TM |
| $C_p$ | stray capacitor in the equivalent circuit model of the $E^3$TM |
| $C_{RFB}$ | capacitor in the equivalent circuit model of the ETM |
| CCG | cold cathode gauge |
| CCP | capacitively coupled plasma |
| CDG | capacitance diaphragm gauge |
| Collector 1 or Collector 2 | characterization electrodes in the ETM |

| | |
|---|---|
| CSAC | chip-scale atomic clock |
| CTE | coefficient of thermal expansion |
| $d$ | gap between two parallel RF electrodes |
| $D_a$ | anode inner diameter |
| DC | direct current |
| Design M.MF | a refined magnetron CCG design |
| Design M.O | a magnetron CCG design |
| Design M.S | a magnetron CCG design for a standard SHV feedthrough |
| Design P.A | a Penning cell CCG design with an array of anode cylinders |
| Design P.C | a Penning cell CCG design with curved cathode |
| Design P.E | a Penning cell CCG design with embedded magnets |
| Design P.F | a Penning cell CCG design with flattened case surfaces |
| Design P.I.1 or Design P.I.2 | Penning cell CCG designs with integrated case, magnetic return path, and cathodes |
| Design P.MF.1 | a refined Penning cell CCG design with better electron confinement and gauge manufacturability |
| Design P.MF.2 | a refined Penning cell CCG design with adjustable magnetic circuit |
| Design P.MF.3 | a refined Penning cell CCG design |
| DMLS | direct metal laser sintering |
| $E(t)$ or $\mathbf{E}$ | electric field |
| ECC | emission current control |
| ESD | electron stimulation desorption |
| ETM | electron trapping module |
| $E^3$TM | enhanced-efficiency electron trapping module |
| $F$ | Lorentz force on an electron |

| | |
|---|---|
| $f_0$ | series resonant frequency |
| $f_{0\_l}$ | lowered series resonant frequency |
| $f_{RF}$ | RF frequency |
| FEA | finite element analysis |
| FG | friction gauge |
| $g_m$ | gap between two magnets in Design P.I.1 or Design P.I.2 |
| $\boldsymbol{H}$ | magnetic field strength |
| HCG | hot cathode gauge |
| HMF | high magnetic field |
| HV | high vacuum |
| $I_D$ | gauge current |
| $I_e$ | electron current (electrons per second) |
| $I_{RFB,peak}$ | peak current through the RFB branch in the equivalent circuit of the ETM |
| $I_{C_{L2},peak}$ | peak current through the $C_{L2}$ in the equivalent circuit of the $E^3$TM |
| $k$ | gauge sensitivity |
| $k_{trap}$ | electron trapping confinement factor |
| $k_v$ | velocity of propagation of coaxial cable |
| $L$ | length of the coaxial cable |
| $L_1$ | frequency lowering inductor |
| $L_a$ | anode length |
| $L_G$ | DC shorting inductors in the bi-directional coupler |
| $L_{L2\_p}$ | stray inductor in the equivalent circuit model of the $E^3$TM |
| LMF | low magnetic field |
| $L_{RFB}$ | stray inductor in the equivalent circuit model of the ETM |

| | |
|---|---|
| $m_e$ | electron mass |
| MEMS | micro-electromechanical systems |
| M.MF.Sim | simulation model of Design M.MF |
| M.O.Sim | simulation model of Design M.O |
| M.S.Sim | simulation model of Design M.S |
| $n$ | gas density at a specific pressure |
| $n_e$ | electron density |
| $P$ | pressure |
| $P_c$ | collision probability between an electron and a gas molecule |
| $P_{fwd}$ | forward RF power |
| $P^{*}_{fwd}$ | ideal forward RF power |
| $P_{ref}$ | reflected RF power |
| $P_s$ | gauge startup pressure |
| $P_t$ | transmitted RF power |
| P.A.Sim | simulation model of Design P.A |
| PCM | photochemical machining |
| P.C.Sim | simulation model of Design P.C |
| P.E.Sim | simulation model of Design P.E |
| P.F.Sim | simulation model of Design P.F |
| P.I.1.Sim | simulation model of Design P.I.1 |
| P.I.2.Sim | simulation model of Design P.I.2 |
| P.MF.1.Sim | simulation model of Design P.MF.1 |
| P.MF.2.Sim | simulation model of Design P.MF.2 |
| P.MF.3.Sim | simulation model of Design P.MF.3 |

| | |
|---|---|
| Plate A or Plate B | additional metal electrodes in the ETM |
| PR | photoresist |
| PSDP | pressure-startup-delay-product |
| $q$ | fundamental charge |
| $r$ | radius of perforations on RF electrodes in the ETM and $E^3$TM |
| $r_a$ | anode radius |
| $R$ | resistance in parallel with the DC blocking capacitors |
| $R_{1\_p}$ | parasitic resistance of the $L_1$ |
| $R_c$ | cycloidal motion radius of trapped electrons |
| $R_{c,e}$ | electron Larmor radius |
| $R_{c,i}$ | ion Larmor radius |
| $R_{L2\_p}$ | stray resistor in the equivalent circuit model of the $E^3$TM |
| $R_{RFB}$ | stray resistor in the equivalent circuit model of the ETM |
| RF | radio frequency |
| RFA or RFB | RF electrodes in the ETM |
| RFT-CHIP | radio frequency trapped chip-scale helium ion pump |
| $S_{gas}$ | ionization rate of a specific gas (ions per second) |
| SHV | safety high voltage |
| SSEP | steady state electrode potential |
| $t$ | time |
| $T_c$ | thickness of the magnetic return path in Design P.I.1 or Design P.I.2 |
| $t_e$ | thickness of RF electrodes in the ETM and $E^3$TM |
| $T_e$ | electron temperature |
| $T_w$ | wall thickness between the magnets and anode in Design P.I.1 or Design P.I.2 |

| | |
|---|---|
| TCG | thermal conductivity gauge |
| UHV | ultra-high vacuum |
| $v$ | average electron velocity |
| $v_0^*$ | ideal initial velocity of the electron enters the RF electron trap |
| $v_{0,i}$ | initial velocity of the electron enters the RF electron trap |
| $V_A$ | anode biasing voltage |
| $V_{Cha}$ | electrode potential at chassis |
| $V_{Cha\_rss}$ | reference steady state electrode potential at chassis |
| $V_{Cha\_ss}$ | steady state electrode potential at chassis |
| $V_{Col1}$ | electrode potential at Collector 1 |
| $V_{Col1\_rss}$ | reference steady state electrode potential at Collector 1 |
| $V_{Col1\_ss}$ | steady state electrode potential at Collector 1 |
| $\overline{v}_e$ | average thermal speed of electron at $T_e$ |
| $v_i$ | ionization rate per electron |
| $V_K$ | cathode biasing voltage |
| $V_{L,peak}$ | peak RF voltage across the ETM |
| $V_{L2,peak}$ | peak RF voltage across the $E^3$TM and the series inductor $L_1$ |
| $V_m$ | magnetic scalar potential |
| $V_p$ | probe or electrode potentials |
| $V_{Pro}$ | probe potential |
| $V_{Pro\_ss}$ | steady state probe potential |
| $V_{Pro\_rss}$ | reference steady state probe potential |
| $\lvert V_{RF}\rvert$ | magnitude of the RF voltage |
| $\lvert V_{RF}^*\rvert$ | magnitude of the RF voltage to initiate an ideal RF electron trap |

| | |
|---|---|
| $V_S$ | source voltage from a high voltage power supply |
| WYDE CDG | Ferran-Tech WYDE capacitance diaphragm gauge |
| $x$ | traveling distance of an electron |
| $x(t)$ | electron position at time $t$ |
| $x_0^*$ | ideal initial position of the electron in the RF electron trap |
| $x_{0,i}$ | initial position of the electron in the RF electron trap |
| $Z_0$ | characteristic impedance of the coaxial cable (50 Ω) |
| $Z_{in}$ | impedance of the module (ETM or E$^3$TM) along with the cable |
| $Z_L$ | impedance of the ETM |
| $Z_{L2}$ | impedance of the E$^3$TM |
| $Z_{L2\_150}$ | impedance of the E$^3$TM with the 150 nH series inductor |
| $Z_{L2\_330}$ | impedance of the E$^3$TM with the 330 nH series inductor |
| $\eta$ | charge to mass ratio of the electron |
| $\beta$ | probability of a gas ionization collision |
| $\lambda$ | mean free path |
| $\sigma_i$ | electron ionization cross section of a specific gas at an electron energy level |
| $\phi$ | phase of RF signal |
| $\Gamma$ | voltage reflection coefficient |
| $\varepsilon_0$ | permittivity of vacuum |
| $\varepsilon_r$ | relative permittivity |
| $\rho_v$ | space charge density |
| $\mu_0$ | vacuum permeability |
| $\mu_r$ | relative permeability |

# ABSTRACT

For devices such as chip-scale atomic clocks (CSACs) and capacitance diaphragm gauges (CDGs) that require compact vacuum environments at sub-µTorr or even nTorr vacuum levels, the stability of the vacuum is generally of great importance. Miniaturized pumps and gauges can play critical roles in actively maintaining and monitoring chip-scale vacuum environments. Toward this end, this thesis describes two types of elements: (i) miniaturized radio frequency (RF) electron traps for magnet-less ion pumps, and (ii) miniaturized cold cathode gauges to measure vacuum levels.

In traditional ion pumps, electrons are confined by crossed electric and magnetic fields in a Penning electron trap in order to extend electron lifetime and promote ionizing electron-gas collisions. However, CSACs are sensitive to magnetic fields. This thesis describes a magnet-less RF electron trap to replace the Penning electron trap for CSAC applications. The RF electron trap was investigated in two generations. The first-generation formed a 0.7 $cm^3$ electron active volume. An RF signal of various power levels and at 143.6 MHz was applied across two RF electrodes spaced 0.7 cm apart to trap electrons that were supplied by an electron gun. It was shown experimentally that the steady state electrode potentials (SSEPs) on electrodes near the trap became more negative after applying certain RF power levels, which indicated higher electron density within the trap. The measured trends aligned well with the modeled trends. The electron density

within the trap was estimated to be 3 x $10^5$ $cm^{-3}$, which was ~1000x the electron density in the electron beam as it exited the electron gun.

The second-generation RF electron trap was refined in structure to have 10x finer perforated RF electrodes, a higher trap-to-device volume ratio, simplified electrode composition and RF characteristics, and a tunable operating frequency. The experimental results showed that the electron density was 2.24 x $10^6$ $cm^{-3}$ in the center of the RF electron trap when the trap was operated at 96.9 MHz with a transmitted RF power of 0.273 W. Both RF electron traps represent successful demonstrations of compact new structures for trapping electrons without using a magnetic field.

Miniaturized vacuum gauges allow monitoring of pressure levels in compact systems without introducing significant performance-degrading dead volume. This thesis describes new designs for miniature cold cathode gauges (CCGs). Seven preliminary CCG designs with an internal volume of less than 1 $cm^3$ were developed. Four of these preliminary CCG designs were shown via analysis to be capable of spiraling electrons with a direct current (DC) operating voltage lower than 1000 V. Four CCG designs were further refined to analytically demonstrate better electron spiraling capability while also fulfilling manufacturability requirements. A magnetron design (Design M.S) was fabricated with three-dimensional (3D) printing techniques for performance characterization. The Design M.S could start at a pressure as low as 10.5 μTorr when the power supply $V_S$ to the cathode was biased at –750 V, and the gauge current was repeatable from $10^{-3}$ Torr to $10^{-5}$ Torr at various $V_S$ from –750 V to –3000 V. The estimated average magnetic flux density was 0.2 T in Design M.S. The miniaturized CCGs are at least 10x smaller than commercially available CCGs, e.g., the MKS Series 903 inverted magnetron transducer, which has an internal volume of 15 $cm^3$.

# CHAPTER 1:

## INTRODUCTION

Miniaturized vacuum encapsulation is essential for various micro-electromechanical systems (MEMS) that are required to operate in high vacuum (HV, $10^{-3}$ Torr to $10^{-9}$ Torr) or even ultra-high vacuum (UHV, $10^{-9}$ Torr to $10^{-12}$ Torr), such as inertial sensors, micro resonators, and field emitter arrays [Pri12, Spi91, Vel10, Zoo92]. The performance of these microsystems is greatly affected by the stability of the vacuum environment. For example, the quality factor and the resonant frequency of a MEMS gyroscope and micro resonators depend on the package pressure [Gor09, Tru11]. Thus, on-board vacuum maintenance and monitoring are attractive topics for microsystems that require very precise control over package pressure over long periods of deployment. In macro-scale HV and UHV systems, ionization-based vacuum pumps and gauges are widely used for gas pumping and vacuum monitoring [Aud87, Sak94, Wel01]. This work explores the possibilities of miniaturizing the ionization-based vacuum pumps and gauges for microsystems that work in HV and UHV.

In Section 1.1, the motivation and previous efforts to develop miniaturized vacuum pumps are presented. Section 1.2 does the same for miniaturized vacuum gauges. Section 1.3 describes the focus and goals of this work. In Section 1.4, the structure of this dissertation is discussed.

## 1.1 Miniaturized Vacuum Pumps

### 1.1.1 Motivation and Prior Work

Miniaturized atomic microsystems that are based on the laser cooling technique, which are the subject of ongoing research, have especially rigorous vacuum requirements: the chamber in which atoms are trapped and cooled requires UHV in order to reduce the rate of spurious collisions between vapor phase atoms (e.g. rubidium) and background gas particles [Can06, Bor02, Kit11, Kna08, Jau12, Lut04, Mul09, Nel12, Sch14, Sch16]. These collisions may perturb the trapped cold atoms, influencing measurement sensitivity and resolution. The conventional approach for providing UHV is to use extremely low leakage packaging with enclosed getters [Del16, Mau13, Spa03, Spa10, Wu12]. However, the pressure of even a hermetically sealed package can significantly increase over time due to outgassing from interior surfaces of the vacuum cavity. Furthermore, helium from the ambient atmosphere permeates all packages and is not absorbed by typical getters, and this eventually compromises the vacuum [Kim09, Sak94]. This limits the useful life of devices, particularly when the vacuum cell is small in volume.

In contrast to conventional vacuum maintenance methods, a miniaturized active pump can potentially provide a stable vacuum environment at the chip scale. However, UHV levels are not practically realized by chip-scale mechanical roughing pumps [Bes12, Zho11], as the compressibility of the gas is too high for such pumps to operate efficiently in this pressure regime. Such vacuum levels are also not easily met by chip-scale thermal transpiration (Knudsen) pumps [An14], as the required dimensional scaling of molecular flow channels at low pressures works against the technique. However, a miniaturized ion pump holds significant promise for meeting UHV requirements.

Miniaturized ion pumps typically utilize a Penning cell structure similar to that used in commercial macro-scale ion pumps [Aud87, Sak94, Wel01]. The Penning cell structure consists of three electrodes (an anode and two cathodes) and magnets. The titanium cathodes are planar and are placed perpendicular to the long axis of the cylindrical-shaped anode, as shown in Fig. 1-1. The magnetic field is perpendicular to the cathode plates, and oriented along the axis of the anode cylinder. Applying a large electric field between the anode and cathodes generates high-energy electrons following electron emission from the cathodes. These electrons are confined to move in long spiral trajectories inside the cylindrical anode under crossed electric and magnetic fields. The helical motion of the electrons produces a long path as the electrons traverse from cathode to anode, which increases the probability of an electron colliding with gas molecules for gas ionization. Ions are accelerated toward the titanium cathodes with sufficient energy to sputter titanium atoms. The reactive background gas molecules (oxygen and nitrogen, for example) are chemically adsorbed by the gettering action of sputtered titanium powder on the cathode while inert gas molecules (such as helium and argon) are ionized and implanted into the cathodes. Miniaturized chip-scale Penning cells for sputter-ion pumping have been reported to operate at pressures as low as 1.5 µTorr in a 2.5 $cm^3$ package [Gre13]. This previously reported pump reduced pressure to <10 mTorr from a starting pressure of 115 mTorr in ≈4 hours of operation with 450-600 V applied across the device, and with a 100-250 mW power consumption. A similar approach demonstrated pumping at pressures as low as 4 µTorr [Grz14].

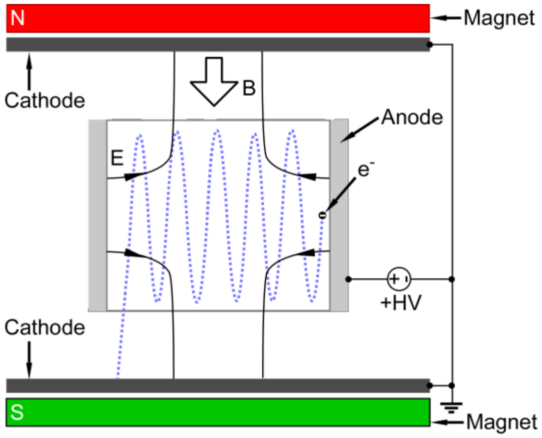

Figure 1-1: Schematic of the Penning cell electron trap, which requires crossed electric and magnetic fields to trap electrons.

In miniaturized ion pumps, the gas ionization efficiency is the most critical parameter that determines the pumping speed because only gaseous ions can be pumped. The ionization rate of a specific gas $S_{gas}$ (ions per second) can be roughly estimated with [Lie94, Lie04, Pan90]:

$$S_{gas} = I_e \cdot P_c \cdot v_i \tag{1-1}$$

$$P_c = 1 - e^{-\frac{x}{\lambda}} \tag{1-2}$$

$$v_i = n\sigma_i v \tag{1-3}$$

where $I_e$ is the electron current in electrons per second, $P_c$ is the collision probability between an electron and a gas molecule, $v_i$ is the ionization rate per electron, $x$ is the traveling distance of a single electron, $\lambda$ is the mean free path of the electrons, $n$ is the number of gas molecules per unit volume ($cm^{-3}$) at a specific pressure, $\sigma_i$ is the electron-ionization cross section of that specific gas at an electron energy level for the electron having $v$, the average electron velocity.

In order to effectively employ miniaturized ion pumps for active pumping of atomic microsystems, such as chip-scale atomic clocks, several challenges still need to be addressed. First, the mean free paths for electrons and gas molecules are typically on the order of hundreds of kilometers at nTorr pressures, which mean only 10 parts-per-billion of electrons will collide with a gas molecule before being lost to the pump surface in a millimeter scale cavity as suggested by Equation (1-2) [Hal81, Lie04]. One way to achieve efficient gas ionization is to configure the miniaturized ion pumps with a very high rate of electron emission to dramatically increase the $I_e$ in Equation (1-1). There have been a few efforts to develop such miniaturized ion pumps that can emit electrons at high rates [Bas16, Fom14]. Fomani *et al.* proposed a high vacuum pump that was intended to increase ion production by producing very large electron currents from field emitter arrays [Fom14]. Another effort utilized a set of electrodes that were biased at certain direct current (DC) voltages to modestly lengthen the trajectories of electrons emitted from field emitter arrays, which is similar in concept to the Orbitron pump [Bas16]. However, most of the highly energetic electrons from the high-density electron streams collided with the internal pump surfaces, causing the pressure to rise dramatically inside the vacuum packages due to electron-induced gas desorption.

As an alternative, high gas ionization efficiency can be achieved with long-lived electrons, such as the Penning cell structure mentioned above. The major advantage of the Penning cell pump is that the probability of collision between electrons and gas molecules is greatly enhanced to allow the reduction of $I_e$. However, the second challenge is associated with this Penning cell structure based on magnetic electron trapping. Atomic systems that rely on specific spacing of energy levels are sensitive to magnetic fields, as these alter the quantum states of atoms [Sch16]. As a result, in atomic inertial microsystems, the final atomic state that is measured is altered by conditions unrelated to the size of the inertial field. This sensitivity to magnetic fields makes the Penning cell structure less desirable for atomic microsystems because of the typically large magnitude of the magnetic fields required for electron trapping (e.g., 0.2 T), and the challenges associated with shielding such fields and minimizing field gradients [Gre13]. One more challenge is associated with the pumping of inert gases like helium because the gettering action does not assist and gases with small nuclei can easily permeate into the sealed cell driven by a concentration difference [Kim09, Sch12]. Therefore, miniaturized magnet-less ion pumps with the capability to pump inert gases are of high importance for atomic microsystems that require a stable UHV environment.

### 1.1.2 Radio Frequency (RF) Trapped Chip-Scale Helium Ion Pump (RFT-CHIP)

Motivated by these needs, a radio frequency (RF) trapped chip-scale helium ion pump (RFT-CHIP) is conceptually introduced as shown in Fig. 1-2. This RFT-CHIP utilizes an RF electron trap and a triode configuration to produce a miniaturized ion pump (~1 $cm^3$) capable of magnet-less ionization and pumping of both reactive and inert gases at nTorr levels.

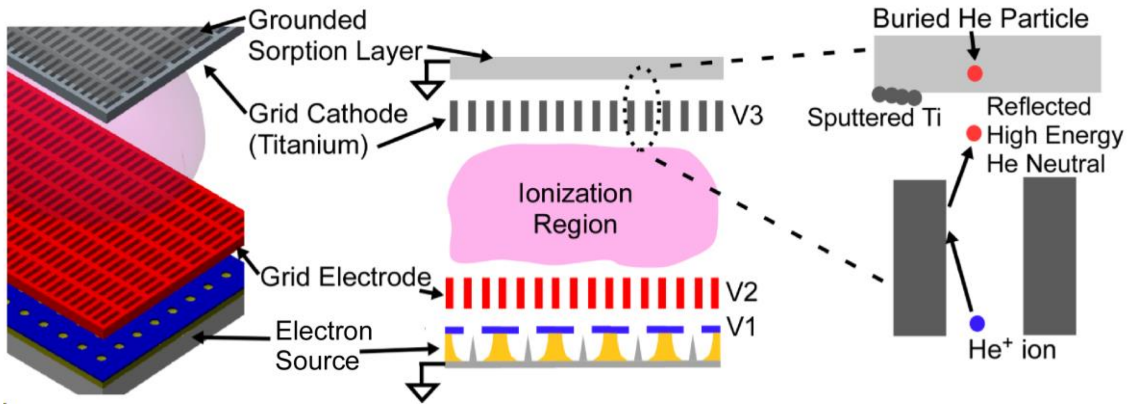

Figure 1-2: RFT-CHIP concept: 3D model (left), two-dimensional (2D) schematic (center), detailed view of grid cathode (right). The electron source (commercially available electron gun system or integrated field emitter array) provides electrons, which are trapped in the ionization region by an RF voltage between the grid electrode and grid cathode. The electrons ionize gas molecules, which are then accelerated into the grid cathode via a pulsed negative voltage. The ions collide with the cathode at shallow angles, and are reflected as neutral particles buried in the sorption layer backing the grid cathode. The titanium cathode is also sputtered by this action, which further buries the neutrals and getters reactive molecules from the environment.

There are three consecutive stages for the operation of the RFT-CHIP: the electron generation stage, the electron trapping and gas ionization stage, and the gas pumping and sorption stage. Electrons can be generated by a commercially available electron gun system or an integrated electron source [Spi91, Vel10]. The generated electrons are then trapped between two grid electrodes via application of an RF voltage. The electrons oscillate in this region, and the extended trajectory and kinetic energy are sufficient for ionizing the gas molecules. Ions build up in the ionization region while the RF voltage is applied, as the high frequency electric fields do not tend to appreciably accelerate the relatively massive ions. After sufficient ionization time, the RF voltage is switched off, and the ions are accelerated into the grid cathode (and away from the electron source) using a DC voltage. The ions collide with the surfaces of the cathode at shallow angles. This collision angle results in neutralization and reflection of the ions, and the now neutral particles continue on their reflected trajectory unaffected by electric fields. The high-energy neutral particles are buried into the sorption layer. The grid cathode is to be made from a sputterable getter (titanium); the sputtering action of any heavy ions bombarding the cathode will not only further bury neutral particles but also result in titanium gettering of reactive molecules that may present in the pump chamber [Sak94]. Importantly, the cathode is to be biased at a negative voltage with respect to the sorption layer and the base of electron source during ion acceleration; this results in ions being attracted only to the cathode and away from both the electron source and the gas particles buried in the sorption layer.

There are several specific innovations of the RFT-CHIP, which are mainly enabled by a miniaturized RF electron trap. First, the magnet-less RF electron trap can achieve a higher probability of electron-gas collisions as the electron trajectories are elongated significantly, which requires a much lower electron current while still generating a sufficient ionization rate. Second, the RF-trapped electrons are energized via the applied RF voltage for gas ionization. Third, the inert gas pumping is enhanced with the slotted grid cathode for generating high-energy neutrals to bury into the integrated sorption layer.

## 1.2 Miniaturized Vacuum Gauges

### 1.2.1 Motivation

The Ferran-Tech WYDE Capacitance Diaphragm Gauge (WYDE CDG™) provides precise vacuum measurements for use in critical semiconductor manufacturing processes (Fig. 1-3) [Fer17]. This gauge capacitively measures the deflection of a diaphragm against a sealed reference vacuum chamber that provides the reference vacuum for the CDG. The operating range of the gauge extends from 760 Torr to <$10^{-6}$ Torr. The sealed vacuum chamber, following the activation of the encapsulated getter, is expected to have vacuum levels in the range of $10^{-9}$ Torr to $10^{-10}$ Torr. If the seals or diaphragm are somehow compromised, the integrity of the reference chamber vacuum may be threatened. In this case, the CDG may provide inaccurate vacuum measurements, which could compromise processes, require unscheduled maintenance of the CDG, and cause interruption of ongoing processes and huge economic losses to semiconductor electronics manufacturers.

Figure 1-3: Ferran-Tech WYDE CDG™ [Fer17].

In order to address this problem, miniaturized vacuum gauges are proposed as an important component for the next generation CDG. These gauges would be used to monitor the pressure in the reference vacuum chamber, and to measure the loss of vacuum over time in a manner that allows the leakage rate to be estimated. The target dynamic range of the gauges is $10^{-3}$ Torr to $10^{-9}$ Torr, which is within the HV range. Thermal conductivity gauges (TCGs), such as the Pirani gauge, and friction gauges (FGs), such as the piezoelectric tuning fork oscillator, are not suitable to work at these vacuum levels. The thermal conductivity through the gas is very small in this pressure range, limiting the sensitivity and resolution of TCGs [Cha05, Wil04]. The gas damping induced resonance shift of FGs is negligible, because the gas damping is minimal in this pressure range [Kob93]. The most effective method for measuring pressure in the identified vacuum range is using ionization gauges, in which energetic electrons ionize gas molecules to produce an ion current that is proportional to the pressure.

### 1.2.2 Prior Work

Ionization gauges are broadly divided into two categories. One is the hot cathode gauge (HCG); the other is the cold cathode gauge (CCG) [Pea91]. In an HCG, electrons are constantly supplied by thermionic emission from a hot filament heated up to at least 1000 °C, and the emitted electrons are accelerated in a biased electric field to gain kinetic energy for gas ionization [Pea91]. In a CCG, the initial electrons are produced by background cosmic radiations or field emissions. Crossed electric and magnetic fields are built across the gauge to circulate and energize these initial electrons for gas ionization, and to maintain a self-sustained electron trap with the secondary electrons produced during the ionizations [Ken00]. The gauge outlines of several typical HCGs and CCGs are conceptually shown in Fig. 1-4.

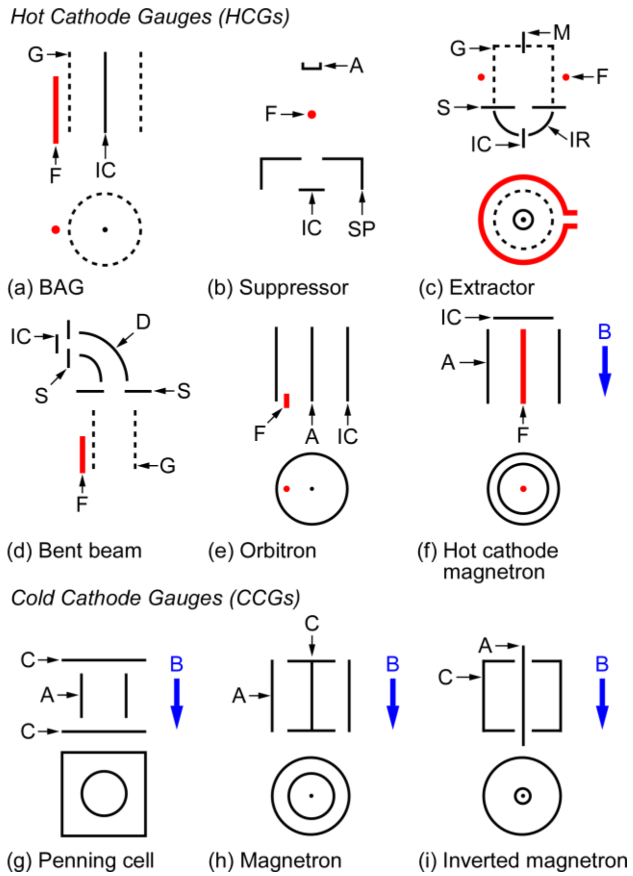

Figure 1-4: The gauge outlines of typical ionization gauges. The hot cathode gauges (HCGs): (a) Bayard-Alpert gauge (BAG), G: grid, F: filament, IC: ion collector; (b) Suppressor type, A: anode, SP: suppressor; (c) Extractor type, M: modulator, IR: ion reflector, S: shield; (d) Bent beam type, D: deflector; (e) Orbitron type; (f) Hot cathode magnetron type, B: magnetic field. The cold cathode gauges (CCGs): (g) Penning cell type, C: cathode; (h) Magnetron type; (i) Inverted magnetron type [Bay50, Hel66, Hob58, Laf61, Met51, Mou64, Pen40, Red59, Red66].

The most widely used HCG is the Bayard-Alpert gauge (BAG). It consists of a fine grid with a thin wire ion collector in the center; both are more positively biased to the filament that is located outside the grid to supply the electrons [Bay50]. There are two major issues that limit the lowest detectable pressure of the BAG, as well as other types of HCGs. First, highly energized electrons may collide at the grid surface to cause electron stimulation desorption (ESD) [Red65]. This ESD can lead to the electronic desorption of grid contamination, which results in an ion current to the ion collector that is not related to the pressure [Red63]. Second, the BAG has a serious X-ray effect [Pea91]. Photons can be produced at the grid when electrons strike the grid. As some of the photons arrive at the ion collector, photoelectrons can be emitted to result in an electron current that has no dependence on pressure. Both the ESD and X-ray effects are thus pressure independent, and therefore limit the minimum measurable pressure of the HCGs.

To extend the minimum measurable pressure level, extensive research efforts have focused on addressing these two limitations through structural refinements. A modulated BAG was developed by Redhead [Red60, Red65]. Additional metal wire is placed near and in parallel with the center ion collector of the conventional BAG to suppress the impact-induced ion current by modulating the ion current that truly represents the chamber pressure. Metson proposed a suppressor type HCG to suppress the X-ray induced photoelectron current at the ion collector by placing a negatively biased suppressor electrode between the ionization region and the ion collector [Met51]. In 1966, more complicated HCGs such as the bent-beam type and extractor type were constructed to address the ESD and the X-ray effects [Hel66, Red66]. These HCGs have an externally located ion collector to allow a more flexible electrode arrangement. As these two issues are related to thermionic emitted electrons, HCGs with electron trajectory elongation capabilities are built to reduce the number of the emitted electrons. Mourad proposed an Orbitron type HCG [Mou64]. Electrons are orbited around the center anode inside the cylindrical ion collector. Lafferty developed a hot-cathode magnetron type HCG to use crossed electric and magnetic fields to trap the emitted electrons [Laf61].

The two typical CCGs are the Penning cell type and magnetron type; both consist of an anode, a cathode, and a magnetic circuit [Gre13, Pen37, Pen40, Red59]. An electric field is developed across the anode and cathode when the cathode is grounded and the anode is biased at $V_A$. The magnetic field provided by the magnetic circuit is directed along the axis of the cylindrical anode. Only the electron trajectory is extended by the crossed electric and magnetic fields because the electron Larmor radius $R_{c,e}$ is smaller than the typical gauge geometry, 2 cm (e.g., $R_{c,e}$ is 0.05 cm when the magnetic field is 0.2 T and the $V_A$ is 600 V) [Abo12]. Typically, the ion Larmor radius $R_{c,i}$ is longer than the gauge geometry; for example, $R_{c,i}$ is 13 cm for a $Ar^+$ ion when the magnetic field is 0.2 T and the $V_A$ is 600 V [Abo12]. The ionized gas molecules are drawn to the cathode without delay because the ions are much heavier than the electrons so the ions are minimally affected by the magnetic field. Another CCG was proposed by Hobson, called the inverted magnetron type [Hob58]. The structure is similar to the magnetron type, but the electrical biasing is inverted as compared to the magnetron type.

The CCGs are more suitable to integrate with the next generation CDG than the HCGs, because ESD and X-ray effects are pressure dependent in CCGs, and thus CCGs maintain sensitivity at lower pressures than HCGs [Ken97]. In addition, CCGs have other advantages over HCGs in applications which require monitoring a compact vacuum chamber in a low power system. First, the power consumption of CCGs is usually at milliwatt or even microwatt levels, whereas HCGs are operated at watt levels [Hob80]. Second, the outgassing rate of CCGs is typically several orders of magnitude lower than that of HCGs [Red03]. This lower outgassing rate is critical in compact vacuum chambers, as the outgassing of the gauge during operation has a pronounced effect on the pressure level in small chambers. Both of these traits are expected when comparing the electron generation methods of CCGs and HCGs. The filament has to be hot enough to start the thermionic emission in HCGs, which requires substantial power and enhances temperature-induced gas desorption from the surrounding environment. Although recent research efforts have focused on replacing the hot filament with either a microfabricated or a carbon nanotube-based field emitter array that can be operated at room temperature to address the power and outgassing problems of HCGs, the power and outgassing performance of these HCGs are still not comparable with that of CCGs [Gra03, Kna08-2]. Third, auxiliary gas pumping may be feasible in CCGs since the macro-scale ion pump is based on the Penning cell structure, and the magnetron gauge has proved to be operable as an ion pump [Gre13, Hob80]. This auxiliary pumping may provide an avenue for servo-controlled vacuum management.

## 1.3 Focus of This Work

### 1.3.1 Miniaturized RF Electron Traps

One major focus of this work is to demonstrate a centimeter-scale magnet-less RF electron trap that can enable the development of the proposed RFT-CHIP. However, the demonstration of the RF electron trap is challenging. Primarily, the RF frequency that efficiently traps electrons scales inversely with trap size, as does the dominant device capacitance. These scaling properties result in less efficient RF power transfer as the device is miniaturized, especially in terms of generating voltage sufficient for gas ionization. Other miniaturization challenges include dielectric breakdown of thinner insulation layers, and more pronounced effects of fringing electric fields within a small volume. First, an electron trapping module (ETM) that utilizes standard machining processes and parts is developed to provide an experimental demonstration of the RF electron trapping concept based on the conceptual structure shown in Fig. 1-5. The ETM structure is analytically and numerically modeled. Then, the RF electron trap is refined in structure in developing an enhanced-efficiency electron trapping module ($E^3TM$) with higher RF electron trapping efficiency and further device miniaturization. An integrated sorption electrode is stacked in the $E^3TM$ as shown in the schematic (Fig. 1-6), which is another step toward the full RFT-CHIP configuration. In summary, the goals of the miniaturized RF electron traps are as follows:

- Demonstrate RF electron trapping in the ETM
- Improve RF electron trapping efficiency with finer perforated RF electrodes, and simplified electrode composition and RF characteristics in the $E^3TM$

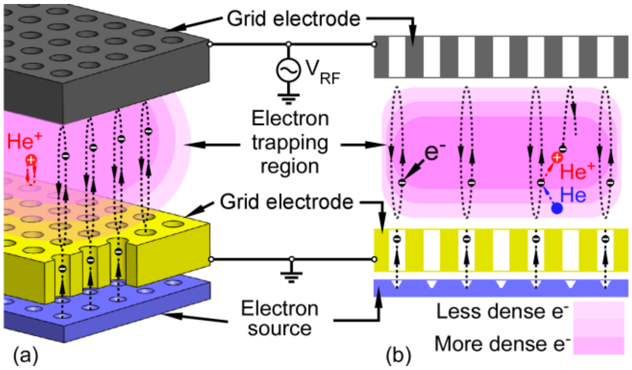

Figure 1-5: Schematic of the ETM concept: (a) 3D model, (b) 2D schematic. The RF electron trap mainly consists of two grid electrodes, which are separated by a certain distance to form an electron trapping region. Electrons are supplied by an external electron source. RF voltage is applied between the two grid electrodes to trap and energize the incoming electrons in the trapping region.

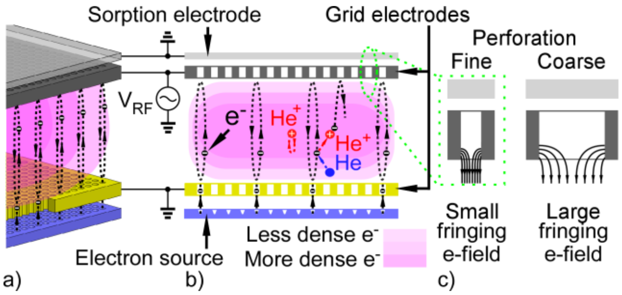

Figure 1-6: Schematic of the $E^3$TM concept: (a) 3D model, (b) 2D schematic, (c) perforation comparison. The $E^3$TM mainly consists of two finely perforated grid electrodes, which are separated by a certain distance to form an electron trapping region. Electrons are supplied by an external electron source. RF voltage is applied between the two grid electrodes to trap and energize the incoming electrons in the trapping region. Sorption electrode is also integrated into the $E^3$TM.

### 1.3.2 Miniaturized Cold Cathode Gauges (CCGs)

Another focus of this thesis is to miniaturize CCGs for use in monitoring the vacuum in the reference chamber of the CDG. In this work, the miniaturized CCGs conform to an overall size constraint of approximately 1 $cm^3$ outside the reference vacuum chamber of the CDG, which is about 10x smaller than most of the commercially available miniature CCGs and recently researched miniaturized CCGs that have an internal volume of at least 10 $cm^3$ (Fig. 1-7). For example, the MKS Series 903 inverted magnetron transducer has an internal volume of 15 $cm^3$ [MKS17]. The volume places additional constraints on the footprint of the gauge, the height of the gauge, the dimensions of any magnetic components with respect to other connections to the CDG, and electrical isolation of high voltage feedthroughs for the gauge. Further, the CCGs aim to have a DC operating voltage lower than 1000 V. However, the miniaturization of gauges is challenging. First, the crossed electric and magnetic fields may not be able to confine electrons in a small enough volume to ensure gas ionization at practical efficiency, as an electron needs to travel several kilometers before a collision with a gas molecule is likely at a pressure of

$10^{-6}$ Torr [Hal81]. This means that the electrons are required to be cycled $10^5$ times in a 1 cm gauge geometry to have a high probability to collide with a gas molecule. Second, all the constraints are maintained to ensure compatibility with the form factor and manufacturing approach used for the CDG. Thus, this work mainly focuses on analyzing the electron trajectory under the resulting electric and magnetic fields for the proposed CCG architectures and on improving the manufacturability of these designs. In summary, the goals of the miniaturized CCGs are as follows:

- Develop an approach to model the electric and magnetic fields distributions and electron spiraling trajectories in different CCG designs
- Refine the CCG designs for better electron spiraling capability and manufacturability to integrate on the CDG
- Fabricate a CCG design with 3D printing technologies and validate its performance

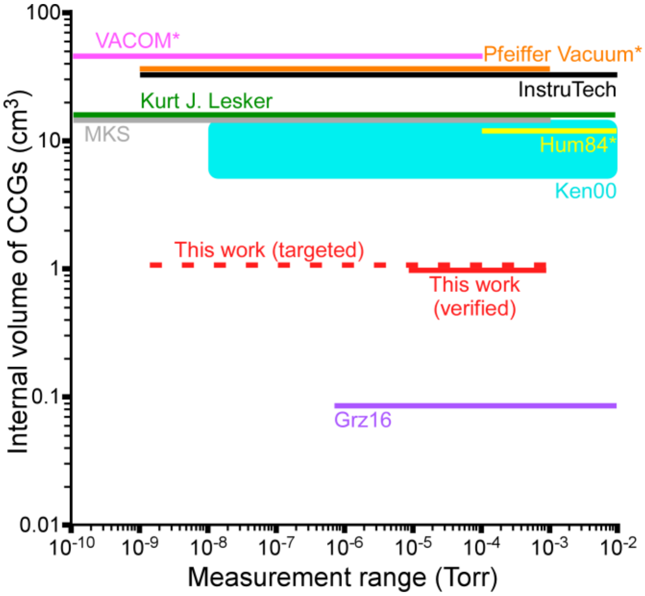

Figure 1-7: A comparison of some commercially available CCGs and miniature CCGs from recent research efforts. VACOM®: COLDION® is a Penning cell type. Pfeiffer Vacuum: cold cathode gauge head IKR 050. InstruTech®: CCM501 Hornet™ is an inverted magnetron type. Kurt J. Lesker®: KJLC 423 series is an inverted magnetron type. MKS: series 903 is an inverted magnetron type. Hum84: a miniature Penning ionization gauge. Ken00: several miniaturized magnetron and inverted magnetron gauges. Grz16: microfabricated MEMS type Penning gauge. The asterisk denotes that the internal volume is estimated [Grz16, Hum84, Ins17, Ken00, Kur17, MKS17, Pfe17, VAC17].

## 1.4 Organization of the Dissertation

Chapter 2 of this work describes the design, fabrication and testing of the ETM, denoted as the first-generation RF electron trap. This ETM forms a 0.7 cm$^3$ electron trapping volume between two perforated RF electrodes spaced 0.7 cm apart. An electrical testing approach is developed for characterizing the density of RF trapped electrons. The peak electron density in the RF electron trap is estimated to be 1000x higher than the electron density in the electron source via the application of an RF electric field, which demonstrates the RF electron trapping concept.

Chapter 3 presents the second-generation RF electron trap, an $E^3$TM, which represents the continuous development and refinement of the ETM. Compared to the ETM, the $E^3$TM has 10x finer perforated RF electrodes, a higher trap-to-device volume ratio, simplified electrode composition and RF characteristics, and a tunable RF operating frequency. The experimental results estimate that the peak electron density in the RF electron trap of the $E^3$TM is 10x higher than the estimated peak electron density in the ETM.

Chapter 4 develops an analytical approach to investigate the electric and magnetic fields and the electron spiraling capabilities of various miniaturized CCG designs. The geometries and fabrication processes of four different CCG designs are refined based on seven preliminary CCG designs and the manufacturing requirements of the CDG. The Design P.MF.1 has an internal volume of 1.1 $cm^3$. The Design M.MF has an even smaller internal volume of 0.4 $cm^3$. Based on the simulation results, Design P.MF.1 can initiate infinite electron spiraling when the anode is biased at 900 V, and Design M.MF can initiate infinite electron spiraling when the cathode is biased at –500 V. A magnetron gauge (Design M.S) is fabricated with 3D printing technologies and characterized from $10^{-3}$ Torr to $10^{-5}$ Torr.

Chapter 5 presents conclusions regarding the achieved performance of the RF electron traps and the assessment of the miniaturized CCG designs. Future work is proposed for performance improvements and further investigations of both topics.

# CHAPTER 2:

# FIRST GENERATION RF ELECTRON TRAP – ELECTRON TRAPPING MODULE (ETM)

As noted in Chapter 1, an RF electron trap is a magnet-less electron trapping solution designed to fit within a miniaturized ion pump. This chapter describes an electron trapping module (ETM) that experimentally demonstrates RF electron trapping at centimeter scale based on the conceptual structure shown in Fig. 1-5. Section 2.1 provides details on the design and fabrication of the ETM. Section 2.2 discusses an analytical model that models the electron trajectory within an idealized RF electron trap. Section 2.3 presents the testing setup and the characterization results of the ETM. Section 2.4 describes the experimental methods and results for the RF electron trapping with the ETM, followed by a discussion in Section 2.5 and a conclusion in Section 2.6.

## 2.1 Design and Fabrication

The ETM utilizes a total of eight electrode elements in a multi-layer, stacked architecture that can be easily reconfigured, thereby providing flexibility in the position, thickness and composition of various elements (Figs. 2-1 and Fig. 2-2). All layers other than two perforated metal electrodes (Fig. 2-1(e)) – RFA and RFB – possess the same U-shaped topography in the X-Z plane with a 1 x 1 $\text{cm}^2$ opening. This opening permits the incoming electrons into the trap formed between the RFA and RFB electrodes, and defines the cross-sectional area of the overall trapping region. The RFA and RFB electrodes are separated by a U-shaped metal element (chassis) whose thickness determines the gap in which the electrons are to be trapped (Fig. 2-1 (f)). The stack is held together by screws and ceramic washers are used for electrical insulation. A U-shape is chosen for the device in this configuration to allow for direct probing of the electron trap through the opening in the U-shape. The effect of the asymmetry in this structure has not been fully measured, but modeling indicates that asymmetries on the edges of the structure do not strongly affect the performance in the central trapping region. Electrical isolation between each metal layer is realized by sandwiching U-shaped ceramic sheets (Fig. 2-1 (d)) between the layers. This configuration enables rapid prototyping to explore the parameter space. For example, the gap between electrodes RFA and RFB can be simply changed by using a thicker chassis. As another example, many perforated metal electrodes that have the same perforation pattern can be stacked to alter the effective aspect ratio of the perforations.

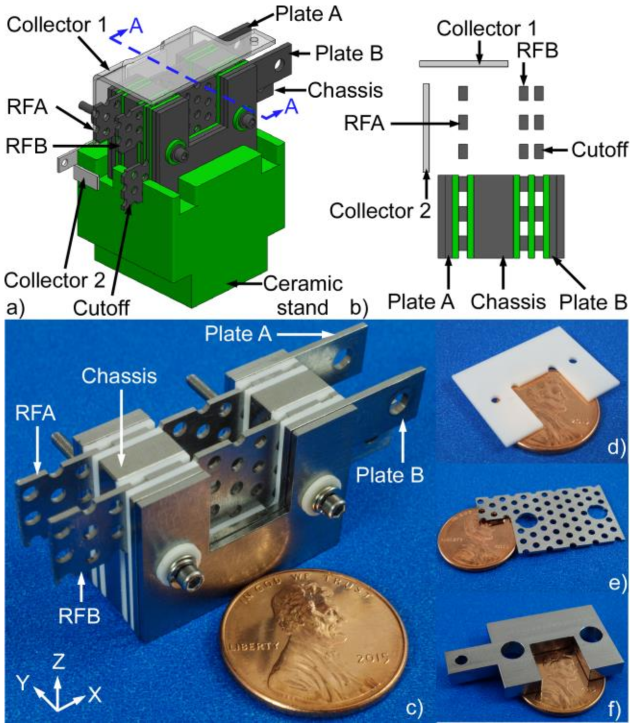

Figure 2-1: a) 3D model of the ETM. b). A-A section view. c) The assembled ETM. d) U-shaped ceramic sheet. e) Perforated stainless steel electrode. f) U-shaped stainless steel chassis.

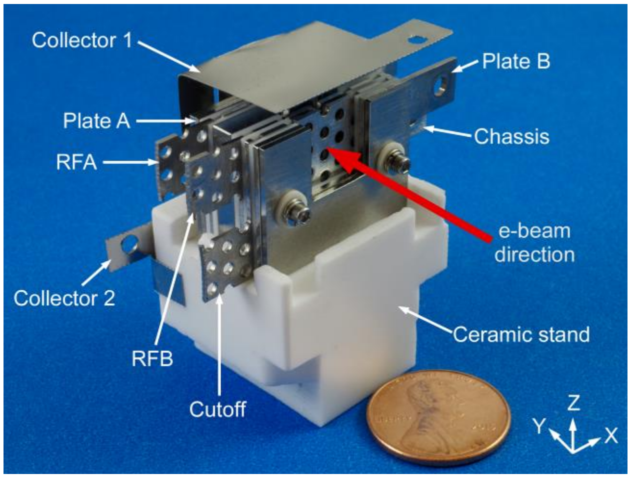

Figure 2-2: The ETM assembled with five additional electrodes. The ETM is electrically isolated and fixed in position within the chamber by a ceramic stand. Collector 1 and Collector 2 are used in diagnostic measurements.

The metal layers are comprised of annealed type 304 stainless steel [Sta16]. The ceramic layers are comprised of machinable Macor® – mica glass ceramic [Mac16]. These materials exhibit low outgassing and are bakeable, and hence are UHV compatible [Els75, Sgo06]. Additionally, these materials are not strongly magnetic [Sta16]. All layers are machined with conventional processes (i.e., milling, drilling, etc.), then cleaned with an acetone/isopropanol/deionized water rinse prior to assembly. The RFA and RFB electrodes are machined from a 0.76 mm thick type 304 stainless steel sheet with a staggered pattern of 1.59 mm diameter holes; these electrodes have 40% open area to allow electrons to pass into the trapping area. These two electrodes are 19 mm wide and 40 mm long, including an extension used for electrical connection. Once the RFA and RFB electrodes are stacked, the perforations are well aligned with a tolerance of $\approx$0.25 mm. The U-shaped ceramic layers (25.4 mm x 19 mm) are machined from 0.75 mm thick machinable ceramic Macor® sheets, and two 1.70 mm diameter alignment holes are drilled into them. The chassis is also made from a type 304 stainless steel sheet, and trimmed down to 5.5 mm in thickness.

To experimentally diagnose the proposed RF electron trapping concept, five additional type 304 stainless steel electrodes are used: Collector 1, Collector 2, a Cutoff electrode, and Plates A and B, as shown in Fig. 2-2. Collector 1 in the X-Y plane covers the open side of the U-shaped stack that bounds the trapping region, whereas Collector 2 covers the opening in the X-Z plane. Collector 1 is bolted to the stack. Collector 2 is clamped to the ceramic stand, and is located opposite the electron source. The perforated Cutoff electrode is sandwiched between electrodes RFB and Plate B, and isolated from both with ceramic layers. The perforation patterns of all three perforated electrodes (RFA, RFB, and Cutoff) are well aligned (within $\approx$0.25 mm) to ensure that incoming electrons can pass into the trap. The Cutoff electrode is the perforated electrode closest to the electron source, so it can be used if necessary to prevent the electrons from going into the trap by biasing it to a positive potential.  Plates A and B are included to minimize the exposed surface area of the ceramic layers and thus reduce charge accumulation on the dielectrics.  The ETM, without considering the two collectors and electrode extensions, is 2.5 x 1.7 x 1.9 $\text{cm}^3$ in volume and encloses a 1.0 x 1.0 x 0.7 $\text{cm}^3$ electron trap.  Detailed parameters of parts in the ETM are listed and summarized in Appendix A.

## 2.2 Analytical Model

An analytical model for demonstrating the RF electron trapping concept is schematically shown in Fig. 2-3.  This simplified ETM only consists of two parallel electrodes that are separated with a gap of *d* of 7 mm as the ETM.  In order to trap and oscillate the electrons between the RFA and RFB electrodes, the magnitude of the RF voltage $|V_{RF}|$ is applied at RFA at a frequency $f_{RF}$, while RFB is grounded to limit the electron excursion within *d/2*, half of the gap between the parallel electrodes.

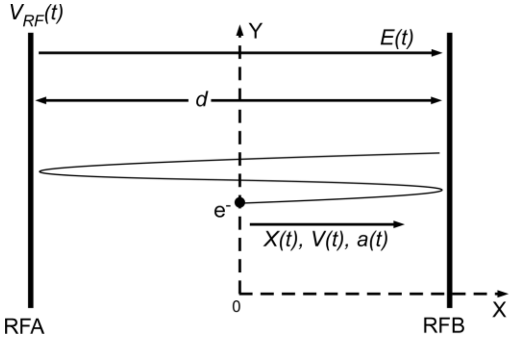

Figure 2-3: Schematic of the analytical model of RF electron trapping.  $|V_{RF}|$ is the RF voltage at frequency $f_{RF}$ applied between two electrodes, separated by gap *d*.  *E(t)* indicates the associated electric field.  The electron will travel in an oscillating horizontal trajectory between the plates (the vertical electron motion depicted here is only for clarity).

Electrons in this electric field experience a Lorentz force:

$$F = -qE(t) = \frac{q}{d}|V_{RF}|\,sin(2\pi f_{RF}t + \phi) \tag{2-1}$$

where $q$ is the fundamental charge, $E(t)$ is the electric field, and $\phi$ is the RF phase. The electron path is not affected by the presence of other electrons, ions or neutrals – which is a fair assumption in the low particle density, low-pressure conditions studied here. In an ideal trap, the electron travels the entire gap between the electrodes periodically and indefinitely. This is considered an “ideally trapped” electron. The position of such an ideally trapped electron at time $t$ is:

$$x^*(t) = \frac{d}{2} - \frac{d}{2}sin(2\pi f_{RF}t + \phi) \tag{2-2}$$

where superscript "*" denotes the ideal condition. Combining the Lorentz force and Newton's Law and comparing to Equation (2-2), one can derive that the ideal RF voltage $|V^*_{RF}|$, the ideal initial position $x^*_0$ and ideal initial velocity $v^*_0$ of the ideally trapped electron are:

$$|V^*_{RF}| = \frac{2m_e(\pi f_{RF})^2}{q}(d)^2 \tag{2-3}$$

$$x^*_0 = \frac{d}{2} - \frac{d}{2}sin(\phi) \tag{2-4}$$

$$v^*_0 = -f_{RF}\pi d\,cos(\phi) \tag{2-5}$$

where $m_e$ is the electron mass. Equations (2-3) – (2-5) show that once an RF frequency and gap have been chosen, the ideal voltage is determined. The choice of frequency (and initial RF phase) will determine which "slice" of the trap ($x_0$ position) will be ideally trapped if the electrons at that slice have the ideal initial velocity $v^*_0$. In other words, only the slice of electrons with the initial position $x^*_0$ and initial velocity $v^*_0$ will be ideally trapped.

A compromise can be made to decrease the path length for electrons in the trap, but allow the electron excursion to be periodical and indefinite (provided appropriate initial conditions are present). This can be achieved by increasing the frequency by an electron trapping confinement factor of $k_{trap} \geq 1$:

$$|V_{RF}| = \frac{2m_e}{q}\left(\frac{\pi f_{RF}}{k_{trap}}\right)^2 (d)^2 \tag{2-6}$$

Using Equation (2-6) along with the Lorentz force and Newton's law, it can be found that the electrons will oscillate around the center of the trap with position described as:

$$x(t) = \frac{d}{2} - \frac{d}{2k_{trap}^2} sin(2\pi f_{RF} k_{trap} t + \phi) \tag{2-7}$$

when the initial conditions are:

$$x_{0,i} = \frac{d}{2} - \frac{d}{2k_{trap}^2} sin(\phi) \tag{2-8}$$

$$v_{0,i} = -f_{RF}\pi d \frac{cos(\phi)}{k_{trap}} \tag{2-9}$$

The benefit of the reduced excursion described by Equation (2-7) is that a "band" of electrons with initial velocity $v_{0,i}$ and initial position $x_0 = x_{0,i} + d/2\Delta x$ also stays within the trap. In this case, the electron position will be:

$$x(t) = \frac{d}{2}(1 + \Delta x) - \frac{d}{2k_{trap}^2} sin(2\pi f_{RF} t + \phi) \tag{2-10}$$

To keep the electrons in the trap, one should ensure that $0 \leq x(t) \leq d$ for all values of $t$. Thus, the electrons with:

$$\frac{1}{k_{trap}^2} - 1 \leq \Delta x \leq 1 - \frac{1}{k_{trap}^2} \tag{2-11}$$

will stay in the trap for all time. As an example, if $k_{trap} = 1.1$, then a band with $-0.18 \leq \Delta x \leq 0.18$ will be trapped (i.e. up to 18% of *d*).

Equation (2-6) can also be expressed as:

$$k_{trap} = \sqrt{\frac{2m_e}{|V_{RF}|q}}\pi f_{RF} d \qquad (2\text{-}12)$$

For $k_{trap} = 1$, the ideal RF trapping voltage $|V^*_{RF}|$ enables the electrons to traverse the entire electrode gap during an RF cycle. For $k_{trap} < 1$, $|V_{RF}|$ larger than $\left|V^*_{RF}\right|$, electrons are accelerated into the electrodes before being turned back, and no RF trapping occurs. For $k_{trap} > 1$, $|V_{RF}|$ smaller than $\left|V^*_{RF}\right|$, trapping still occurs; however, the excursion of trapped electrons will be reduced to only a portion of the inter-electrode gap. The confinement of the electrons between the two RF electrodes is tighter. Alternatively, the $k_{trap}$ value can be used as an indicator of the stability of the electron trajectories in the face of positional or velocity perturbations. A $k_{trap}$ value of greater than 1 allows electrons that are initially "out of phase" with the RF voltage from a positional or energy standpoint to remain within the electrode gap while cycling. Although this can be an advantage, operating under conditions with a very high $k_{trap}$ value will generally result in reduced time-averaged electron energy for a given RF power level. In turn, the RF electron trap will return a lower ionization efficiency as the gas ionization rates decrease when electron energy is reduced. Further, negligible ionization will occur once the electron energy is lower than the ionization energy.

## 2.3 Testing Setup and RF Characterizations

### 2.3.1 Vacuum Setup

The experimental setup is configured to provide the vacuum environment and electron source for testing the RF electron trapping (Fig. 2-4). The pumps are connected to the vacuum chamber (Kimball Physics, 2.75" Double Spherical Cube Vacuum Chamber) through a tee connector and individual manual isolation valves. It uses an all-in-one turbo pump (Agilent, Mini-TASK AG81), capable of pumping down to $<10^{-7}$ Torr, and a sputter ion pump (Agilent, 20L/s VacIon Pump), capable of pumping down to $10^{-10}$ Torr. One valve (Kurt J. Lesker, 2.75" CF Manual Bellows Sealed SS Angle Valves) is attached to the chamber for venting, and one valve (Agilent, Variable Leak Valve) is attached for leaking in small amounts of gas, e.g. helium. The pressure inside the chamber is continuously monitored by an ion gauge (Adixen, AHC 2010). One BNC electrical feedthrough (Kurt J. Lesker, 2.75" CF 4xBNC) and one safety high voltage (SHV) electrical feedthrough (Kurt J. Lesker, 2.75" CF 4xSHV) are connected to the chamber to provide electrical access to all metal layers of the ETM. An electron gun (Kimball Physics, FRA-2X1-2 Electron Gun) with an insertion length of 150 mm serves as the electron source for the RF electron trapping testing. The electron gun is offset by 58.74 mm with a custom 2.75" CF full nipple from the right side of the chamber, such that the tip of the cathode barrel for the electron gun is 10.7 mm away from the opening of the ETM. This separation is close to the minimum working distance for this electron gun, and maximizes the percentage of the emitted electrons arriving at the trapping region. Several customized stands are used to mechanically support the setup and to adjust the relative positions of the different components.

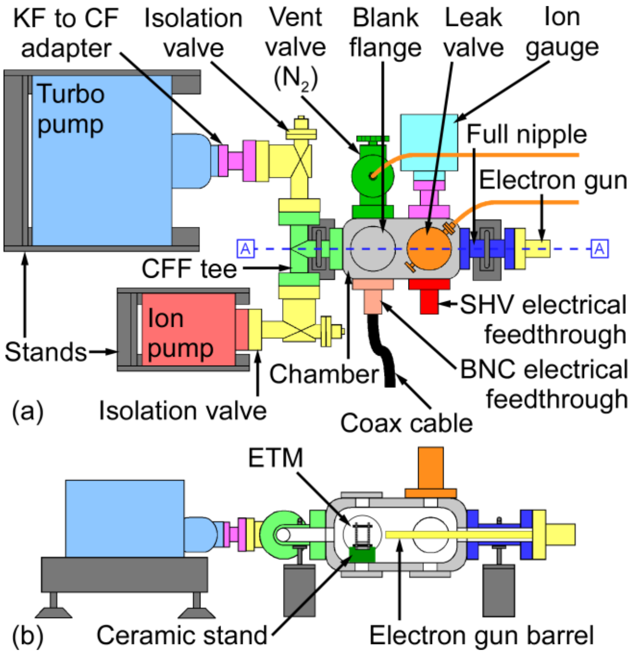

Figure 2-4: The experimental vacuum setup for the ETM. a) Top view. b) A-A sectional view.

The ETM is placed on a customized Macor® stand for electrical isolation from the grounded chamber (Fig. 2-2). The ceramic stand is fixed by two 2.75" Groove Grabbers (Kimball Physics, MCF275-GrvGrb-C02). It is located in the left part of the chamber close to the BNC electrical feedthrough. The trap opening is perpendicular to and centered on the tip of the electron gun barrel. The red arrow in Fig. 2-2 indicates the incoming direction of the electron beam.

The RFA, RFB, Cutoff electrodes, and the chassis are electrically connected via the 50 Ω BNC electrical feedthrough with minimum lengths of solid core wire (Fig. 2-4). The intent here is to reduce parasitic inductances and capacitances at RF frequencies. Collector 1, Collector 2, Plate A, and Plate B electrodes are electrically connected to the SHV electrical feedthrough via solid core wire. This feedthrough can accommodate high DC voltage (> 1 kV) and pulsed DC signals.

### 2.3.2 Electrical Testing

For a typical capacitively coupled plasma (CCP) utilized in a commercial reactive ion etching chamber, a capacitor is usually placed between the RF power source and a powered electrode – which is isolated from the grounded chamber – to store electrons and build up a negative DC bias voltage. This negative DC bias will help in generating positive plasma potential over the edge of the plasma to attract positive ions across the sheath to bombard, react with, and etch the substrate [Sug98]. Inspired by the CCP approach, a similar electrical testing setup is developed for the ETM as shown in Fig. 2-5(b). Capacitors are placed in series with electrodes that are near the trapping region – RFA, Collector 1, and the chassis – to provide DC isolation, while all other electrodes are grounded. These DC-isolated electrodes build up negative potentials – $V_{Col1}$ at Collector 1 and $V_{Cha}$ at the chassis – that are related to the electron density in the trapping region [Sug98]. Eventually, an equilibrium electron density is maintained in the trapping region after applying a specific RF signal between RFA and RFB, which establishes the steady state electrode potentials (SSEPs) for Collector 1 at $V_{Col1\_ss}$ and the chassis at $V_{Cha\_ss}$. A high impedance 10:1 voltage divider is placed in parallel with the DC blocking capacitor to step down the electrode potential; the reduced voltage is measured by a digital multimeter (Agilent, 34401A). The input impedance of this multimeter (10 GΩ) substantially exceeds the impedance across which it is placed (0.1 GΩ). The overall impedance in parallel with the DC blocking capacitor is 1.1 GΩ, which is high enough to avoid shunting a significant electron current from the trap. In order to ensure that the placement of these capacitors does not significantly shift the series resonant frequencies of the device, relatively large capacitors (86 pF) are used.

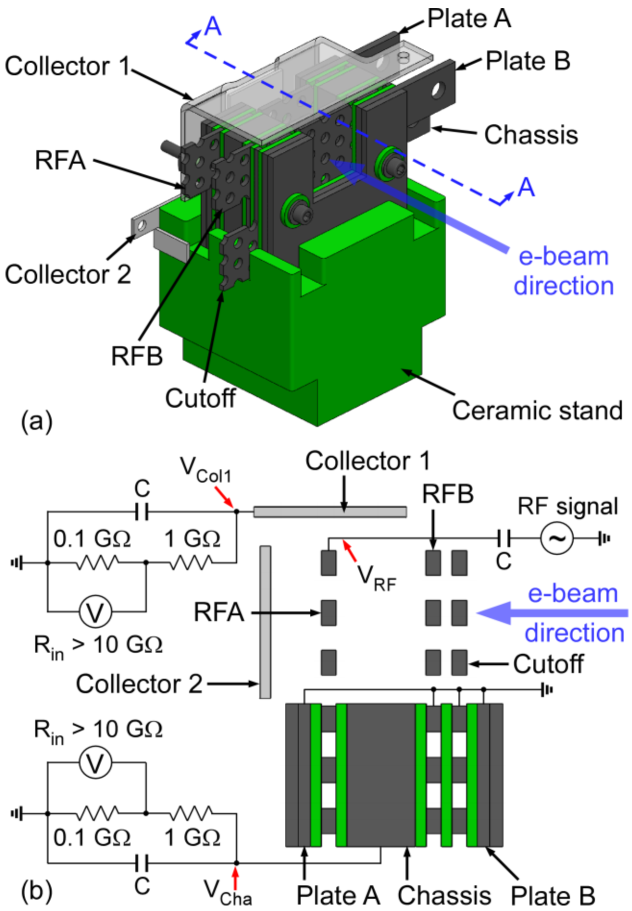

Figure 2-5: Testing setup of the ETM. a) A 3D drawing of the ETM. The electron beam is directed into the ETM with its spot size (20 mm) covering the Cutoff electrode. b) Section A-A and electrical testing setup for RF electron trapping. DC blocking (AC passing) capacitors are connected to the chassis, and Collector 1 electrodes. Another capacitor is connected between the RF source and the RFA electrode.

### 2.3.3 RF Characteristics

The behavior of the ETM at RF frequencies must be understood in order to estimate the RF voltage $|V_{RF}|$ generated across the RF electrodes for a given forward RF power $P_{fwd}$. For this characterization, all electrodes and the chamber are grounded except the RFA electrode, where the RF voltage is applied. A 60 cm long LMR-400 low loss RF coaxial cable is connected between the RFA electrode via the associated BNC electrical feedthrough and the impedance analyzer (Agilent, 4395A). The impedance of the ETM along with the cable $Z_{in}$ is measured, and the ETM impedance $Z_L$ (blue impedance trace, Fig. 2-6(a)) is de-embedded by utilizing a lossless cable assumption and a lossless transmission line equation [Qia09]:

$$Z_{in} = Z_0 \frac{Z_L + jZ_0 \tan\left(\frac{2\pi f_{RF}}{k_v c} L\right)}{Z_0 + jZ_L \tan\left(\frac{2\pi f_{RF}}{k_v c} L\right)} \tag{2-13}$$

where $Z_{in}$ is the measured impedance along the coaxial cable, $Z_0$ is the characteristic impedance of the cable (50 Ω), $c$ is the speed of light, $k_v$ is the velocity of propagation for the LMR-400 cable (0.85), and $L$ is the length of the cable (0.6 m) [LMR17].

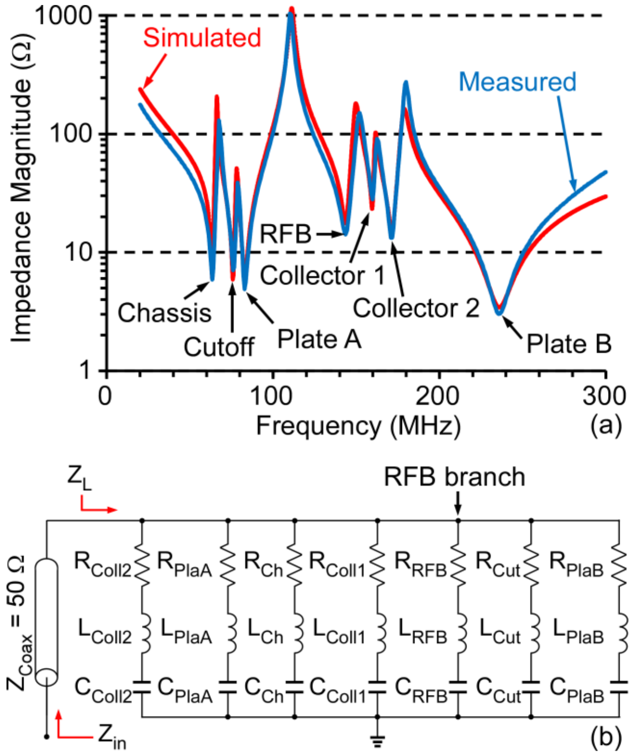

Figure 2-6: a) The de-embedded ETM impedance magnitude $|Z_L|$ (blue curve) from the RFA electrode from 20 MHz to 300 MHz with all electrodes except the RFA electrode grounded compared with the SPICE simulated $|Z_L|$ (red curve) from the equivalent circuit model of the ETM. The de-embedded device impedance results suggest that the eight electrode elements in the device form parallel branches from the RFA electrode to the ground, each with a series resonant behavior. b) The equivalent circuit model of the ETM.

A simplified equivalent circuit model (Fig. 2-6(b)) with seven series RLC branches in parallel from the RFA electrode to the ground is developed to represent the eight electrode elements in the ETM. For example, examining the RFB branch of the equivalent circuit model shows the capacitor $C_{RFB}$ formed between the RFA and RFB electrodes. However, a stray resistance $R_{RFB}$ and a stray inductance $L_{RFB}$ are also present due to the unshielded wires in the vacuum chamber, the contact resistances of these wires, and the skin effect within the electrodes [Hay11]. These parasitic components, along with the capacitance, cause a series resonant dip in the measured device impedance.

In order to assign the series resonant frequencies from the de-embedded impedance – the blue curve of Fig. 2-6(a) – to the correct branches of the equivalent circuit model, an experimental method is utilized. In this method, one branch at a time is loaded with an inductor (225 nH) between the electrode and the ground. A resulting shift of one of the series resonant dips in the measured (de-embedded) impedance is observed, indicating that the loaded branch is associated with that series resonant frequency. The process is repeated for each branch. In this way, the series resonant frequencies of all seven branches can be identified.

The capacitances in each branch are first measured with an LCR meter (Hewlett-Packard, 4284A); these values are the initial estimations for the capacitor in each branch. The inductance in each series RLC branch is determined by keeping the product of the inductance and capacitance at a fixed value, which links to the series resonant frequency associated with that branch. The impedance at each series resonant frequency is then used to estimate the stray resistance of the associated branch, since the reactance of the capacitor and the inductor in that branch are canceled out at series resonance. Then, the estimated values of the inductances and capacitances are tuned together to match not only the series resonant dips, but also the parallel resonant peaks in the de-embedded ETM impedance results. The values of all components in the equivalent circuit model are summarized in Table 2-1. The SPICE simulated impedance of the ETM using this model (red impedance trace, Fig. 2-6(a)) is well aligned with the measured de-embedded ETM impedance (blue impedance trace, Fig. 2-6(a)). This agreement indicates that the equivalent circuit model is an appropriate representation of the ETM.

Table 2-1: Resonant frequencies and element values used in the equivalent circuit model.

| Branch | Resonant frequency $f_0$ (MHz) | Resistance $R$ (Ω) | Inductance $L$ (nH) | Capacitance $C$ (pF) |
|---|---|---|---|---|
| Chassis | 63.3 | 6.25 | 1210.00 | 5.23 |
| Cutoff | 75.9 | 6.25 | 916.90 | 4.80 |
| Plate A | 82.8 | 6.25 | 400.10 | 9.23 |
| RFB | 143.6 | 18.75 | 921.25 | 1.33 |
| Collector 1 | 159.7 | 28.12 | 3103.75 | 0.32 |
| Collector 2 | 171.5 | 15.63 | 747.50 | 1.15 |
| Plate B | 235.8 | 3.44 | 47.44 | 9.60 |

With the developed circuit model, the actual $|V_{RF}|$ applied between electrodes RFA and RFB for a given $P_{fwd}$ can be estimated by the $|V_{RF}|$ appearing on $C_{RFB}$ in the equivalent circuit model using the following equations [Gra91]:

$$\Gamma = \frac{Z_L - Z_0}{Z_L + Z_0} \tag{2-14}$$

$$P_t = P_{fwd} \cdot (1 - |\Gamma|^2) \tag{2-15}$$

$$V_{L,peak} = \sqrt{2P_t \cdot Z_L} \tag{2-16}$$

$$I_{RFB,peak} = \frac{V_{L,peak}}{R_{RFB}+j\left(2\pi f_{RF}L_{RFB}-\frac{1}{2\pi f_{RF}C_{RFB}}\right)} \tag{2-17}$$

$$|V_{RF}| = \frac{|I_{RFB,peak}|}{2\pi f_{RF}C_{RFB}} \tag{2-18}$$

where $\Gamma$ is the voltage reflection coefficient, $P_t$ is the transmitted RF power to the ETM, $V_{L,peak}$ is the peak voltage across the ETM, and $I_{RFB,peak}$ is the peak current through the RFB branch. Using this model, the $|V_{RF}|$ at the RFA electrode is calculated over the frequency range at different values of $P_{fwd}$, as represented by the three colored curves in Fig. 2-7. The calculated $|V_{RF}|$ peaks for any given value of $P_{fwd}$ at the series resonant frequency of the RFB branch (143.6 MHz).

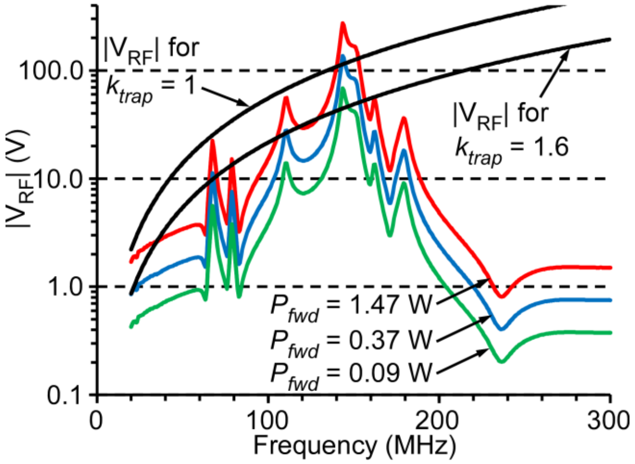

Figure 2-7: Three colored curves indicate peak RF voltage $|V_{RF}|$ developed at the RFA electrode across the frequency range under different $P_{fwd}$. $|V_{RF}|$ values versus frequency are plotted for $k_{trap}$ of 1 and 1.6 (Equation (2-12)).

As electrons enter the trap, they are subjected to the oscillating Lorentz force driven by the RF electric field. This force causes the electrons to oscillate between the RF electrodes. When the values of $|V_{RF}|$, $f_{RF}$, and $d$ in Equation (2-12) result in a $k_{trap}$ of 1, the oscillating trapped electrons travel the entire gap between electrodes RFA and RFB during each cycle, which is considered an ideal trap. The voltage amplitude for $k_{trap}$ = 1 is denoted as $\left|V_{RF}^{*}\right|$. The calculated $\left|V_{RF}^{*}\right|$ for this 0.7 cm gap device over the frequency range of 20-300 MHz is indicated by the $k_{trap}$ = 1 curve in Fig. 2-7. No RF electron trapping is expected to exist when the RFA electrode is operated with $|V_{RF}| > \left|V_{RF}^{*}\right|$, as electrons will be accelerated beyond the trap before the voltage can cycle to keep them in the trap. In this case, $k_{trap}$ is less than 1. With $|V_{RF}|$ lower than $\left|V_{RF}^{*}\right|$, or $k_{trap} > 1$ equivalently, RF trapping is expected to exist with tighter confinement, as the excursion of trapped electrons will be reduced to only a portion of the electrode gap (example voltages for this case are the $|V_{RF}|$ indicated by the $k_{trap}$ = 1.6 curve in Fig. 2-7). By substituting the calculated $\left|\mathrm{V}_{\mathrm{RF}}^{*}\right|$ at $f_{RF}$ of 143.6 MHz into Equation (2-18) from the equivalent circuit model, the required $P_{fwd}$ to initiate this ideal RF electron trapping can be determined. The calculated ideal operating RF signal for the 0.7 cm gap ETM is at $f_{RF}$ of 143.6 MHz, and $P_{fwd}$ of 0.836 W. Note that only a portion of the $P_{fwd}$ is transmitted to the device, while the remainder is reflected back to the source; this power transmission efficiency can be improved with an appropriate matching network or RF transformer.

## 2.4 Experimental Methods and Results

### 2.4.1 Experimental Methods

All RF electron trapping tests were performed using a 40 μA steady emission current and 15 eV electron energy. The emission current was provided by an electron gun (Kimball Physics, FRA-2X1-2) and a controller. The vacuum chamber was maintained at 7 x $10^{-8}$ Torr for all tests.

The testing protocol was the same for all the RF electron trapping tests. A customized LabVIEW® data acquisition program was used to simultaneously record all voltage readouts from the digital multimeters during the course of the RF electron trapping tests. First, 30 seconds before turning on the RF at a specific power level, the reference steady state electrode potentials (reference SSEPs) across the DC blocking capacitors with only the presence of electron beam were recorded as $V_{Col1\_rss}$ at the Collector 1 and $V_{Cha\_rss}$ at the Chassis. Once the RF was powered on, observable changes in both $V_{Col1}$ and $V_{Cha}$ occurred over a course of minutes. Eventually the two electrode potentials arrived at a new stabilized steady state before the end of data acquisition, which was $V_{Col1\_ss}$ at Collector 1 and $V_{Cha\_ss}$ at the chassis. At this point, the measurement was concluded, the RF power was switched off, and the DC blocking capacitors were shorted with a 10 MΩ resistor to discharge any charge built up during RF electron trapping. Typically, a two-hour wait after this process was required for the electrode potentials to return to reference steady state values with just the electron source. Then, a new RF power level was selected, and the experiment was repeated. After all the RF electron trapping tests, the SSEPs were measured at all the tested RF signal levels without the presence of the electron beam through the above testing protocol for reference purposes, and the measured SSEPs were returned with 0 V.

### 2.4.2 Results

The recorded reference SSEPs were –13.5 V at both Collector 1 ($V_{Col1\_rss}$) and the chassis ($V_{Cha\_rss}$), as shown in Fig. 2-8. No major shifts of $V_{Col1\_rss}$ and $V_{Cha\_rss}$ were found throughout the course of testing. The recorded $V_{Col1\_ss}$ and $V_{Cha\_ss}$ as a function of RF power at $f_{RF}$ of 143.6 MHz are shown in Fig. 2-8. The testing sequence of RF electron trapping experiments is indicated by the subscripts in the results, and the repeatability of testing results is indicated by the error bars at different power levels. At $P_t$ of 0.033 W ($P_{fwd}$ of

0.105 W), $V_{Col1\_ss}$ was –15.9 V, while $V_{Cha\_ss}$ was –20.8 V; both values were more negative than the recorded $V_{Col1\_rss}$ and $V_{Cha\_rss}$. As $P_t$ increased to 0.130 W ($P_{fwd}$ of 0.419 W), $V_{Col1\_ss}$ increased to –13.0 V, and $V_{Cha\_ss}$ was –13.1 V; both values were close to the recorded $V_{Col1\_rss}$ and $V_{Cha\_rss}$. Further, $V_{Col1\_ss}$ was –13.2 V, and $V_{Cha\_ss}$ was –5.5 V at $P_t$ of 0.517 W ($P_{fwd}$ of 1.668 W); both $V_{Col1\_ss}$ and $V_{Cha\_ss}$ became more positive than the $V_{Col1\_rss}$ and $V_{Cha\_rss}$.

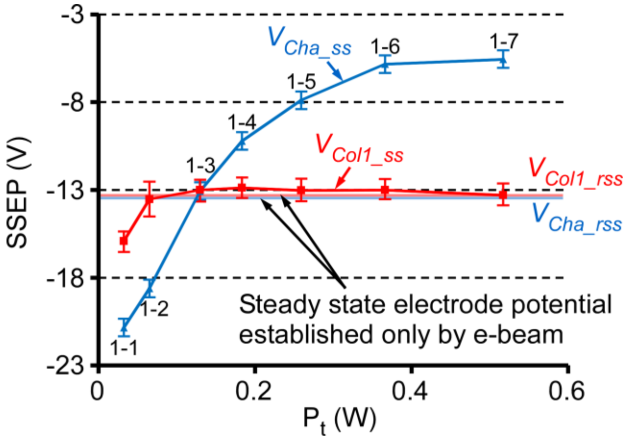

Figure 2-8: The $V_{Col1\_ss}$ and $V_{Cha\_ss}$ measured during RF electron trapping at different level of power transmitted to the ETM, $P_t$ with a fixed $f_{RF}$ of 143.6 MHz. The horizontal lines represent the recorded $V_{Col1\_rss}$ and $V_{Cha\_rss}$ with only the injection of the 40 µA electron beam.

The dependence of $V_{Col1\_ss}$ and $V_{Cha\_ss}$ on RF frequency is shown in Fig. 2-9. Based on five testing points in the frequency range from 141 MHz to 152.5 MHz at a fixed $P_{fwd}$ of 0.836 W (at 143.6 MHz, this is calculated as $P_t$ of 0.259 W), $V_{Cha\_ss}$ ranged from –7.4 V to –6.2 V, and $V_{Col1\_ss}$ ranged from –13.1 V to –12.0 V. The change in $V_{Col1\_ss}$ and $V_{Cha\_ss}$ over the investigated frequency range was approximately 10%.

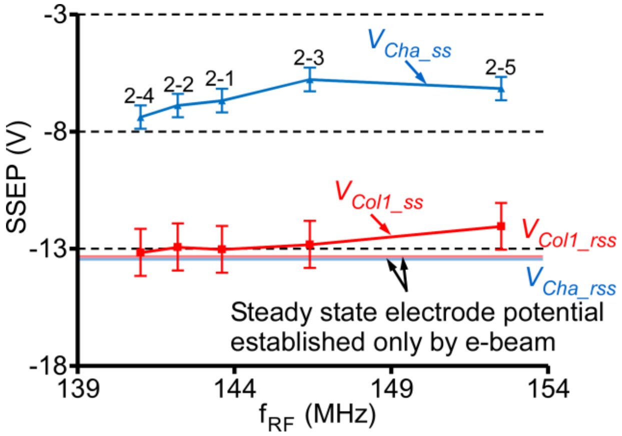

Figure 2-9: The $V_{Col1\_ss}$ and $V_{Cha\_ss}$ measured during RF trapping at different $f_{RF}$ with a fixed $P_{fwd}$ of 0.836 W ($P_t$ of 0.259 W at 143.6 MHz). The horizontal lines represent the recorded $V_{Col1\_rss}$ and $V_{Cha\_rss}$ with only the injection of the electron beam.

## 2.5 Discussion

The $V_{Col1\_ss}$ and $V_{Cha\_ss}$ are more negative than $V_{Col1\_rss}$ and $V_{Cha\_rss}$ at $P_t$ of 0.033 W ($P_{fwd}$ =0.105 W), which implies that the electron density in the trapping region increases with the application of the RF voltage, as is consistent with the design expectations. The more negative potentials measured at these electrodes when RF voltage is applied denote a larger thermal electron current through the resistor networks connected to the electrodes. This larger thermal electron current is available only from the higher electron density near the electrodes. Furthermore, $V_{Cha\_ss}$ is more negative than $V_{Col1\_ss}$. This result further supports the conclusion that a more negative electrode potential corresponds to a higher electron density, for the following reasons. The U-shaped metal chassis, sandwiched by the RFA and RFB electrodes, has three sides immediately adjacent to the RF electron trapping region, while Collector 1 only covers the remaining side of the trap and is $\approx$3 millimeters farther away from the trap. Thus, the chassis is physically closer to the trapping region, and has more area surrounding the electron trap, than Collector 1. The physical proximity to the region of higher electron density and the larger surface area of the chassis accesses more electron current, leading to a more negative potential on the chassis.

The use of the steady-state DC potentials on these electrodes, rather than any RF or other rapidly changing voltages, is an important aspect of the measurement technique. The vast difference in time scales between when these potentials are measured (minutes after application of RF power) and the period of the RF cycle (nanoseconds for each cycle) helps to separate the changes in potential due to local, RF-driven electron movement from those changes due to thermal drift and diffusion of the electrons. The slower thermal drift and diffusion processes are more indicative of average electron density and are more properly measured with the steady-state DC potential established on the electrodes.

While the diagnostic approach utilized here is simple and adequate for semi-quantitative assessment of the trapping concept, improvement of the approach or utilization of other diagnostic methods warrants investigation in future assessment and refinement of the RF traps. The approach utilized here can be improved in the future with an appropriate redesign: rather than relying on the chassis or Collector surfaces that are necessarily at the periphery of the trapping volume, a needle-like probe can be positioned near the center of the trapping volume. Utilizing a very small probe in this location will minimally disturb the electric fields and RF behavior of the device, while also providing the most sensitivity to the location of the largest electron density within the trapping volume. An important constraint on the size of the probe is that it should minimize perturbations of the plasma and electric fields. The recommended probe size depends on the mean free path of the gas and can be larger at the low pressures used in this device

[God02]. In principle, microfabricated Langmuir probes can be incorporated with an appropriate redesign [Chi11, Chi14]. Although optical techniques such as interferometry and Stark broadening have been used to estimate plasma densities, these techniques would be extremely challenging in the compact, very low density plasmas created by this device.

A plasma transport model [Kus09] was extended and used to analyze the ETM SSEP testing; this process is described in [Mar17]. The model was used to estimate the electron distribution as well as the potentials at capacitively-isolated electrodes while operating at different RF voltage levels. For $|V_{RF}|$ of 150 V at RFA electrode and an $f_{RF}$ of 150 MHz as shown in Fig. 2-10, modeling results show 3-4 orders of magnitude increase in electron density in the trapping region [Mar17]. In addition, the simulated SSEPs at this RF voltage level are more negative than the simulated reference SSEPs with only the presence of the electron beam. These results support the premise that higher electron density results in a more negative SSEP.

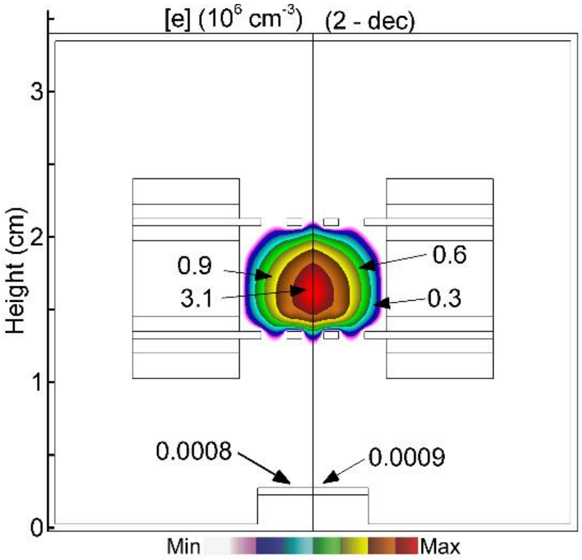

Figure 2-10: Simulated electron density based on a plasma transport model (He, 80 nTorr, 150 MHz, 150 V, 15 eV initial electron energy, 40 µA electron current from source). Densities are plotted on a two-decade log scale with the maximum values indicated [Mar17].

It should be noted that these negative SSEPs peak at an RF power level – $P_t$ of 0.033 W ($P_{fwd}$ = 0.105 W) – that is lower than the estimated ideal RF power level – $P_t$ of 0.259 W ($P_{fwd}$ = 0.836 W). The most likely cause of this is the non-ideality of the electric fields resulting from the perforated electrodes. The relatively large perforations result in lateral fringing fields near the electrodes extending into a significant portion of the trap volume. The ideal power level is estimated from a simple model that does not account for these lateral fields, and is termed "ideal" because it would allow the entirety of the trap volume to be utilized. However, the existence of the lateral fringing fields effectively reduces the usable trap volume, and thus a lower voltage (resulting in a higher $k_{trap}$ and a reduced electron excursion) at a lower power level more optimally densifies the electrons in this case.

As $P_t$ increases in Fig. 2-8, $V_{Col1\_ss}$ and $V_{Cha\_ss}$ become more positive, indicating a less efficient trap. With further increase in the $P_t$, $V_{Col1\_ss}$ and $V_{Cha\_ss}$ become more positive than $V_{Col1\_rss}$ and $V_{Cha\_rss}$. This indicates a smaller electron density in the trapping region due to the applied RF signals. Both of these observations are expected from Equation (2-12). As $|V_{RF}|$ becomes larger than $\left|V_{RF}^{*}\right|$, the incoming electrons are accelerated excessively and leave the trap before the voltage can cycle and keep the electrons in the trap. Therefore, the trends in Fig. 2-8 indicate that the most effective electron trapping occurs over a small range of RF power. RF power outside this range results in reduced electron trapping. The peak electron density inside the trap predicted by the model over a range of $|V_{RF}|$ applied for $f_{RF}$ of 150 MHz indicates a similar small range of trapping potentials (Fig. 2-11) [Mar17].

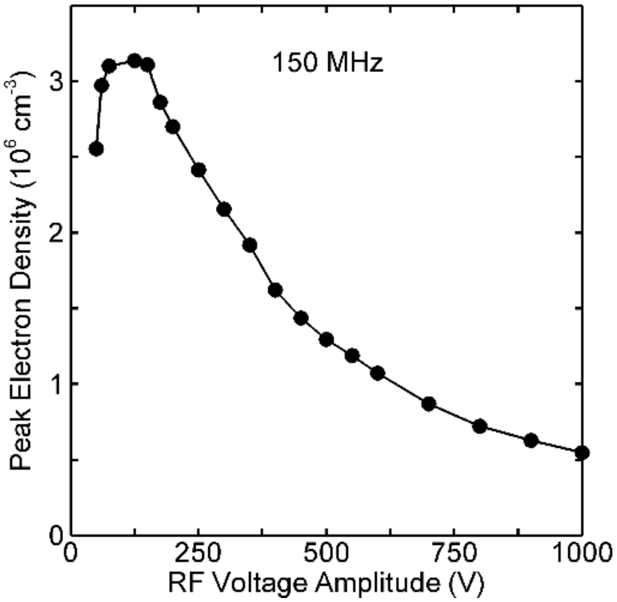

Figure 2-11: Simulated maximum electron densities as a function of applied RF voltage at 150 MHz (He, 80 nTorr, 15 eV, 40 µA) [Mar17].

The charge density in the trap is small and may be below the ambipolar limit, so charge neutrality is not strictly required. Even so, assuming that the trapped electron density is equal to the ion density to maintain the zero net charge in the trapping region, and that all ions are helium ions, the electron current equation for a planar probe with a collisionless sheath (Equation 2-19) can be used to estimate the electron density near the capacitively isolated electrodes (the chassis and Collector 1) [Lie94].

$$I_e = -\frac{V_p}{R} = \frac{1}{4} q n_e \overline{v_e} A_p exp\left(\frac{V_p}{T_e}\right) \tag{2-19}$$

where $V_p$ (in volts) is either $V_{Col1\_ss}$ or $V_{Cha\_ss}$, $n_e$ is the estimated electron density, $q$ is the fundamental charge, $T_e$ is the electron temperature, $\overline{v_e}$ is the average thermal speed of electrons at $T_e$, $A_p$ is the electrode surface area, and the electron current $I_e$ in the original equation is calculated from the recorded steady state electrode potential $V_p$ divided by the resistor $R$ (1.1 GΩ) in parallel with the DC blocking capacitors. After simplification:

$$n_e \approx -1.4 \times 10^4 \cdot V_p \, cm^{-3} \tag{2-20}$$

The estimated electron density is $3 \times 10^5$ cm$^{-3}$ near the chassis at $P_t$ of 0.033 W and $f_{RF}$ of 143.6 MHz, which agrees well with the simulated electron density near the edge of the trap as shown in Fig. 2-11 [Mar17]. Note that this simplified relation is only expected to be valid for a very limited range of operating conditions. The simulation results presented here and in [Mar17] are expected to be valid over a larger range of operating conditions, as the numerical modeling makes no assumptions about charge neutrality, accounts for non-ideal electric fields, and incorporates the effects of charge accumulation on dielectric surfaces.

At $P_t$ of 0.259 W at 143.6 MHz, the difference between the SSEPs with RF and without RF were large, so the SSEPs are expected to result in the most sensitivity to frequency at this power level. However, the values of $V_{Col1\_ss}$ and $V_{Cha\_ss}$ stay flat over the tested frequency range in Fig. 2-9, indicating that the electron density within the trap is similar over a range of $f_{RF}$ at approximately the same power level. Similarly, the simulated peak electron densities are relatively insensitive to frequency and can occur over a fairly broad $k_{trap}$ region, as indicated in the numerical modeling in [Mar17].

As suggested by the results from the ETM, improvements can be implemented in future designs to achieve better electron trapping performance. First, finely perforated RF electrodes are preferable because the finer perforations result in lateral fringing fields that occupy much less of the trap volume. Then, parasitic resistances and capacitances of the device can be minimized by reducing unused electrodes, reducing the volume and exposed surface area of the ceramics, and improving skin effect losses. Reduction of parasitic resistances and capacitances will effectively improve the quality factor of the series resonance of the device, which should significantly reduce the power consumption.

## 2.6 Conclusion

The ETM work demonstrated that magnet-less RF-based electron traps are viable at sub-cubic centimeter scales. The trap utilizes RF electric fields to oscillate electrons in the trapping volume (0.7 $cm^3$) between two perforated electrodes. A measurement technique was identified to estimate the efficiency of RF electron trapping. This technique is based on measuring steady state potentials on electrodes near the trap, and correlating those values with the thermal electron current and electron density within the trap. At $P_t$ of 0.033 W for $f_{RF}$ = 143.6 MHz, the measured SSEPs at the chassis and Collector 1 were more negative than reference SSEPs with RF power off and due to only the injection of the electron beam. These results are consistent with the premise that the electron density over the trapping region was increased by the applied RF signal, up to a calculated value of $\approx 3 \times 10^5$ $cm^{-3}$ near the walls of the trapping region. In accordance with analytical and numerical modeling, larger RF power levels indicated a lower electron density (calculated to be as low as $\approx 1 \times 10^5$ $cm^{-3}$ near the walls of the trapping region), and demonstrated that effective RF electron trapping only occurs over a certain RF power range at a specific RF frequency. The miniaturized RF electron trap described here addresses the challenges of magnet-less electron confinement and RF power transfer in a miniaturized device, and may enable magnet-less ion pumping solutions that will significantly increase the operating lifetime of extremely accurate atomic microsystems currently in development.

# CHAPTER 3:

## SECOND GENERATION RF ELECTRON TRAP –

## ENHANCED-EFFICIENCY ELECTRON TRAPPING MODULE ($E^3$TM)

Chapter 2 described the successful demonstration of the RF electron trapping concept with the ETM. However, the electron trapping efficiency can be improved through design modifications. Therefore, the second-generation electron trapping model, the enhanced-efficiency electron trapping module ($E^3$TM), is refined in structure, material selection, and fabrication processes as described in this chapter. To improve the electric field uniformity in the $E^3$TM, two RF electrodes are perforated 10x more finely than those in the ETM, and the exposed ceramic surface area is reduced. Other structural improvements lead to a higher trap-to-volume ratio, and a simplified RF characteristic in the $E^3$TM. Titanium and tantalum are used as electrodes materials in the $E^3$TM in consideration of pumping requirements. Lithography-based, batch-compatible fabrication processes are used to fabricate some components of the $E^3$TM.

The $E^3$TM design and fabrication are described in Section 3.1. Section 3.2 introduces the experimental setup. Based on the assembled $E^3$TM in the revised vacuum system, Section 3.3 presents the electrical characteristics of the $E^3$TM. Section 3.4 describes the revised experimental methods and the measured results, followed by a discussion and conclusion in Section 3.5 and Section 3.6.

## 3.1 Design and Fabrication

### 3.1.1 Design and Structure

The $E^3$TM is directly built on top of a 1.33" CF 9-pin electrical feedthrough (Accu-Glass Products, Inc., 9C-133) [Acc17]. No additional wiring is required during vacuum installation, as shown in Fig. 3-1. It mainly consists of three electrodes – top and bottom RF electrodes, and a sorption electrode – and two adapters in a stacked architecture. The three electrodes are in the same circular shape with an outer diameter of 15 mm, which defines the overall shape of the $E^3$TM. The top and bottom RF electrodes are separated by 7 mm in the Z direction with the use of three tapped standoffs. This determines the gap in which the electrons are to be trapped within the $E^3$TM. Two adapters are used to achieve reliable electrical connections and robust mechanical support. The $E^3$TM has the same basic operation to trap electrons by a RF signal as the ETM described in Chapter 2. A RF signal is applied to the bottom RF electrode, and all other metal parts are grounded. This forms a RF electric field between the two RF electrodes. Electrons are supplied by an electron gun from the top of the top RF electrode. The electrons that pass through the perforations on the top RF electrode are then trapped by the RF electric field to oscillate between the two RF electrodes due to the oscillating Lorentz forces.

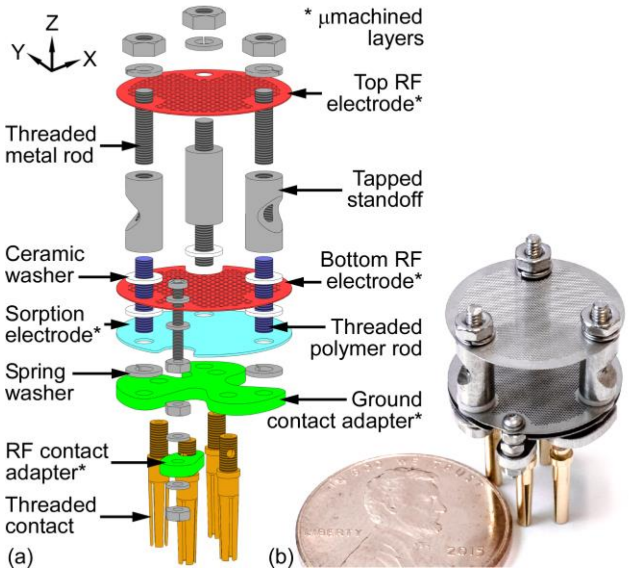

Figure 3-1: (a) The exploded view of the E$^3$TM. Threaded contacts and customized adapters are used to create mechanical supports and electrical connections for the E$^3$TM. Ceramic washers and threaded polymer rods are utilized to electrically isolate the bottom RF electrode from all other grounded parts. (b) The assembled E$^3$TM.

In the E$^3$TM, a uniform electrical field can be developed over a much larger volume within the trap of the E$^3$TM to enhance RF electron trapping efficiency when compared to the ETM. There are three structural changes account for this improvement. First, all standoffs are located near the edge of the trap and are symmetrically distributed. This placement allows a large, uninterrupted perforated trapping region in the center of the device. Second, a smaller exposed area of isolating ceramic parts is used to minimize unwanted electron charge accumulation to disturb the field uniformity. The exposed area of the ceramic is 58 mm$^2$ in the E$^3$TM compared to 483 mm$^2$ in the ETM. Third, the top and bottom RF electrodes are perforated with the same staggered pattern as the perforated RF electrodes in the ETM, but the electrodes are more finely perforated – a hole diameter of 0.13 mm and hole spacing of 0.23mm in the E$^3$TM, versus a hole diameter of 1.59 mm and hole spacing of 2.39 mm in the ETM – to minimize the presence of the fringing electric field near the electrodes, as shown in Fig. 3-2.

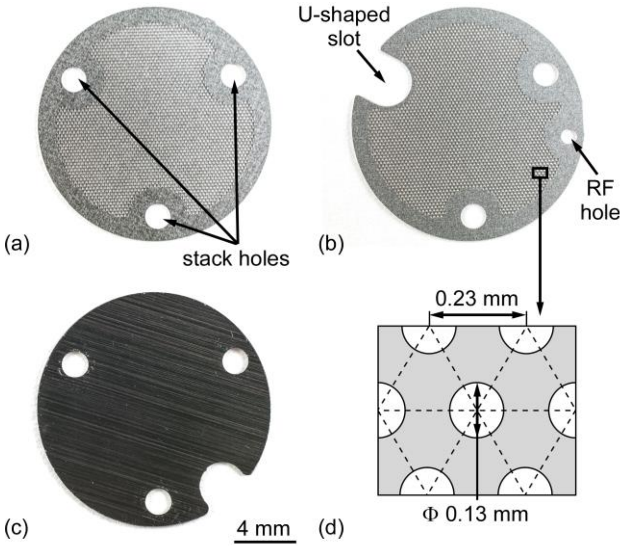

Figure 3-2: Electrodes in the $E^3$TM. (a) Top RF electrode. (b) Bottom RF electrode. (c) Sorption electrode. (d) Staggered perforation pattern. (The scale of (a) – (c) is shown in (c)).

A 2D axisymmetric electrostatic simulation model (COMSOL Multiphysics) is used to investigate the fringing electric field near a single perforation (electric field in the radial direction, which corresponds to directions perpendicular to the Z direction in Fig. 3-1) for both the ETM and the $E^3$TM as shown in Fig. 3-3 (a). In the model, the top RF electrode is biased at 140 V, while the bottom RF electrode is grounded. The simulation result with the ETM geometry has a 1 V/m fringing field 3.3 mm away from the RF electrode, while the model with the $E^3$TM geometry has a 1 V/m fringing field only 0.28 mm away from the RF electrode, as shown in Figs. 3-3 (b) and (c). Therefore, the fringing electric field is significantly reduced with the finer perforations used in the $E^3$TM. Thus, the electrons in the trap are expected to have substantially reduced lateral drift and accordingly longer lifetimes within the trap.

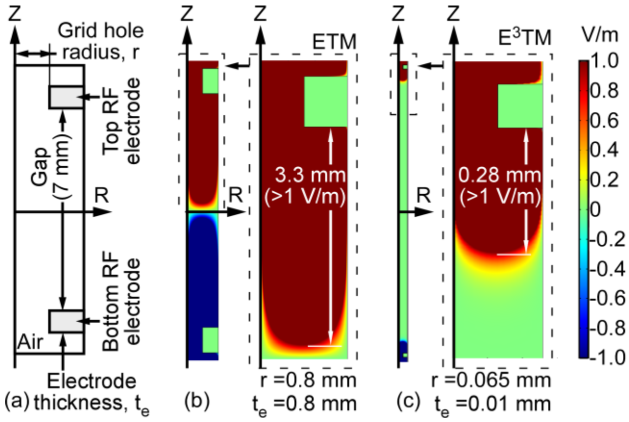

Figure 3-3: (a) The geometry of the 2D axisymmetric electrostatic model used to investigate the fringing electric field (electric field in the R direction, which is the directions perpendicular to the Z direction in Fig. 3-1) near the RF electrodes. The top RF electrode is biased at 140 V, while the bottom RF electrode is grounded. The thickness of both RF electrodes is $t_e$, and the hole radius is $r$. The gap between electrodes is fixed at 7 mm. (b) The cropped simulated fringing electric field with the perforation geometry of the ETM. The fringing field is larger than 1 V/m up to 3.3 mm into the inter-electrode space. (c) The cropped simulated fringing electric field with the perforation geometry of the $E^3$TM. The fringing electric field is larger than 1 V/m up to 0.28 mm into the inter-electrode space.

Two more improvements are incorporated into the design of the $E^3$TM when compared to that of the ETM [Den17]. First, fewer metal electrodes are stacked into the $E^3$TM; this reduces parasitics and simplifies RF characterization. Second, the trap-to-device volume ratio is increased from 8.6% for the ETM to 75.7% for $E^3$TM to maintain a similar trap size while dramatically shrinking the device footprint.

For the purpose of assembly and electrical connections, the U-shaped slot, RF hole, and stack holes are placed near the edges of the RF electrodes as shown in Fig. 3-2. To hold the stack together, threaded rods are screwed through the standoffs and stack holes, and then bolted to the nuts and tapped holes on the ground contact adapter. The electrical isolation of the bottom RF electrode is realized through two aspects. First, threaded polymer rods and ceramic washers are used where rods are in contact with the bottom RF electrode.  Additionally, a safe clearance is maintained between the U-shaped slot on the bottom RF electrode and the standoff that passes through it.  Such a configuration allows all metal parts to be grounded properly.  A total of four copper contacts (Accu-Glass Inc., 100181) are threaded outside their crimp barrel and pushed on feedthrough pins.  One of the contacts is screwed into the RF contact adapter to supply the RF signal to the bottom RF electrode.  The rest of the contacts are screwed through tapped holes on the ground contact adapter and tightly pushed toward the sorption electrode for reliable grounding, as three spring washers are placed between the sorption electrode and the ground contact adapter to provide extra space for these contacts to be screwed through.

Two sets of holes are perforated on adapters to not only fit the pin pattern from the feedthrough but also to adapt this pattern to the assembled electrodes.  As shown in Fig. 3-4 (a), the ground contact adapter is designed to ground the $E^3$TM, except for the bottom RF electrode where the RF signal is applied.  Six tapped holes are located on this adapter, three of which are aligned with stack holes on all the electrodes, while the three other are aligned to pins from the electrical feedthrough.  Material is removed from the ground contact adapter where possible in order to reduce the gas load and to allow room for another RF contact adapter as shown in Fig. 3-4 (b).  This RF contact adapter is only used to route the RF signal from the feedthrough to the bottom RF electrode.  Detailed drawings of the three electrodes and the two adapters are shown in Appendix A.

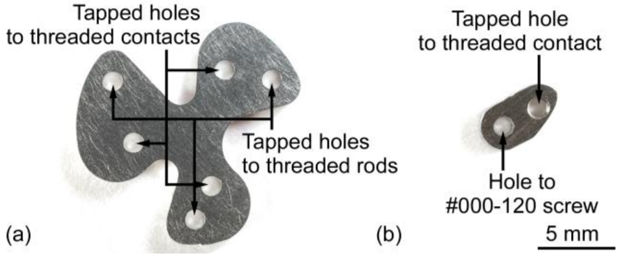

Figure 3-4: Adapters in the $E^3$TM. (a) Ground contact adapter. (b) RF contact adapter. (The scale for both adapters is shown in (b)).

The ETM was only designed to provide a preliminary proof-of-principle for RF trapping of electrons, and did not include any consideration toward physical or chemical pumping. In the $E^3$TM, a goal in addition to enhanced trapping efficiency is incorporation of considerations that may lead to physical or chemical pumping. Two such considerations are included in the $E^3$TM structure. First, the RF electrodes are made from titanium to produce auxiliary pumping of reactive gas species such as oxygen and nitrogen. Fresh titanium, a widely used gettering material, is sputtered during ion neutralization [Sto55]. Second, a sorption electrode is placed between the bottom RF electrode and the ground contact adapter. As described in the introduction, ionized inert gas molecules are pumped by physically burying into the sorption electrode. Tantalum is selected as the sorption electrode material because the ion implantation depth and the diffusion coefficient of tantalum are well balanced to make it suitable for the physical burying of inert gasses [Sch70, Zie03]. While these considerations are included in the $E^3$TM, this work demonstrates only the RF trapping performance with the considerations in place – not full pump operation.

### 3.1.2 Fabrication

Commercially available techniques and parts are leveraged to facilitate fabrication of the $E^3$TM. In particular, the top and bottom RF electrodes are patterned with photochemical machining (PCM) from 0.1 mm thick commercial pure titanium (Photofabrication Engineering Inc.) [Pho17]. Both adapters are patterned with PCM from 1.0 mm thick annealed 304 stainless steel. This is a batch-compatible lithographic process that allows fine perforations to be etched (Fig. 3-5). This process begins with clean metal sheets, which are laminated with dry film photoresist layers on both sides. Double-sided exposure and developing follows, resulting in the transfer of structural features to the hardened photoresist masks. The masked sheets are sprayed with an etchant to etch from both sides, which attacks and removes the exposed metal. For the titanium parts, a copper-based proprietary etchant is used, while ferric chloride is used for the stainless steel. Finally, the remaining photoresist is stripped off the released parts.

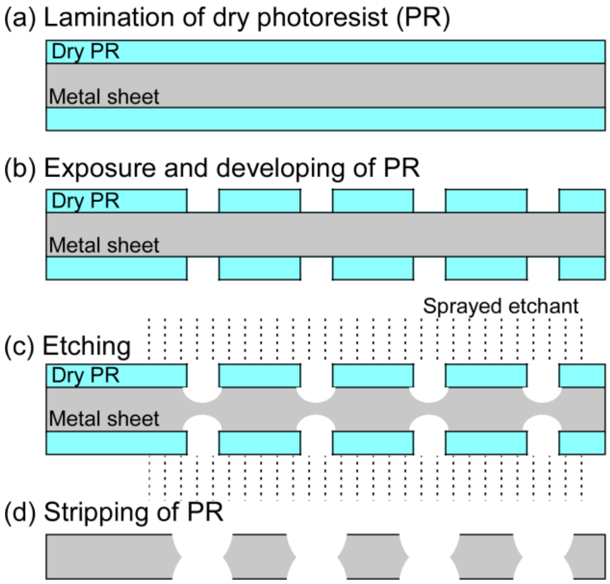

Figure 3-5: The fabrication process of PCM. (a) Lamination of photoresist on the metal sheet. (b) Exposure and development of the photoresist. (c) Etching the metal sheet with sprayed etchant. (d) Stripping the photoresist off the released parts.

For the sorption electrode, the U-shaped slot and stack holes are machined with high precision using micro-electro-discharge machining (SmalTec$^{TM}$, EM203) from a 0.20 mm thick tantalum disk with high precision (Goodfellow, 012-928-68, tantalum disk, OD: 15.00 mm) [Ma15, Mas 90, Sma17]. This is also a batch-compatible micromachining process, although a serial mode is used in fabricating the sorption electrode [Tak02]. An electric discharge is maintained and controlled between the tool (a tungsten wire) and the workpiece (tantalum disk) to continuously remove materials. Dielectric oil is used as a discharge medium to flush away the removed materials and to dissipate the heat during machining.

Other parts of the E$^3$TM are commercially available standard parts, as shown in Table A-2. Some of these parts are tailored to desired geometries through traditional machining processes. To prevent a virtual leak, V-shaped openings are cut into the tapped standoffs in which the threaded rods are screwed. The ceramic washers are comprised of machinable Macor® – mica glass ceramic – and their outer diameter is reduced by grinding to 1/8" (3.2 mm) [Mac16]. The polymer-threaded rods are threaded and cut from acetal rod; acetal is a chemical and moisture resistant polymer that has low outgassing rate, which is widely used in various vacuum products [Del17]. These non-metallic parts are mainly enclosed in or covered by grounded metal parts to minimize their exposed surfaces and prevent unwanted charge accumulation. Although the E$^3$TM has a more complex material composition than the ETM, all materials in the E$^3$TM are UHV compatible and exhibit low outgassing rates [Els75, Sgo06]. The assembled E$^3$TM is shown in Fig. 3-1 (b).

## 3.2 Experimental Setup

To test the RF electron trapping performance of the $E^3$TM, a compact 1.33" CF flange vacuum system is assembled to the original vacuum chamber that was used for testing the ETM, and an electrical setup is developed.

### 3.2.1 Vacuum System

The $E^3$TM is built on a 1.33" CF flange for quick vacuum installation. Although a flange reducer can be used to install the $E^3$TM along with the 1.33" CF flange on the 2.75" CF vacuum chamber used in characterizing the ETM, another smaller spherical cube vacuum chamber (Kimball Physics, MCF133-SphCube-A6) that only supports 1.33" flanges has been identified to install and test the $E^3$TM [Kim17]. This 1.33" CF vacuum chamber has six ports with an internal volume of 16 cc, compared to 366 cc in the 2.75" CF vacuum chamber to which the ETM is attached [Den17]. The original electron gun and the customized 2.75" CF full nipple are detached from the right side of the 2.75" CF chamber, and the 1.33" chamber is then assembled to the 2.75" CF chamber through a 2.75" CF to 1.33" CF reducer (Kimball Physics, MCF275-FlgAdptr-C1A1), as shown in Fig. 3-6. All vacuum gauges and pumps that belong to the previous vacuum system are still used to monitor and pump the 1.33" CF chamber. As shown in Fig. 3-6 (a), the feedthrough that mechanically supports and electrically connects to the $E^3$TM is assembled to the front side of the 1.33" CF chamber, and a spare 9-pin electrical feedthrough is assembled to the top side of the 1.33" CF chamber for the purpose of characterization.

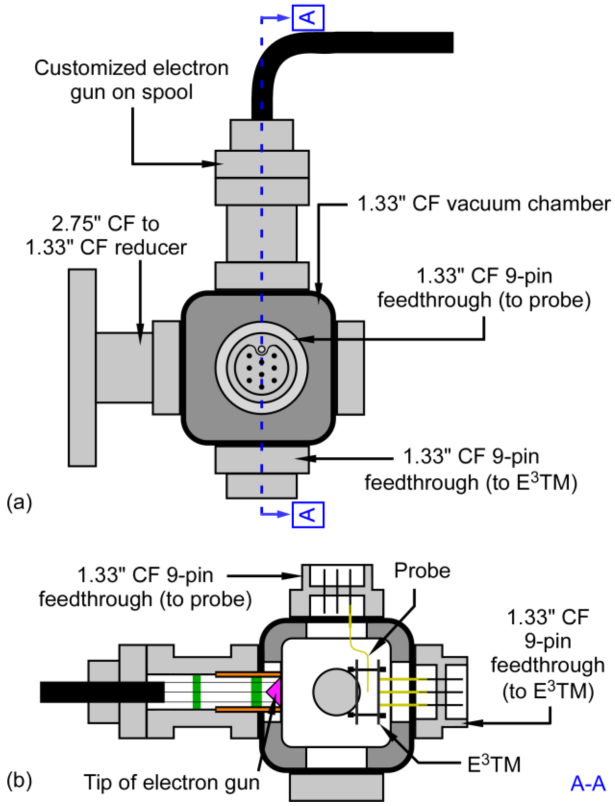

Figure 3-6: The modified vacuum system for the E$^3$TM is attached to and pumped by a 2.75" CF vacuum system via a 2.75" CF to 1.33" CF reducer. The E$^3$TM is built on top of a 9-pin electrical feedthrough and is placed on the front side of the 1.33" CF chamber. The customized electron gun is mounted on a 1.33" CF spool and attached to the 1.33" CF chamber, with its gun barrel tip 15 mm away from the E$^3$TM. A curved probe is routed to the center of the trap from a spare 9-pin electrical feedthrough on top of the 1.33" CF chamber. (a) Top view. (b) A-A section view.

An electron gun is used to supply electrons for testing the electron trap. This gun has a 1.33" CF flange connection and has been customized by Kimball Physics, as shown in Fig. 3-7. The insertion length of this customized electron gun is only 1.62" (4.12 cm), compared to 6" (15.24 cm) for the previous electron gun [Den17]. A 1.40" (3.56 cm) spool is pre-assembled on the 1.33" CF electron gun to enable a 0.22" (0.56 cm) insertion of the gun tip into the 1.33" CF chamber from the back. Therefore, the gun tip is 15 mm away from the top RF electrode of the E$^3$TM. The other two ports of the 1.33" CF chamber are assembled with blank flanges (Kurt J. Lesker®, F0133X000N) to seal the vacuum.

Although this work is focused on demonstrating enhanced electron trapping efficiency with the developed E$^3$TM, the modified vacuum system is well designed for the final pumping demonstration as well. Once a gate valve is assembled between the reducer and 1.33" CF chamber, and a blank flange is replaced with a micro ion gage, this 1.33" CF chamber system has a small dead volume and can be isolated from the rest of the vacuum system to demonstrate gas pumping due solely to the E$^3$TM device.

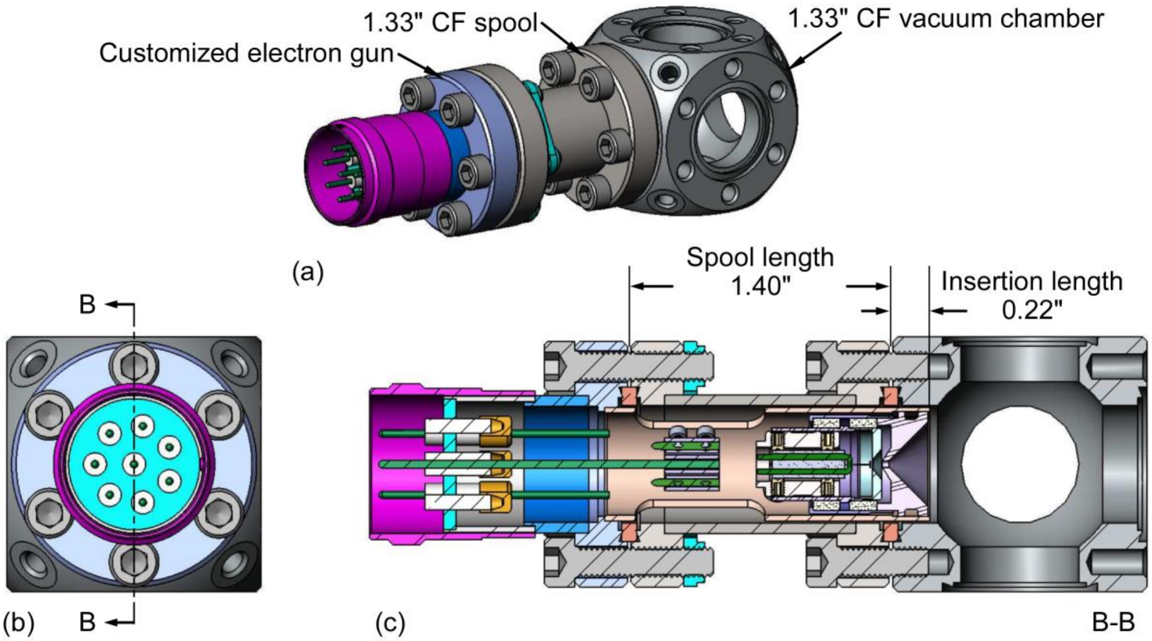

Figure 3-7: Customized electron gun assembled on the 1.33" CF vacuum chamber. (a) 3D schematic. (b) Left view. (c) B-B section view. (Solid models courtesy of Kimball Physics)

### 3.2.2 Electrical Testing

The electrical setup inside the vacuum chamber is adjusted and simplified as compared to the ETM [Den17]. As shown in Fig. 3-8, a curved metal wire probe with a tip that is directed toward the center of the trap serves as a probe for characterizing the RF electron trap in the E$^3$TM. This stands in contrast to using two planar collectors to probe the RF electron trap from the side as in the ETM. This probe is made from 0.25 mm diameter silver plated copper wire and clamped on a contact, which is to be pushed into the spare 1.33" CF 9-pin electrical feedthrough for electrical connection. This wire probe is advantageous for two reasons. First, the wire has a much smaller surface area than the collectors, which will result in less perturbation of the established electron trap. Second, the electron trap will be probed in the center of the trap where the electron density is mostly concentrated, rather than at the periphery of the trap.

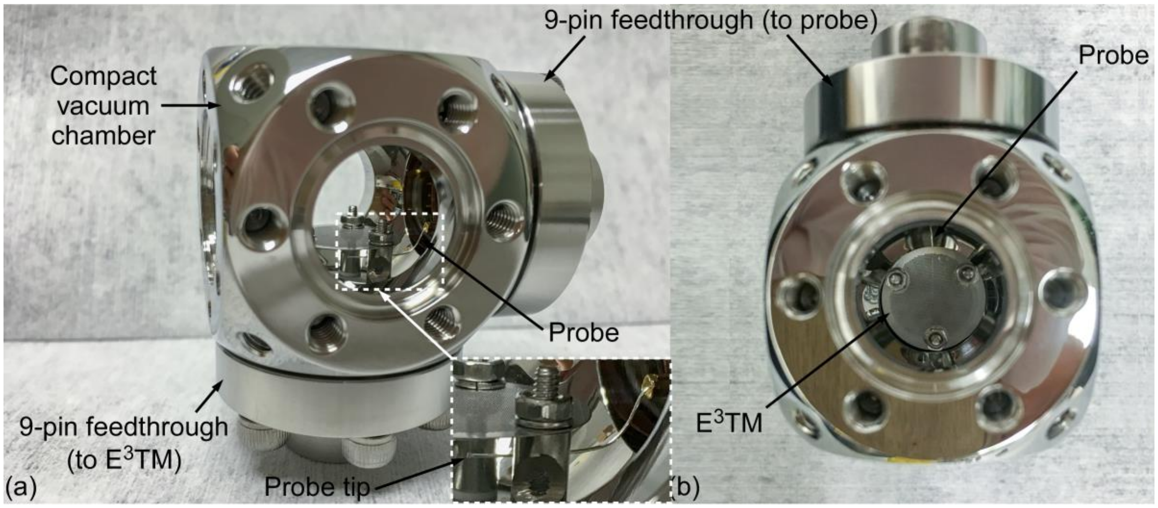

Figure 3-8: Probe used in characterizing the RF electron trap for the E$^3$TM. The probe and E$^3$TM are assembled to the compact vacuum chamber to show their relative positions from (a) side and from (b) top.

Outside the vacuum chamber, the unused pins of the electrical feedthroughs are grounded properly to minimize the parasitics introduced into the circuit loop where the E$^3$TM is operated. For the electrical feedthrough that routes the RF signal to the E$^3$TM, five closely packed unused pins are electrically grounded to the feedthrough flange through a grounding fixture. As shown in Fig. 3-9 (a), this grounding fixture consists of five contacts and a 304 stainless steel plate. Contacts are shortened to 7.2 mm in length from the crimp side as shown in Fig. 3-10. The plate (thickness: 0.048" (1.22 mm)) is shaped to cover only the area where the pins need to be grounded and where the #4-40 connector thread is located on the feedthrough. A hole is drilled on the plate to align with the #4-40 connector thread on the flange. Shortened contacts are soldered onto the plate and pushed on unused pins, and the plate is then grounded to the flange by tightening a #4-40 screw into the flange as shown in Fig. 3-9 (b). KAPTON® tape is wrapped around the edge of the plate to ensure electrical isolation between the grounding fixture and the contacts that route to the E$^3$TM [DUP17]. For the electrical feedthrough that connects to the probe, eight unused pins are grounded together through another customized grounding fixture, as shown in Fig. 3-11.

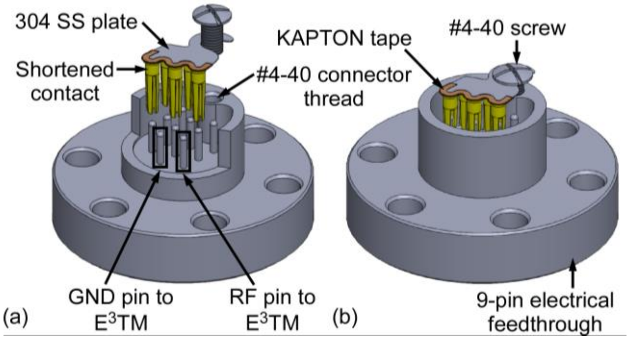

Figure 3-9: Grounding fixture on 9-pin electrical feedthrough that supports the E$^3$TM. (a) Explosive view with partially cropped feedthrough flange. (b) Grounding fixture assembled to the feedthrough.

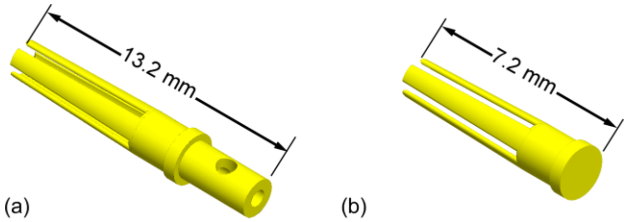

Figure 3-10: Contact used in grounding fixtures. (a) Contact at its full length. (b) Shortened contact.

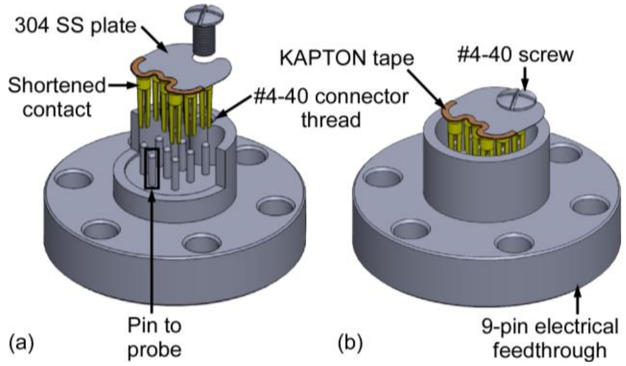

Figure 3-11: Grounding fixture on 9-pin electrical feedthrough that routes to the probe. (a) Explosive view with partially cropped feedthrough flange. (b) Grounding fixture assembled to the feedthrough.

There are a few discrete components that are set outside the vacuum chamber to help establish and diagnose the electron trap for the E$^3$TM, as shown in the electrical testing setup (Fig. 3-12). An inductor $L_1$ is soldered to a contact and then pushed on the feedthrough pin to which the bottom RF electrode is connected, while the other end of the $L_1$ is soldered to the center conductor of a 69 cm long customized RG 58 C/U coaxial cable [RG17]. The braided shield of this coaxial cable is soldered to another contact that is pushed on a pin to where the E$^3$TM is grounded. This not only realizes the electrical connection to the E$^3$TM, but also allows the RF characteristics of the E$^3$TM to be tuned with the external $L_1$ by adjusting its inductance outside the vacuum chamber.

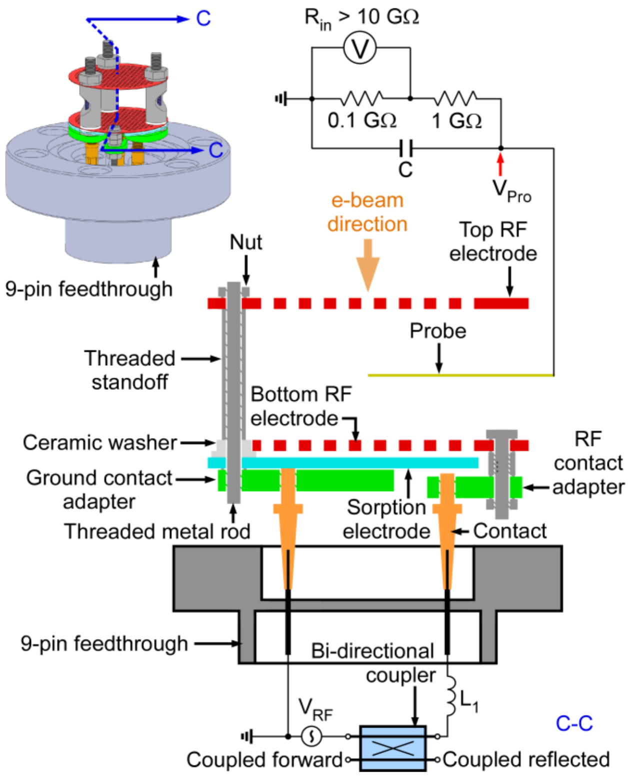

Figure 3-12: The electrical testing setup for the RF electron trapping of the $E^3$TM. An 86 pF capacitor $C$ is placed in between the ground and the probe to float the probe. The potential across the probe capacitor is measured with a voltmeter through a high impedance voltage divider. The bottom RF electrode is RF powered through a bi-directional coupler and an inductor $L_1$. The forward RF power can be directly measured during the testing.

A bi-directional coupler (Mini-Circuits®, ZFBDC20-62HP+) that works from 10 MHz to 600 MHz is added into the setup to allow forward and reflected RF power ($P_{fwd}$ and $P_{ref}$) measurement during testing, rather than estimate the RF power based on the developed circuit model in the ETM [Bid17]. As shown in the schematic of the bi-directional coupler (Fig. 3-13), the main line is connected between $L_1$ and the RF source to couple $P_{fwd}$ and $P_{ref}$ 20 dB less at the coupled ports. The bottom RF electrode is DC shorted to ground as all four ports of the bi-directional coupler are DC shorted to ground through the large inductor $L_G$ (around 10 μH).

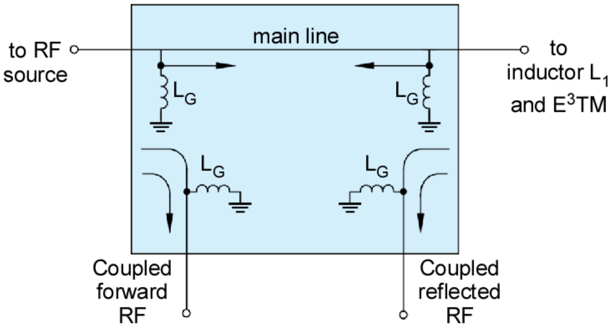

Figure 3-13: Schematic of the bi-direction coupler with four ports. The RF signal is routed through the main line coupled through two coupled ports [Bid17].

Similar to the electrical setup in the ETM, a capacitor *C* (86 pF) is placed in series with the probe to DC isolate the probe from the ground [Den17]. This prevents the trapped electrons from leaking through the probe [Sug98]. In turn, electrons accumulate on it to establish a negative probe potential $V_{Pro}$. As the electrons are being trapped within the trapping region under a specific RF signal, a steady state average electron density is reached to build up a corresponding steady state probe potential $V_{Pro\_ss}$ at the probe. Higher electron densities near the probe will result in higher electron current through the probe, and thus a more negative $V_{Pro\_ss}$. A voltage divider that consists of a 1.0 GΩ and a 0.1 GΩ resistor in series is placed in parallel with the capacitor *C* to create a reference voltage in measuring the $V_{Pro\_ss}$. Then, the reference voltage across the 0.1 GΩ resistor is measured by a digital multimeter (Agilent, 34401A) with an input impedance of 10 GΩ. Thus, the resistive load in parallel with the capacitor is 1.1 GΩ in total, which is high enough to avoid draining out all the accumulated electrons at the probe.

## 3.3 Electrical Characteristics

### 3.3.1 RF characterization

As described in Chapter 2, an ideal RF electron trap in the context of this thesis is one in which electrons travel the entire gap between parallel RF electrodes. In order to identify the ideal forward RF power $P_{fwd}^{*}$ and the RF frequency $f_{RF}$ to operate the E$^3$TM for ideal electron trapping, the RF characteristics of the E$^3$TM are characterized and an equivalent circuit model that represents the E$^3$TM is developed. The impedance of the E$^3$TM along a 0.69 m long RG58 C/U coaxial cable $Z_{in}$ is measured from 2 MHz to 400 MHz via the impedance analyzer (Agilent, 4395A). With the help of the lossless transmission line equation, the impedance of the E$^3$TM $Z_{L2}$ can be de-embedded from the measured $Z_{in}$ at the coaxial cable-impedance analyzer junction [Qia09]:

$$Z_{in} = Z_0 \frac{Z_{L2} + jZ_0 \, tan\left(\frac{2\pi f_{RF}}{k_v c} L\right)}{Z_0 + jZ_{L2} \, tan\left(\frac{2\pi f_{RF}}{k_v c} L\right)} \tag{3-1}$$

where $Z_0$ is the characteristic impedance of the cable (50 Ω), $c$ is the speed of light ($3 \times 10^8$ m/s), $f_{RF}$ is the RF frequency in Hz, $k_v$ is the velocity propagation factor of the RG58 C/U cable (0.66), and $L$ is the length of the cable (0.69 m) [RG17]. As shown in Fig. 3-14, the de-embedded $Z_{L2}$ (solid impedance trace) only presents one series resonant dip within the characterized frequency range at the series resonant frequency $f_0$ (366 MHz), compared to seven series resonant dips in the de-embedded impedance of the ETM [Den17]. This was expected as unused electrodes in the ETM were removed when designing the E$^3$TM. In addition, the reflection coefficient $\Gamma$ can be calculated with the $P_{ref}$ and $P_{fwd}$ measured by the bi-directional coupler:

$$\Gamma = \sqrt{\frac{P_{ref}}{P_{fwd}}} \tag{3-2}$$

At $f_0$ of the E$^3$TM, the $\Gamma$ should theoretically reach its lowest value; this property can be used to verify $f_0$ that is identified from the de-embedded $Z_{L2}$. From the measured $\Gamma$, it was observed that the difference between experimentally measured $f_0$ and de-embedded $f_0$ is less than 0.5%.

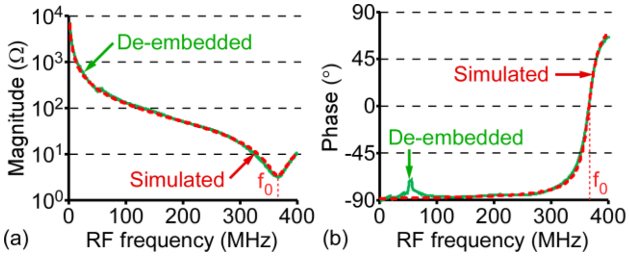

Figure 3-14: (a) Magnitude and (b) phase of the de-embedded E$^3$TM impedance $Z_{L2}$ (green solid traces) and the simulated E$^3$TM impedance (red dashed traces) from 2 MHz to 400 MHz. The series resonance of the E$^3$TM is located at $f_0$ (366 MHz).

Based on the de-embedded impedance of the E$^3$TM, an equivalent circuit model that consists of four components is developed to electrically represent the E$^3$TM (Fig. 3-15). This model has four components. The capacitor $C_{L2}$ is the total shunt capacitance between the bottom RF electrode and the ground. Thus, a portion of the $C_{L2}$ is the electrical representation of the electron trap, as this trap is formed between the RF-driven bottom RF electrode and the grounded top RF electrode. Before the vacuum installation of the E$^3$TM, the $C_{L2}$ is measured with an LCR meter (Hewlett-Packard, 4284A) at a testing frequency of 1 kHz, and the measured $C_{L2}$ is 5.77 pF. The other three circuit components are parasitics, two of which are in series with the $C_{L2}$ – series stray resistance and inductance ($R_{L2\_p}$ and $L_{L2\_p}$), and one of which is in parallel with the $C_{L2}$ – parallel stray capacitance ($C_p$). These parasitics are due to the contact resistance, self-inductance of metal parts, and capacitance that results from the testing setup [Hay11].

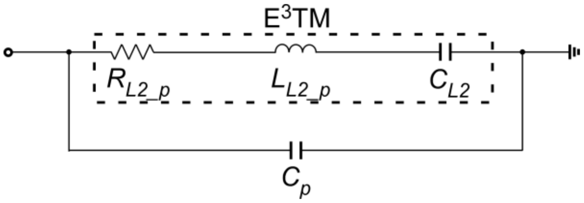

Figure 3-15: The equivalent circuit model of the E$^3$TM. The capacitor $C_{L2}$ is the electrical representation of the RF electron trap. $R_{L2\_p}$, $L_{L2\_P}$, and $C_p$ are parasitics.

Based on the measured $C_{L2}$, $C_{L2}$ and $L_{L2\_p}$ are tuned simultaneously to result in not only a series resonant frequency at $f_0$ but also an impedance profile near $f_0$ similar to the measured profile. Then, $R_{L2\_p}$ is determined by the magnitude of $Z_{L2}$ at $f_0$ because reactance from $C_{L2}$ and $L_{L2\_p}$ are canceled out at $f_0$. The simulated impedance of this series RLC circuit is already a precise match to the $Z_{L2}$ near $f_0$. Finally, a proper capacitance value of $C_p$ is selected to improve the match between simulated and de-embedded impedances over the full characterized frequency range. The values of circuit components are summarized in Table 3-1. The SPICE simulated impedance of the E$^3$TM (dashed impedance trace, Fig. 3-14) closely matches with the measured impedance, especially near $f_0$. Thus, the peak RF voltage $|V_{RF}|$ that develops across the E$^3$TM during RF electron trapping for a given RF power can be estimated with the calculated $|V_{RF}|$ on $C_{L2}$ in the model.

Table 3-1: Circuit components in the equivalent circuit model of the E$^3$TM.

| Circuit components | $R_{L2\_p}$ | $L_{L2\_p}$ | $C_{L2}$ | $C_p$ |
|---|---|---|---|---|
| Values | 3.4 Ω | 21.8 nH | 8.68 pF | 3.65 pF |

### 3.3.2 Lowering Series Resonant Frequency $f_0$

For power efficiency purposes, the ETM was operated at its series resonant frequency $f_0$ to take advantage of voltage amplification at that frequency [Den17]. However, the E$^3$TM has a much higher $f_0$ than the ETM. According to the analytical model of the idealized geometry in Chapter 2, the ideal RF voltage $|V_{RF}^*|$ is 738 V to result in the electron traveling the entire 7 mm interelectrode gap at 366 MHz. This RF voltage corresponds to an excessively high RF power for the E$^3$TM – a $P_{fwd}$ of 1.5 kW. When operated with excessive RF power, the E$^3$TM is likely to experience a significant temperature increase as power is dissipated through heat, which will result in excessive outgassing. As an alternative, an external inductor $L_1$ is connected in series with the E$^3$TM to lower the series resonant frequency at which the E$^3$TM will be operated, as shown in the stated electrical testing setup (Fig. 3-12). There are a few advantages of this experimental approach. First, the lowered series resonant frequency $f_{0\_l}$ allows the E$^3$TM to consume less RF power, while still resulting in an ideal electron trap. Second, the $L_1$ provides an external parameter to make the operating frequency of the E$^3$TM tunable, compared to operating it at a fixed RF frequency. Third, the $L_1$ can be added to the equivalent circuit model and used to verify the credibility of the model by comparing the simulated impedance and the measured impedance, because the $L_1$ is a known quantity.

As this work is an intermediate step towards the final gas pumping demonstration, the ideal RF voltage $|V_{RF}^*|$ should be at least 50 V to ensure that RF energized electrons have enough kinetic energy to ionize the gas molecules. The corresponding RF frequency for this $|V_{RF}^*|$ is around 90 MHz, which is the target lower limit for $f_{0\_l}$. For any specified $f_{0\_l}$, the required inductance $L_1$ can be estimated with Equation (3-3) by assuming that an ideal $L_1$ is in series with the series RLC branch that belongs to the equivalent circuit model. Therefore, the inductance of $L_1$ cannot exceed 339 nH.

$$L_1 = \left[\left(\frac{f_0}{f_{0\_l}}\right)^2 - 1\right] \times L_{L2\_p} \tag{3-3}$$

There are a few criteria for selecting the $L_1$ from a commercially available source. First, the self-resonant frequency of the $L_1$ must be high enough (e.g. 300 MHz) to behave like an inductor at $f_{0\_l}$. Second, the rated current of the $L_1$ must be in ampere level appropriate for the potential high power operation, since the E$^3$TM will be operated at a high current level to achieve a large $|V_{RF}|$ at $f_{0\_l}$. Third, the DC resistance of the $L_1$ must be small enough (e.g. a few mΩ) to avoid lowering the resulting current at the same power level at $f_{0\_l}$.

An $L_1$ with an inductance of 150 nH (VISHAY®, 541-1522-ND) is applied outside the vacuum chamber to lower the $f_0$ of the E$^3$TM. From the manufacturer specifications of this inductor, this $L_1$ has a current rating of 2.45 A, a DC resistance less than 30 mΩ, and a self-resonant frequency at 525 MHz. Based on Equation (3-3), this inductor should result in an $f_{0\_l}$ of 130.4 MHz. The impedance of the E$^3$TM in series with this $L_1$ is measured along the coaxial cable and de-embedded through Equation (3-1) from 2 MHz to 400 MHz. As shown in the de-embedded impedance of the E$^3$TM in series with an $L_1$ of 150 nH $Z_{L2\_150}$ (Fig. 3-16), the series resonant frequency is shifted from 366 MHz to 141.3 MHz.

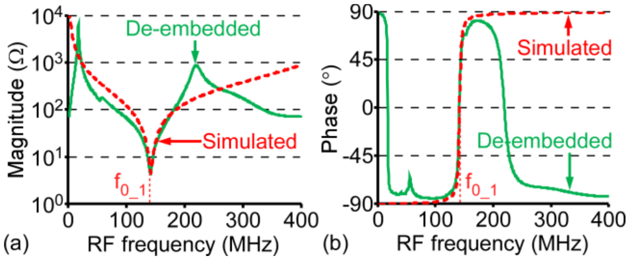

Figure 3-16: (a) Magnitude and (b) phase of the de-embedded impedance of the E$^3$TM with a series $L_1$ of 150 nH $Z_{L2\_150}$ (green solid traces) and the simulated $Z_{L2\_150}$ (red dashed traces) of the simplified equivalent circuit model as shown in Fig. 3-17 (b) from 2 MHz to 400 MHz. The lowered series resonant frequency of the E$^3$TM $f_{0\_l}$ is 141.3 MHz when the $L_1$ is 150 nH.

To address the shifting of the $f_0$ in the circuit model, an inductor with an inductance of $L_1$ can be put in series with the series RLC branch in the developed circuit model to update that branch as shown in Fig. 3-17 (a). Additionally, two parallel resonant peaks emerge in the characterized frequency range in the de-embedded impedance trace. In the electrical testing setup, a large DC shorting inductor $L_G$ is in parallel with the series inductor $L_1$ and the E$^3$TM once the bi-directional coupler is attached, because all four ports of the bi-directional coupler are DC shorted to ground through the large inductor $L_G$ (around 10 μH). This leads to the parallel resonant peak at 20 MHz. To coordinate this peak in the circuit model, a 10 μH inductor $L_G$ can be put in parallel with the series RLC branch. Another parallel resonant peak at 240 MHz may result from the $C_p$, the previously identified parallel parasitic capacitor in the equivalent circuit model shown in Fig. 3-15. Note that the impedances of these two parallel branches are at least two orders of magnitude higher than the $Z_{L2\_150}$ at the $f_{0\_l}$. Therefore, both parallel circuit components are negligible (and can be treated as open branches) at $f_{0\_l}$ because the impedance is dominated by the circuit components that represent the E$^3$TM and the $L_1$.

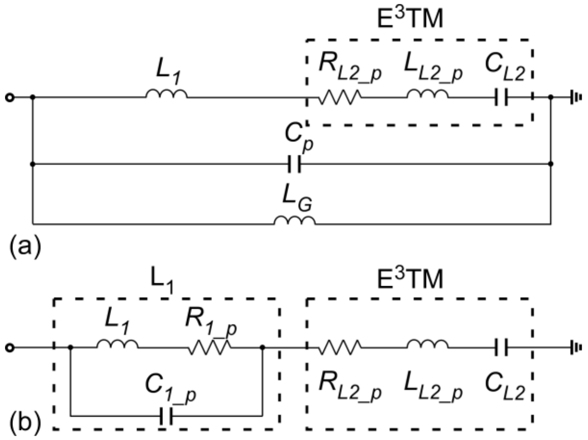

Figure 3-17: (a) The equivalent circuit model with the considerations of the bi-directional coupler and the series inductor $L_1$. (b) The simplified equivalent circuit model of the E$^3$TM with a series inductor $L_1$. A non-ideal inductor model is used to represent the $L_1$, and the E$^3$TM is represented by a series RLC circuit. The model is simplified to match the de-embedded $Z_{L2\_150}$ only at $f_{0\_l}$.

The equivalent circuit model is further simplified for the E$^3$TM with a series $L_1$, as shown in Fig. 3-17 (b). A non-ideal circuit model of the inductor is adapted to the model to represent the inductor $L_1$. Parasitic capacitance and resistance of the $L_1$ ($C_{1\_p}$ and $R_{1\_p}$) are determined from its data sheet. Circuit components that cause parallel resonances are neglected in the simplified circuit model, because these components are non-dominant at $f_{0\_1}$, where the E$^3$TM is operated. The values of $R_{L2\_p}$, $L_{L2\_p}$, and $C_{L2}$ from the original equivalent circuit model are slightly adjusted with the known circuit components of the $L_1$ to result in a simulated $Z_{L2\_150}$ with similar resonant properties near $f_{0\_l}$ to those of the de-embedded $Z_{L2\_150}$. The SPICE simulated $Z_{L2\_150}$ is shown in Fig. 3-16 (dashed impedance traces), and the component values of the simplified circuit model for an $L_1$ of 150 nH are listed in Table 3-2.

Table 3-2: Circuit components in the simplified circuit model of the E$^3$TM with a series $L_1$. $L_1$ is listed at both 150 nH and 330 nH.

| Lowered series resonant frequency $f_{0\_l}$ (MHz) | $L_1$ (nH) | $R_{1\_p}$ (Ω) | $C_{1\_p}$ (pF) | $R_{L2\_p}$ (Ω) | $L_{L2\_p}$ (nH) | $C_{L2}$ (pF) |
|---|---|---|---|---|---|---|
| 141.3 | 150 | 0.03 | 0.613 | 4.5 | 24.3 | 6.83 |
| 96.9 | 330 | 0.22 | 0.457 | 5.2 | 24.3 | 7.22 |

Another $L_1$ with an inductance of 330 nH (API Delevan®, 1025R-08K) is used in lowering the series resonant frequency of the E$^3$TM to further verify the simplified equivalent circuit model. From the manufacturer specifications of this inductor, this $L_1$ has a current rating of 0.83 A, a DC resistance of 220 mΩ, and a self-resonant frequency at 410 MHz. The impedance of the E$^3$TM with this 330 nH $L_1$ is measured and de-embedded as shown by $Z_{L2\_330}$ in Fig. 3-18 (solid impedance traces). The estimated $f_{0\_l}$ is 91.1 MHz based on Equation (3-3), which is only 6% smaller than the measured $f_{0\_l}$ at 96.9 MHz. The known component values of $L_1$ of 330 nH are adapted into the simplified circuit model. By slightly adjusting (by less than 10%) some of the component values identified in the case of $L_1$ at 150 nH, the simulated $Z_{L2\_330}$ (dashed impedance traces, Fig. 3-18) is perfectly matched with the de-embedded $Z_{L2\_330}$ near the $f_{0\_l}$. The component values for the case of $L_1$ of 330 nH are listed in Table 3-2. This set of results indicates that the simplified circuit model is a good electrical representation for the E$^3$TM with series $L_1$.

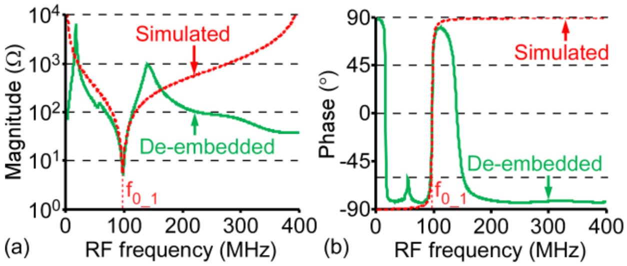

Figure 3-18: (a) Magnitude and (b) phase of the de-embedded impedance of the $E^3$TM with a series $L_1$ of 330 nH $Z_{L2\_330}$ (green solid traces) and a simulated $Z_{L2\_330}$ (red dashed traces) of the simplified equivalent circuit model as shown in Fig. 3-17 (b) from 2 MHz to 400 MHz. The lowered series resonant frequency of the $E^3$TM $f_{0\_1}$ is 96.9 MHz when the $L_1$ is 330 nH.

For a specific RF voltage $|V_{RF}|$ to operate an RF electron trap at $f_{RF}$, the required $P_{fwd}$ can be estimated with the simplified circuit model for both $L_1$ cases using the following steps [Gra91]. First, the $|V_{RF}|$ developed across the electron trap is electrically represented by the peak RF voltage developed across the $C_{L2}$ in the simplified circuit model. Thus, the peak current through the $C_{L2}$ ($I_{C_{L2},peak}$) can be derived with Equation (3-4). This $I_{C_{L2},peak}$ is then used in deriving the peak RF voltage across the $E^3$TM and the series $L_1$ ($V_{L2,peak}$) with Equation (3-5), in which $Z_{L2}$ is the measured de-embedded $Z_{L2}$ at $f_{RF}$. Second, the transmitted RF power $P_t$ can be calculated with Equation (3-6), and the reflection coefficient $\Gamma$ can be determined by Equation (3-7). Finally, the $P_{fwd}$ is calculated with Equation (3-8).

$$\left|I_{C_{L2},peak}\right| = 2\pi f_{RF} C_{L2} \times |V_{RF}| \tag{3-4}$$

$$V_{L2,peak} = \left|I_{C_{L2},peak}\right| \times |Z_{L2}| \tag{3-5}$$

$$P_t = \frac{{V_{L2,peak}}^2}{2Z_{L2}} \tag{3-6}$$

$$\Gamma = \frac{Z_{L2}-Z_0}{Z_{L2}+Z_0} \tag{3-7}$$

$$P_{fwd} = \frac{P_t}{(1-|\Gamma|^2)} \tag{3-8}$$

Based on the analytical model in Chapter 2, the calculated ideal RF voltage $|V_{RF}^*|$ is 110.0 V at the lowered $f_{0\_l}$ of 141.3 MHz when $L_1$ is 150 nH and is 51.7 V at the lowered $f_{0\_l}$ of 96.9 MHz when $L_1$ is 330 nH to result in an ideal RF electron trap. By substituting the calculated $|V_{RF}^*|$ at the corresponding $f_{0\_l}$ into Equation (3-4), the required $P_{fwd}$ to operate an ideal RF electron trap can be estimated for the E$^3$TM. For an $L_1$ of 150 nH, the estimated ideal RF signal is at $P_{fwd}^*$ of 3.31 W ($P_t$ of 1.01 W) and $f_{RF}$ of 141.3 MHz. For an $L_1$ of 330 nH, the estimated ideal RF signal is at $P_{fwd}^*$ of 0.40 W ($P_t$ of 0.14 W) and $f_{RF}$ of 96.9 MHz.

## 3.4 Experimental Methods and Results

### 3.4.1 Experimental Methods

For all RF electron trapping tests, the vacuum system is maintained at 4.5 x $10^{-8}$ Torr, and an electron beam is maintained at a 40 µA emission current and 15 eV electron energy. This electron beam is supplied by the customized electron gun and controlled by the controller under the emission current control (ECC) mode to maintain a stable emission status.

The reference steady state probe potential ($V_{Pro\_rss}$) across the DC blocking capacitor with only the presence of the electron beam is measured before the RF electron trapping tests. For the RF electron trapping tests, the $P_{fwd}$ and $P_{ref}$ are experimentally measured with the bi-directional coupler rather than through estimations from the circuit model when compared to the ETM. With the measured $P_{fwd}$ and $P_{ref}$, the experimental obtained transmitted RF power $P_t$ can be derived with Equation (3-9). The steady state probe potential ($V_{Pro\_ss}$) is recorded at ten different RF power levels that include the identified $P^*_{for}$ for both L1. The detailed measurement process was already introduced in Chapter 2.

$$P_t = P_{fwd} - P_{ref} \tag{3-9}$$

### 3.4.2 Experimental Results

The measured $V_{Pro\_rss}$ was repeatable throughout the course of the testing at –12.1 V as shown in Fig. 3-19 and Fig. 3-20 with a blue horizontal line. The measured $P_{fwd}$ and $P_{ref}$, and the corresponding $P_t$ calculated from Equation (3-9) are listed in Table 3-3 for all RF electron trapping tests. The recorded $V_{Pro\_ss}$ at these tested $P_t$ levels are indicated by green data points, and the variations over separate tests are represented by the associated error bars in Fig. 3-19 and Fig. 3-20. Additionally, $|V_{RF}|$ is calculated from Equation (3-4) in the characterized $P_t$ range as shown by $|V_{RF}|$ traces in Fig. 3-19 and Fig. 3-20.

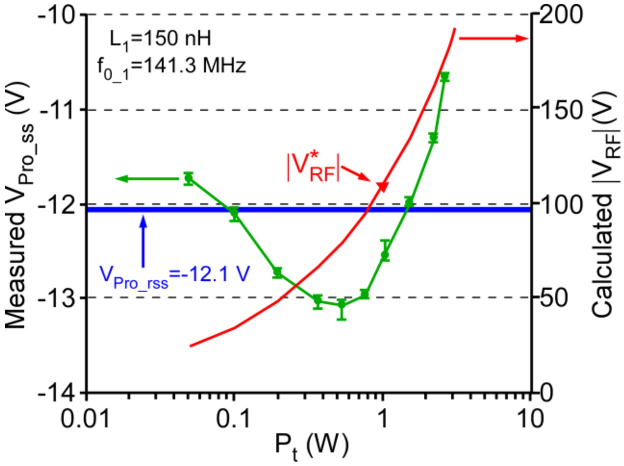

Figure 3-19: The measured steady state probe potential $V_{Pro\_ss}$ (green data points) at different transmitted RF power levels with a fixed $f_{RF}$ of 141.3 MHz and $L_1$ of 150 nH. The blue horizontal line represents the reference steady state probe potential $V_{Pro\_rss}$ with only the injection of the electron beam. The calculated RF voltage $|V_{RF}|$ is plotted within this power range as well.

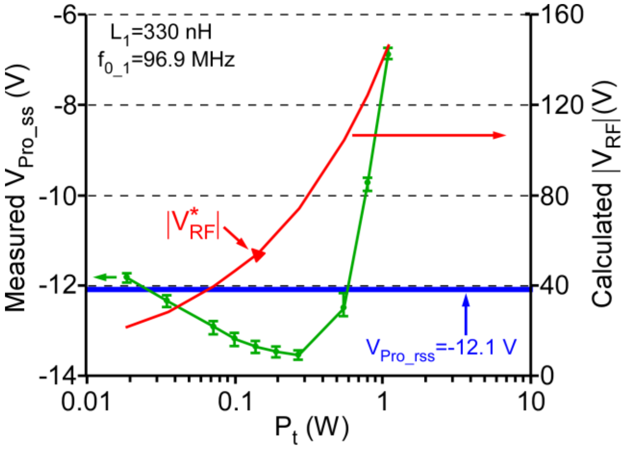

Figure 3-20: The measured steady state probe potential $V_{Pro\_ss}$ (green data points) at different transmitted RF power levels with a fixed $f_{RF}$ of 99.6 MHz and $L_1$ of 330 nH. The blue horizontal line represents the reference steady state probe potential $V_{Pro\_rss}$ with only the injection of the electron beam. The calculated RF voltage $|V_{RF}|$ is plotted within this power range as well.

Table 3-3: The measured $P_{fwd}$ and $P_{ref}$, and corresponding $P_t$ for RF electron trapping tests at $L_1$ of 150 nH and 330 nH.

| $L_1$ = 150 nH | | | | | | | | | | |
|---|---|---|---|---|---|---|---|---|---|---|
| $P_{fwd}$ (W) | 0.149 | 0.281 | 0.534 | 1.022 | 1.438 | 2.000 | 2.746 | 3.888 | 5.704 | 6.904 |
| $P_{ref}$ (W) | 0.099 | 0.180 | 0.339 | 0.650 | 0.900 | 1.245 | 1.723 | 2.386 | 3.496 | 4.297 |
| $P_t$ (W) | 0.050 | 0.101 | 0.195 | 0.372 | 0.538 | 0.755 | 1.023 | 1.502 | 2.208 | 2.607 |
| $L_1$ = 330 nH | | | | | | | | | | |
| $P_{fwd}$ (W) | 0.081 | 0.146 | 0.276 | 0.383 | 0.530 | 0.733 | 1.015 | 1.985 | 2.786 | 3.923 |
| $P_{ref}$ (W) | 0.062 | 0.110 | 0.203 | 0.282 | 0.387 | 0.537 | 0.742 | 1.441 | 2.005 | 2.830 |
| $P_t$ (W) | 0.019 | 0.036 | 0.073 | 0.101 | 0.143 | 0.196 | 0.273 | 0.544 | 0.781 | 1.093 |

For $L_1$ of 150 nH (Fig. 3-19), the recorded $V_{Pro\_ss}$ was –11.8 V at $P_t$ of 0.050 W, which was slightly more positive than the $V_{Pro\_rss}$. As the $P_t$ increased, the $V_{Pro\_ss}$ became more negative till the most negative $V_{Pro\_ss}$ was reached at –13.2 V when $P_t$ was 0.538 W. Then, the $V_{Pro\_ss}$ began to become less negative as $P_t$ was further increased. The $V_{Pro\_ss}$ was –11.2 V at $P_t$ of 2.208 W and was –10.6 V at $P_t$ of 2.607 W; both values were more positive than the $V_{Pro\_rss}$.

As shown in Fig. 3-20, the overall trend of the $V_{Pro\_ss}$ at $L_1$ of 330 nH is similar to the measured $V_{Pro\_ss}$ when $L_1$ is 150 nH. The $V_{Pro\_ss}$ was –11.9 V at the tested lowest $P_t$ – 0.019 W. The $V_{Pro\_ss}$ was gradually decreased as $P_t$ was increased, and the most negative $V_{Pro\_ss}$ was recorded at –13.7 V when $P_t$ was 0.273 W. As the $P_t$ was further increased, $V_{Pro\_ss}$ experienced a rapid increase and became more positive than the $V_{Pro\_rss}$. The $V_{Pro\_ss}$ was –9.8 V at $P_t$ of 0.781 W and was –7.0 V at $P_t$ of 1.093 W.

## 3.5 Discussion

At several tested $P_t$ levels for $L_1$ of both 150 nH and 330 nH, the $V_{Pro\_ss}$ are more negative than the $V_{Pro\_rss}$, which indicates that the electron density is increased between two RF electrodes with the applied RF voltage. For a more negative $V_{Pro\_ss}$, a larger thermal electron current is required to flow through the resistors that are in parallel with DC blocking capacitor $C$, and this larger thermal electron current can be only sourced from the electron trap with higher electron density. Therefore, the most negative $V_{Pro\_ss}$ implies the highest electron density among the tested $P_t$ levels. For $L_1$ of 150 nH, the most negative $V_{Pro\_ss}$ is achieved at $P_t$ of 0.538 W, which is 46% smaller than the estimated ideal RF power from the simplified circuit model. For $L_1$ of 330 nH, the most negative $V_{Pro\_ss}$ is achieved at $P_t$ of 0.273 W, which is 2x the estimated ideal RF power from the simplified circuit model. Although the most densified electron trap is not exactly established at the estimated ideal RF power levels, the developed circuit model of the E$^3$TM is more accurate in determining the ideal operating RF signal than the circuit model of the ETM, as the measured most negative steady state electrode potential of the ETM is acquired at a RF power that is 10x smaller than the estimated ideal RF power in Chapter 2. Additionally, the trends predicted by the model are followed by the experimental results at the two tested frequencies. A lower $\left|V_{RF}^{*}\right|$ is predicted by the model for a lower operating frequency, and the most negative $V_{Pro\_ss}$ is observed at a lower $P_{fwd}$ for the lower frequency. The improved match of the trends with the idealized model is expected because a more uniform electrical field is maintained between the RF electrodes by reducing the effects of non-idealities – such as the fringing field near perforations and charge accumulation on ceramic surfaces. This also implies that the full volume of the trap is more efficiently used, with electrons able to travel nearly the full electrode gap in the E$^3$TM.

The electron current equation of a probe with a collisionless sheath that was used to estimate the electron density $n_e$ for the ETM in the Chapter 2 is updated with the geometries and results of the E$^3$TM for estimating the electron density [Lie94]:

$$n_e \approx -9.8\times10^3 \cdot \frac{V_p}{A_e} \tag{3-10}$$

where $V_p$ is the measured $V_{Pro\_ss}$ (in volts) and the $A_e$ is the surface area of the probe between the RF electrodes (0.06 $\text{cm}^2$). The estimated highest electron density is $2.16 \times 10^6$ $\text{cm}^{-3}$ at $P_t$ of 0.538 W for $L_1$ of 150 nH, and $2.24 \times 10^6$ $\text{cm}^{-3}$ at $P_t$ of 0.273 W for $L_1$ of 330 nH; both are 10x higher than the electron density in the ETM when the most negative steady state electrode potential is achieved [Den17]. Thus, the $E^3$TM has higher electron trapping efficiency than the ETM. In addition, the estimated highest electron density is almost identical for $L_1$ at 150 nH and 330 nH, but the measured $P_t$ when the $E^3$TM is operated at $f_{0\_l}$ of 96.9 MHz is only half of the $P_t$ when the $E^3$TM is operated at $f_{0\_l}$ of 141.3 MHz. There are two reasons for such results. First, the impedance of $C_{L2}$ that represents the RF electron trap is inversely proportional to $f_{RF}$, which means that a smaller current is required to generate the same $|V_{RF}|$ at a lower $f_{RF}$. Second, the ideal RF voltage $\left|V_{RF}^*\right|$ is decreased as $f_{RF}$ decreases, which means that a similar RF electron trap can be realized at a lower $f_{RF}$ with a lower $|V_{RF}|$. Thus, the power consumption of the $E^3$TM is adjustable by changing the inductance of $L_1$, but there is a tradeoff to operate the RF electron trap at a lower $f_{RF}$ – the electrons are less energetic in the ideal trapping conditions. This may affect gas pumping because the full pump configuration is dependent on gas ionization, which requires sufficiently energetic electron-gas collisions.

The trend of $V_{Pro\_ss}$ is similar to the ETM at the lower and higher power ends [Den17]. The values of $V_{Pro\_ss}$ are close to the $V_{Pro\_rss}$ at the lowest tested $P_t$. The developed $|V_{RF}|$ at these $P_t$ levels are not strong enough to cycle the electrons between the RF electrodes, so the electron density is still dependent on the electron beam current. However, the values of $V_{Pro\_ss}$ are more positive than the $V_{Pro\_rss}$ at the highest tested $P_t$. At these $P_t$

levels, the calculated $|V_{RF}|$ are larger than the $\left|V_{RF}^{*}\right|$ that are associated with the tested $f_{RF}$. The RF electron trap is depleted by this RF voltage as electrons are accelerated and leave the trap or collide into the RF electrodes before the direction of the electric field changes. Note that the probe is in the center of the electron trap where the electrons have the highest kinetic energy when cycle between two RF electrodes. Thus, the electrons that collide with the probe at various incident angles may cause secondary electron emissions and make the $V_{Pro\_ss}$ more positive when the $P_t$ increases [Sei83]. The characteristic of a range of power levels that result in trapping is expected from the idealized analytical model and from numerical modeling of these types of devices [Mar17].

Although the $E^3$TM has a higher estimated electron density in the RF electron trap than the ETM, it requires 7-10x more RF power for the $E^3$TM to achieve it. Note that ideally, the RF electron trap behaves like a capacitor that does not consume power; all power is dissipated as heat from parasitic resistance. For future power improvement, contact resistance can be minimized by soldering or welding metal joints together rather than connecting them through mechanical contact as in the $E^3$TM. Another source of parasitic resistance potentially comes from the series inductor $L_1$ placed outside the chamber to lower the operating frequency of the $E^3$TM. It is possible to adjust the operating frequency of the $E^3$TM without using the series inductor solely by adjusting the gap between the sorption electrode and the bottom RF electrode of the $E^3$TM, as the capacitance between the bottom RF electrode and the sorption electrode dominates the total shunt capacitance $C_{L2}$ identified in the circuit model.

## 3.6 Conclusion

The $E^3$TM is improved in mechanical structure, electrical configuration, and testing setup to enhance the RF electron trapping efficiency when compared to the ETM [Den17]. The RF electrodes of the $E^3$TM are micromachined with a 10x finer perforation pattern than the ETM to increase the uniformity of the RF electric field between RF electrodes. All grounded metal parts of the $E^3$TM are electrically shorted together in the assembly to reduce the parasitics, compared to the grounded parts of the ETM, which are individually routed outside the chamber to perform grounding. The $E^3$TM presents a much simpler de-embedded impedance than the ETM in the characterized RF frequency range. The series resonant frequency of the $E^3$TM, as well as the operating RF frequency of the RF electron trap, is tunable with the external series inductor $L_1$. Based on the measured $V_{Pro\_ss}$, the highest estimated electron density is $2.24 \times 10^6$ $cm^{-3}$, which is 10x higher than the estimated electron density in the ETM. The $E^3$TM and the modified vacuum system can be used in the future work to investigate gas pumping for both reactive and inert gasses, because the RF electrodes are fabricated from titanium and a tantalum sorption electrode is integrated into the stack.

# CHAPTER 4:

# MINIATURIZED COLD CATHODE GAUGES

Capacitance Diagram Gauges (CDGs) are widely used in semiconductor manufacturing processes for vacuum monitoring. However, the normal operation and measurement accuracy of the CDGs are dependent on the integrity of their reference vacuum chambers. To improve the reliability and to enable the failure prediction of the CDGs, miniature cold cathode gauges (CCGs) are proposed for monitoring the reference vacuum of the CDGs from $10^{-3}$ Torr to $10^{-9}$ Torr. Different CCG designs with an internal volume of less than 1 $cm^3$ have been studied regarding their geometries to result in efficient electron trapping in Section 4.1 and Section 4.2. Section 4.3 describes the refined CCG designs and their manufacturability to be compatible with existing processes of CDGs, followed by a refined magnetron design for a standard vacuum feedthrough in Section 4.4 and conclusion in Section 4.5.

## 4.1 Penning Cell Gauge Designs

As shown in Fig. 4-1, a traditional Penning cell gauge includes a cylindrical anode, two planar cathodes, and a magnetic circuit [Gre13, Pen37]. A high DC voltage $V_A$ is applied between the anode and cathodes to form a radially-directed electric field inside the anode cylinder. The magnetic circuit consists of magnets and a magnetic return path and provides a magnetic field along the length of anode. Typically, the electric field and magnetic field are axially symmetric about the axis of the anode, as shown in Fig. 4-1. The crossed electric and magnetic fields cause electrons to spiral and be confined within the anode cylinder, promoting ionizing collisions with gas molecules rather than immediate termination at the anode. Tighter confinement, as necessary for miniature structures, requires stronger magnetic fields.

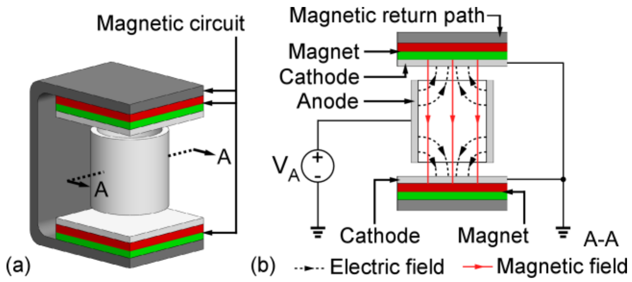

Figure 4-1: A traditional Penning cell CCG. The gauge consists of an anode cylinder, two planar cathodes, and a magnetic circuit that includes two permanent magnets and a magnetic return path. (a) 3D schematic. (b) A-A section view.

### 4.1.1 Analytical Approach

For investigation of the electron trajectory, COMSOL Multiphysics is used [COM17]. A three-dimensional model incorporating electrostatic field and magnetic field physics modules is developed for the proposed gauge designs. In the finite element analysis (FEA) model, the gauge is centered and enclosed in a large air block (12 x 12 x 12 $cm^3$), and material properties are assigned to different gauge parts and air accordingly to reflect their electrical and magnetic properties. N52 grade neodymium magnets are selected to produce the magnetic field here, with the decision criteria for this including cost, magnetic field strength, and commercial availability considerations. This grade of neodymium magnet has the highest output magnetic flux per unit volume, which aids in gauge miniaturization. Thus, modeling domains that represent the magnets are assigned a remanent magnetic flux density $\boldsymbol{B_r}$ of 1.45 T along their magnetization directions

[Neo17]. Soft-iron is selected to route the magnetic flux in the magnetic circuit because it can withstand high magnetic flux density without saturation. The non-linear magnetic B-H curve of soft-iron built into COMSOL (Fig. 4-2) is included in the model to estimate the magnetic field distribution. Titanium is selected for the anode and cathodes. This material is frequently used in Penning cell sputter ion pumps, has low outgassing rates, and may assist in pumping of the reference chamber (via gettering) to combat leaks. As this is a non-magnetic material, it has little reaction to the magnetic field, which desirably maintains uniformity of the magnetic field within the Penning cell.

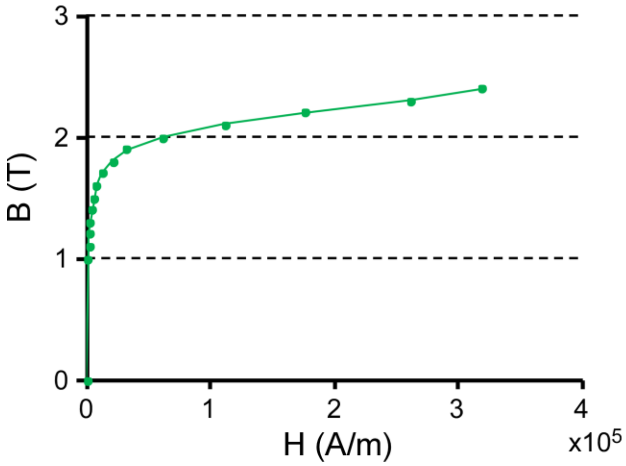

Figure 4-2: B-H curve of the soft-iron [Boz93].

In the electrostatics physics module, the anode surfaces are biased at $V_A$, and the cathode surfaces are grounded. This $V_A$ is varied from 100 V to 1000 V with a step size of 100 V to study the resulting electric field based on charge conservation equations [Ula15]:

$$\boldsymbol{E} = -\nabla V_A \tag{4-1}$$

$$\nabla \cdot (\varepsilon_0 \varepsilon_r \boldsymbol{E}) = \rho_v \tag{4-2}$$

where $\boldsymbol{E}$ is electric field, $\varepsilon_0$ is permittivity of vacuum (8.85 x $10^{-12}$ F/m), $\varepsilon_r$ is relative permittivity, and $\rho_v$ is space charge density (which is assumed to be zero for the purposes of the analyses presented here). In the physics module that is used for magnetic fields (in the absence of electrical current), the magnetic field distribution is analyzed with magnetic flux conservation [Ula15]:

$$\boldsymbol{B} = \mu_0\mu_r\boldsymbol{H}+\boldsymbol{B_r} \tag{4-3}$$

$$\boldsymbol{H} = -\nabla V_m \tag{4-4}$$

$$\nabla \cdot (\mu_0\mu_r\boldsymbol{H}) = 0 \tag{4-5}$$

where $\boldsymbol{B}$ is the magnetic flux density, $\boldsymbol{H}$ is magnetic field strength, $\boldsymbol{B_r}$ is remanent flux density, $V_m$ is magnetic scalar potential, $\mu_0$ is vacuum permeability (4π x $10^{-7}$ H/m), and $\mu_r$ is relative permeability. This FEA approach allows estimation of the electric and magnetic fields arising from the geometry under different applied voltages and magnetic circuits. The electric and magnetic fields determined from this simulation are then used in a particle tracking analysis, which consists of releasing an electron near a gauge cathode and using numerical integration of Lorentz forces to estimate the resulting electron trajectory [Hay11]:

$$m_e\boldsymbol{a} = \boldsymbol{F} \tag{4-6}$$

$$\boldsymbol{F} = q(\boldsymbol{E} + \boldsymbol{v}\times\boldsymbol{B}) \tag{4-7}$$

where $m_e$ is mass of the electron (9.1095 x $10^{-31}$ kg), $\boldsymbol{a}$ is acceleration of the electron, $\boldsymbol{F}$ is the Lorentz force acting upon the electron, $q$ is the elementary charge carried by a single electron (-1.602 x $10^{-19}$ C), and $\boldsymbol{v}$ is the velocity of the electron. The initial velocity of the electron is perpendicular to the cathode surface (toward the anode) and set to be 1.229 x $10^{6}$ m/s. The equivalent kinetic energy for an electron at this velocity is equal to

4.3 eV, which is the work function for titanium, the cathode material [Hay16]. This is the typical velocity associated with an electron emitted from the titanium surface. The trajectory is calculated for up to $10^5$ integration steps, which is sufficient to track particles in typical geometries for hundreds of loops. If the electron travels for all steps without colliding into the boundary, the trajectory of the electron can be considered “infinitely” spiraling and likely to lead to eventual gas collision. In this case, the electric and magnetic fields determined from the simulations are considered appropriate for achieving gas ionization at high or ultra-high vacuum. In other words, an infinitely spiraling electron as determined by this FEA approach indicates a suitable gauge design.

### 4.1.2 Parametric Study of Critical Magnetic Field

In order to estimate the magnetic field required for Penning cell gauges to trap the electron at the desired geometries, a simplified Penning cell model, based on the defined FEA approach in section 4.1.1, is first applied. This approach analyzes the electron trajectory under different electric and magnetic fields, while varying selected geometrical parameters (Fig. 4-3). The simplified Penning cell only consists of a cylindrical anode and two flat cathodes. The cathodes are aligned in parallel at a fixed gap of 6 mm, while the anode is placed between and in the center of the two cathodes. Two geometrical variables are investigated here – anode length $L_a$, and anode inner diameter $D_a$. In the electrostatic model, the cathodes are grounded, and the anode biasing voltage $V_A$ is specified as either 400 V or 1000 V. A magnetic flux density $B$ is applied uniformly along the axial direction of the anode from 0.025 T to 0.200 T in the model. This is a simplified representation of the magnetic flux, which will likely be somewhat non-uniform in a practical Penning cell gauge.

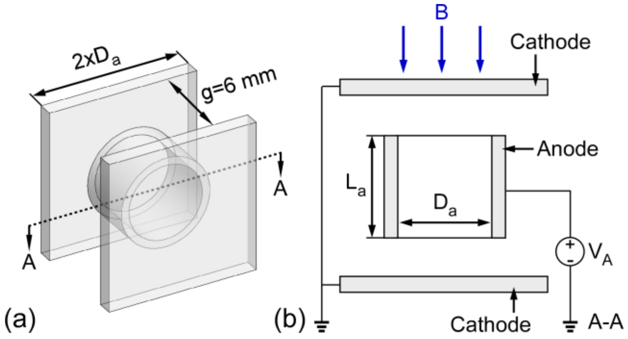

Figure 4-3: Simplified Penning cell model with four variables to investigate electron spiraling at desired geometries – anode length $L_a$, anode inner diameter $D_a$, anode biasing voltage $V_A$, and magnetic flux density $B$. (a) 3D schematic. (b) A-A section view.

The initial position of the electron is 1 µm away from one cathode plate and at 75% of the anode radius along the radial direction of the anode. The initial velocity of the electron is $1.229 \times 10^6$ m/s, as stated previously. Simulations show that the electron spirals infinitely when the magnetic flux density exceeds the critical magnetic flux density $B_c$ (Fig. 4-4 (a)). At a lower magnetic flux density, the electron collides into the cathodes or the anode after only a few loops (Fig. 4-4 (b)). From the perspective of gauge performance, $B_c$ indicates the lowest magnetic field to enable infinitely electron spiraling for the assessed parameters. The $B_c$ ranges from 0.06 to 0.12 T when $V_A$ is 400 V and is the largest with two anode types: long with a narrow diameter, and short with a wide diameter, as shown in Fig. 4-5 (a). The $B_c$ has a similar range from the simulation results when $V_A$ is 1000 V, but the $B_c$ increases when the anode length $L_a$ increases in the simulated parameter space, as shown in Fig. 4-5 (b). From the summarized simulation results in Table 4-1, the $B_c$ is typically observed to be inversely proportional to $V_A$ with each specific model geometry.

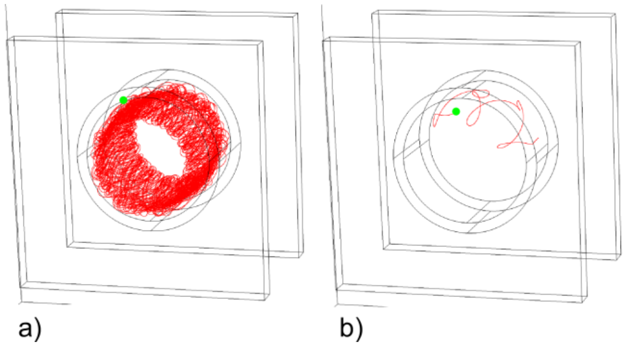

Figure 4-4: The electron trajectories determined from the simplified Penning cell model. Red trace indicates the integrated electron trajectory, and green dot represents the electron position in the end of simulation. (a) Electron spirals infinitely ($L_a$ = 4 mm, $D_a$ = 6 mm, $V_A$ = 1000 V, $B$ = 0.10 T). (b) Electron collides into cathode ($L_a$ = 4 mm, $D_a$ = 6 mm, $V_A$ = 1000 V, $B$ = 0.09 T).

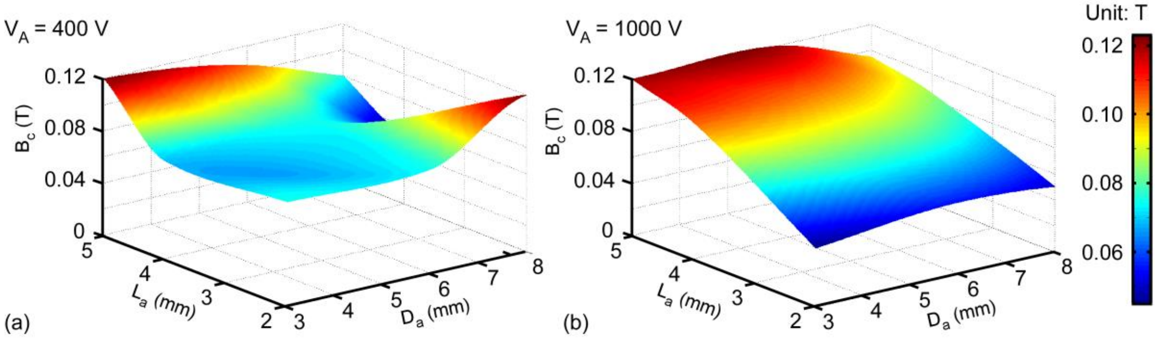

Figure 4-5: The critical magnetic flux density $B_c$ determined from the simulation results for various geometries at $V_A$ of (a) 400 V and (b) 1000 V.

Table 4-1: The critical magnetic flux density $B_c$ determined from simulation model for various geometries and voltages.

| Anode length $L_a$ (mm) | Anode diameter $D_a$ (mm) | Anode voltage $V_A$ (V) | Critical magnetic flux density $B_c$ (T) |
|---|---|---|---|
| 2 | 3 | 400 | 0.080 |
| 2 | 6 | 400 | 0.080 |
| 2 | 8 | 400 | / |
| 4 | 3 | 400 | 0.075 |
| 4 | 6 | 400 | 0.080 |
| 4 | 8 | 400 | 0.055 |
| 5 | 3 | 400 | 0.120 |
| 5 | 6 | 400 | 0.105 |
| 5 | 8 | 400 | 0.080 |
| 2 | 3 | 1000 | 0.045 |
| 2 | 6 | 1000 | 0.055 |
| 2 | 8 | 1000 | 0.050 |
| 4 | 3 | 1000 | 0.105 |
| 4 | 6 | 1000 | 0.100 |
| 4 | 8 | 1000 | 0.085 |
| 5 | 3 | 1000 | / |
| 5 | 6 | 1000 | / |
| 5 | 8 | 1000 | 0.095 |

/ - Indicates that no spiraling was found over the simulated applied *B* flux densities

### 4.1.3 Circular Designs

The Penning cell designs are classified into two different groups, circular and non-circular, based on the shape of the cases; because of the shapes of the designs affect the gauge integration to the CDG. Three circular Penning cell designs are investigated with the developed FEA approach in this section. The curved cathode design (Design P.C) is the only design that has cathodes that are part of the cylindrical case. The integrated magnetic circuit designs (Design P.I.1 and Design P.I.2) integrate the case, the magnetic return path, and the cathodes. The anode array design (Design P.A) consists of an array of anode cylinders within one magnetic flux path.

### 4.1.3.1 Curved Cathode Design (Design P.C)

The curved cathode design (Design P.C) is the simplest design among all the proposed designs, as shown in Fig. 4-6. In Design P.C, the cathodes on both sides of the anode cylinder are part of the case cylinder (8.8 mm inner diameter), which is different than traditional Penning cells that have flat cathodes. The anode is located inside the case with an inner diameter of 5.0 mm and a length of 4.0 mm. Thus, the spacing between the anode and cathodes reduces from the center to the edge of the anode as shown in Fig. 4-6 (b). A feedthrough provides electrical access to the anode. External to the cathode, a magnetic circuit includes two circular magnets (K&J magnetics, D52-N52, 5/16" diameter, 1/16" thickness, magnetization direction: axial) and a U-shaped magnetic return path. The magnets share the same center axis as the anode, and the opening of the anode is fully covered by these magnets. The overall volume of the gauge is 0.73 $cm^3$ without including the magnetic circuit. A glass seal exists between the case and feedthrough to provide electrical isolation and hold vacuum. Based on the analytical approach described in section 4.1.1, the geometry of Design P.C is analyzed with a simulation model, P.C.Sim. For simplicity, glass is not represented in P.C.Sim because it does not affect the electric and magnetic fields inside the anode.

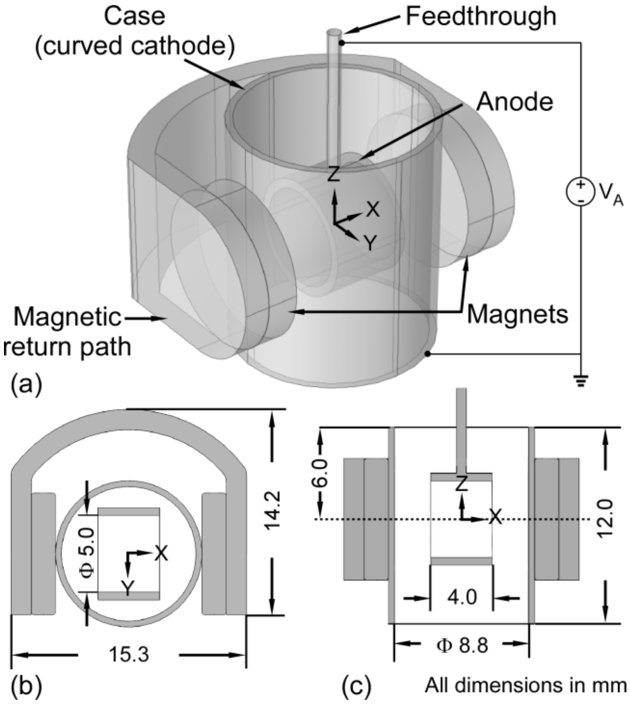

Figure 4-6: FEA model of Design P.C – P.C.Sim. Anode is biased at $V_A$, and cathode is grounded. (a) 3D schematic. (b) X-Y section view. (c) X-Z section view.

The simulation results (Fig. 4-7 (a) and (b)) show that the electric field lines are perpendicularly terminated into the anode and cathode surfaces, and present plane symmetry in X-Y, X-Z, and Y-Z planes. In the magnetic field obtained from the simulation (Fig. 4-7 (c) and (d)), the flux lines are axially symmetric along the length of the anode (X axis), and diverge radially (e.g. Y axis and Z axis) within the anode. The magnetic flux density of this non-uniform magnetic field $B$, which is 0.18 T at the center of the anode at its maximum value, is comparable to the critical magnetic flux density $B_c$ that was identified in section 4.1.2. However, there is a relatively large tangential magnetic field component $B_t$ at the cathode surfaces because of the cathode curvature. The ratio of $B_t$ to $B$ ranges from 0 to 0.98. This does have a perceivable impact on performance and is discussed in the next paragraph.

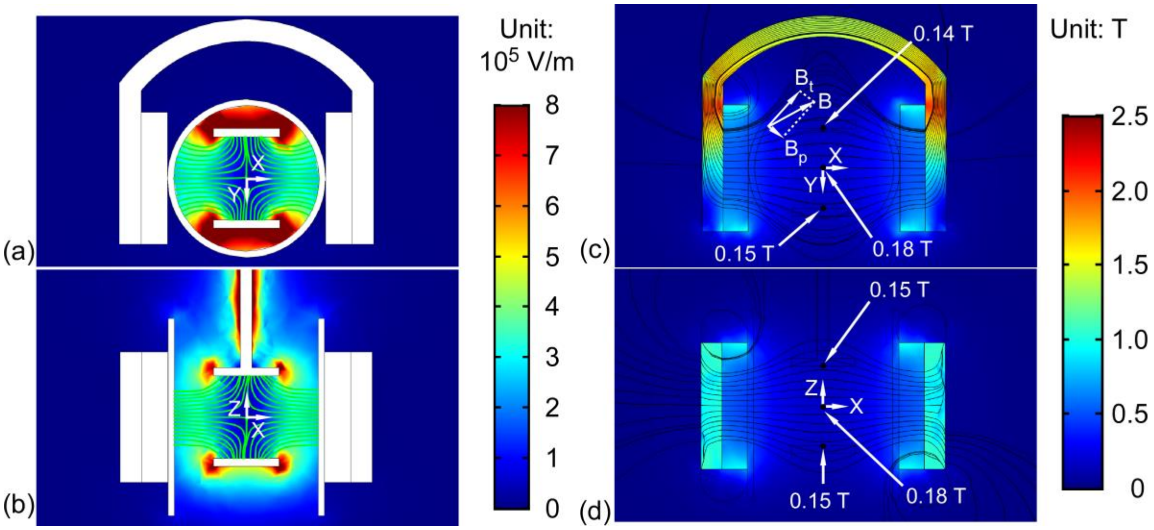

Figure 4-7: The simulation results of P.C.Sim. The electric fields at (a) X-Y section view and (b) X-Z section view (anode voltage $V_A$ of 1000 V). The magnetic flux density at (c) X-Y section view and (d) X-Z section view.

The electron trajectory is analyzed with the electric and magnetic fields that are determined from P.C.Sim. In the particle tracking model of this design, electrons are assumed to be released from several radial positions within the anode radius while still 1 μm away from cathode surfaces. The initial velocity of each electron is 1.229 x $10^6$ m/s in a direction normal to the cathode surface at the point of origin. Once an electron is released, it immediately experiences an electrostatic force from the electric field, as well as a sideways force from the tangential magnetic field $B_t$. Thus, the electron spiraling starts immediately upon release, because there is an angle between the resultant force and the initial velocity. This early spiraling dramatically increases the possibility for an electron to collide into anode surfaces as it moves towards the anode. For $V_A$ from 200 V to 1000 V with an interval of 100 V, all electrons terminate at the anode surface in the first a few numerical integration steps (e.g. Fig. 4-8). In comparison, the electric field lines in the traditional Penning cell gauge are mostly parallel to magnetic field lines near the flat cathodes (Fig. 4-1 (b)). Therefore, the electron moves directly into the anode cylinder after release, and the spiraling starts inside the anode as electric field lines are radially-directed towards the anode in that area. Although the curved cathode design is simple in architecture, the electric and magnetic fields are not suitable to trap electrons infinitely.

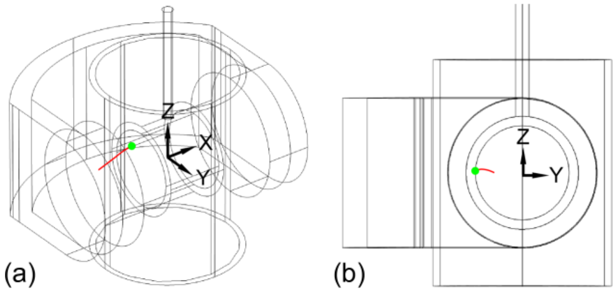

Figure 4-8: The electron trajectory at anode voltage $V_A$ of 1000 V in P.C.Sim from the simulation result. Electron is released at (X, Y, Z) = (–4.199 mm, –1.0 mm, 0 mm). The red line is the integrated electron trajectory, and the green dot is the electron end position (anode). (a) 3D schematic. (b) Y-Z section view.

#### 4.1.3.2 Integrated Magnetic Circuit Designs (Design P.I.1, Design P.I.2)

In the integrated magnetic circuit designs (Design P.I.1 and Design P.I.2), the case, the magnetic return path, and the cathodes are monolithically formed as shown in Fig. 4-9. The overall shape of the Design P.I.1 is defined by a circular case with a diameter of 11.1 mm and 14.8 mm in height. The bottom side of the case forms a cubic opening. Two 8.0 x 8.0 mm$^2$ sidewalls of this opening – acting as gauge cathodes – are separated by a gap of 6.0 mm. The cylindrical anode is 5.0 mm in diameter and 4.0 mm in length, and is centered within the gap with its axis perpendicular to the flat cathodes. The electrical feedthrough for the anode passes through a central perforation of the case. As for the magnetic circuit, two slots on the top side of the case embed two commercial magnets (K&J magnetics, B631-N52, 3/8" x 3/16" x 1/16", magnetization direction: thru thickness), whereas the case itself is made from soft-iron to route the magnetic flux. The slots for the magnets are parallel to the cathodes below them; this is intended to maximize the axially-directed magnetic flux routed through the anode. The bottom perimeter of the gauge is sealed to the vacuum reference chamber of the CDG, while glass seals the feedthrough to the case; both are not shown in Fig. 4-9. Although the gauge volume is 1.43 cm$^3$, it can be partially embedded into the CDG structure to still meet the volume constraint, as external magnets are above the sensing section where the electrodes are located. The geometry of Design P.I.1 is investigated with the simulation model P.I.1.Sim that is based on the analytical approach described in section 4.1.1.

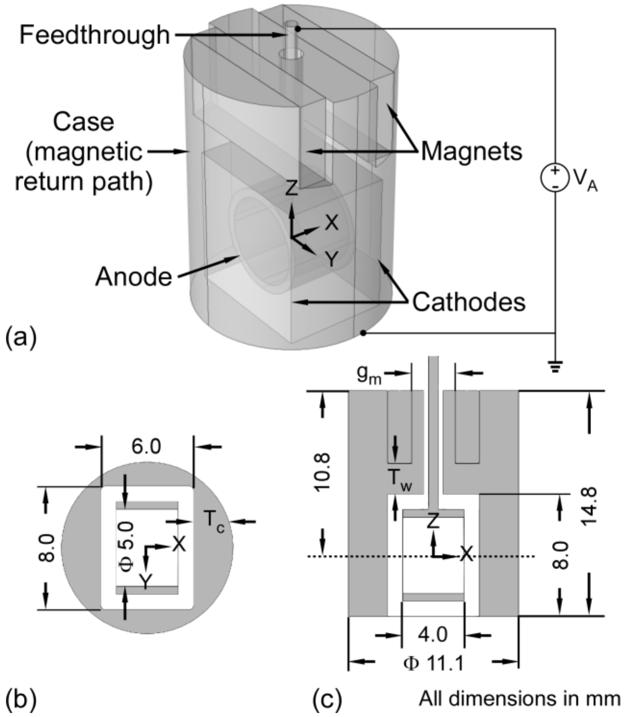

Figure 4-9: FEA model of Design P.I.1 – P.I.1.Sim. Anode is biased at $V_A$, and cathodes are grounded. (a) 3D schematic. (b) X-Y section view. (c) X-Z section view.

The electric field from the simulation results in P.I.1.Sim has axial symmetry about the X axis within the anode (Fig. 4-10 (a) and (b)). However, the magnetic field exhibits a very non-uniform distribution within the anode. In the X-Y plane (Fig. 4-10 (c)), the magnetic field decreases along the radial direction of anode, because the thickness of the magnetic return path in the X direction $T_c$ is smaller as the edge of the circular case is approached in the Y direction. In the X-Z plane (Fig. 4-10 (d)), the magnetic field gradually decreases as it moves away from the magnets along the negative Z direction. The magnetic return path is observed to saturate near the magnets, and insufficiently route the magnetic flux to the anode region. The magnetic flux density that is determined from P.I.1.Sim is 0.0029 T at the center of anode, which is 20x smaller than the critical magnetic flux density $B_c$ required for a similar Penning cell geometry to produce infinite electron spiraling below $V_A$ of 1000 V.

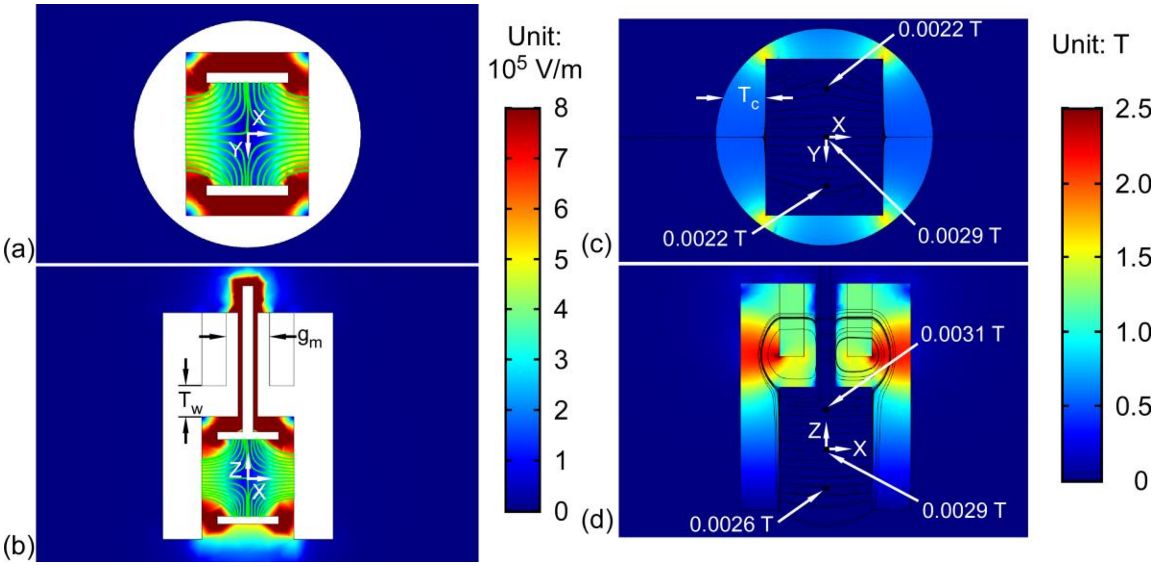

Figure 4-10: The simulation results of P.I.1.Sim. The electric fields at (a) X-Y section view and (b) X-Z section view (anode voltage $V_A$ of 1000 V). The magnetic flux density at (c) X-Y section view and (d) X-Z section view.

In order to increase the magnetic flux density in the sensing region of Design P.I.1, several improvements of the magnetic circuit have been considered in Design P.I.2. The gap between the two magnets $g_m$ is decreased from 2.8 mm to 1.8 mm. This expands $T_c$ near the magnet locations for better magnetic conduction. In addition, the wall thickness between the magnets and the anode $T_w$ is trimmed from 2.0 mm down to 0.4 mm to reduce the magnetic conductivity of this flux leakage path. The geometry of Design P.I.2 is analyzed with the simulation model P.I.2.Sim. Although the magnetic flux density after the improvements has smaller saturated volume in the magnetic return path and is 10x higher in magnitude within the anode from the simulation results of P.I.2.Sim, the magnetic field is still non-uniformly distributed (Fig. 4-11). This is because of the inherent limitation of the circular magnetic return path with flat magnets: more volume of the magnetic return path experiences a saturation as $T_c$ decreases as shown in the plotted 2D magnetic field distributions (Fig. 4-12). This problem might be solvable by increasing the diameter of the circular magnetic return path, or by changing the cross-section of the magnetic return path so that the thickness is not reduced near the perimeter along the Y axis. However, these changes are likely to violate the dimensional or manufacturability constraints of the gauge.

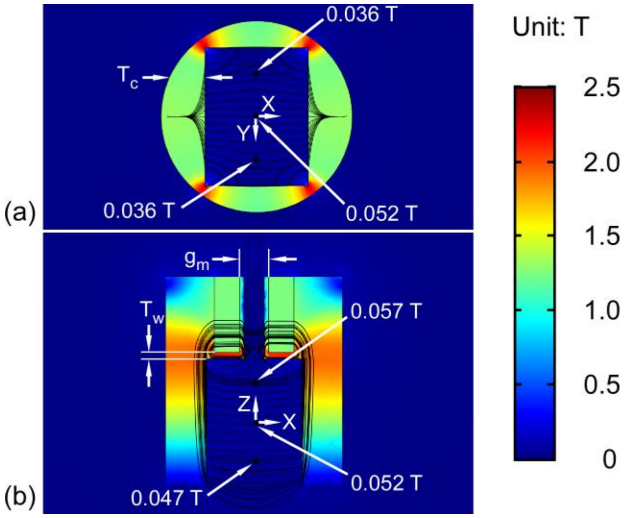

Figure 4-11: The magnetic flux density from the simulation results in P.I.2.Sim with smaller $g_m$ (2.8 mm to 1.8 mm) and $T_w$ (2.0 mm to 0.4 mm) at (a) X-Y section view and (b) X-Z section view.

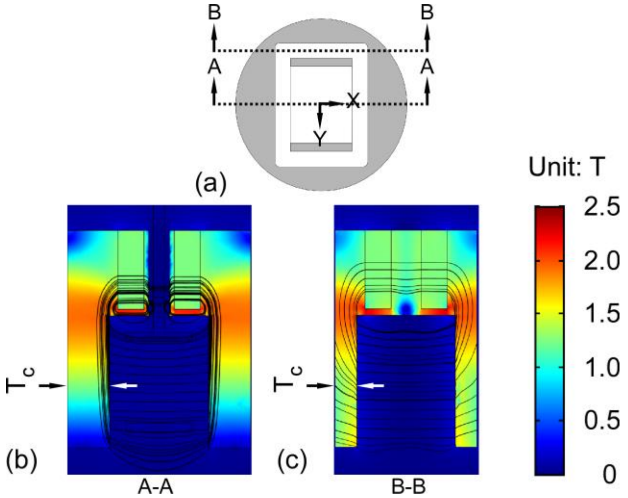

Figure 4-12: Magnetic saturation in the magnetic return path at different $T_c$. (a) X-Y section view of gauge to define locations of two section views. The magnetic flux density from the simulation results in P.I.2.Sim at (b) A-A section view and (b) B-B section view.

For Design P.I.2, the electron trajectory is investigated under electric and magnetic fields that result from P.I.2.Sim. An electron is released 1 μm away from a cathode surface in the X direction and at 60% of the anode inner radius in the radial direction. The initial velocity of the electron is $1.229 \times 10^6$ m/s in the X direction, as stated previously. Electrons collide with the anode quickly after release for the simulated values of $V_A$ from 200 V to 1000 V with a step of 100 V. As suggested by an electron trace at $V_A$ of 1000 V (Fig. 4-13), the electron is mainly driven by electrostatic force from the electric field as the crossed magnetic field is too weak to result in electron spiraling. For designs P.I.1 and P.I.2, although the integration of the magnetic return path, cathodes, and case is appealing for gauge miniaturization, the magnetic flux is insufficient for trapping electrons.

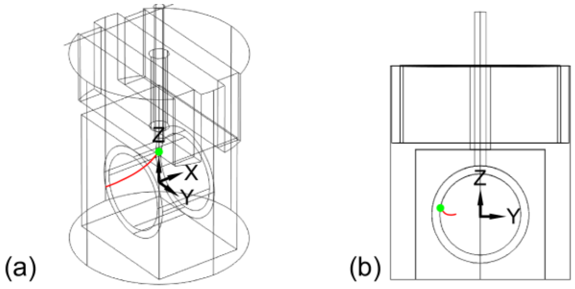

Figure 4-13: Simulation result of electron trajectory at anode voltage $V_A$ of 1000 V in P.I.2.Sim. Electron is released at (X, Y, Z) = (–2.999 mm, –1.5 mm, 0 mm). The red line is the integrated electron trajectory, and the green dot is the electron end position (anode). (a) 3D schematic. (b) Y-Z section view.

#### 4.1.3.3 Anode Array Design (Design P.A)

The anode array design (Design P.A) consists of a case cylinder, a ring magnet, and an anode disc that contains an array of four anodes (Fig. 4-14). The case cylinder is 10.0 mm in outer diameter and 5.4 mm in height, and defines the outline of gauge. A ring-shaped recess is located on top of the case to fit a ring magnet (K&J magnetics, D61-N52, 3/8" diameter, 1/16" thickness) with axial magnetization direction. Another cylindrical recess with a height of 3.0 mm and diameter of 8.0 mm is on the bottom of the case, and contains the anode disc (6.8 mm in diameter, and 1.0 mm in height). Four anode perforations (2.0 mm in diameter) are arranged symmetrically on this anode disc. Thus, each of the four anode surfaces is affectively a cylinder 2 mm in diameter and 1 mm in height. Additionally, the axes of the anodes are in parallel with the case axis, rather than perpendicular to the case axis as in the previous two designs. A feedthrough pin is located in the center of anode disc for electrical access. A glass seal is assumed to exist between the feedthrough and the case that is not included in the model for simplicity. The case wall below the magnet acts as a flat cathode on the top side. The bottom cathode is a separate piece that has the same outer diameter as the case. The bottom cathode is perforated to permit gas flow between the sensing region and the vacuum reference chamber. The gauge is intended to be sealed to the vacuum reference chamber of the CDG along its bottom perimeter. There are several changes in this design as compared to the traditional Penning cell vacuum gauge. First, no magnetic return path is utilized to route the magnetic flux, and the flux is diverged freely outside the ring magnet to simplify the magnetic circuit. Then, the anodes are perforated in an array to allow feedthrough to connect through the center of anode disc, rather than from the side. This saves gauge space, as larger radial spacing between the anode disc and case is required to fit in a side feedthrough. The geometry of Design P.A is analyzed with the simulation model P.A.Sim that is based on the analytical approach described in section 4.1.1.

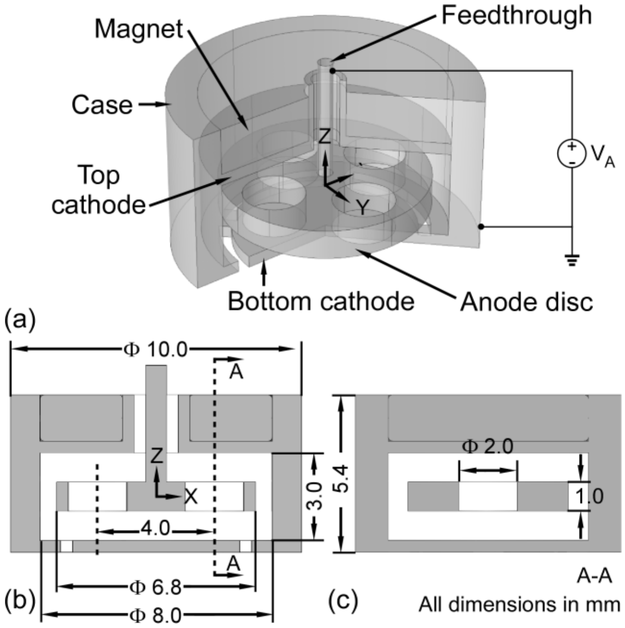

Figure 4-14: FEA model of Design P.A – P.A.Sim. The anode disc contains four perforations; the sidewalls of these perforations serve as arrayed anodes. (a) Cutaway view of 3D schematic. (b) X-Z section view. (c) A-A section view.

The simulations show that the electric field (Fig. 4-15 (a) and (b)) is axisymmetric within each anode perforation. In contrast, the magnetic field presents an expected asymmetrical distribution within the anode disc perforations (Fig. 4-15 (c) and (d)). In the anode disc perforations, the magnetic flux density ranges from 0.12 T to 0.19 T, which is close to the previously estimated critical magnetic flux density $B_c$ that ranges from 0.06 T to 0.12 T to have the potential for infinite electron spiraling. However, the non-uniformity of the magnetic flux density may alter the electron trapping capability of this approach.

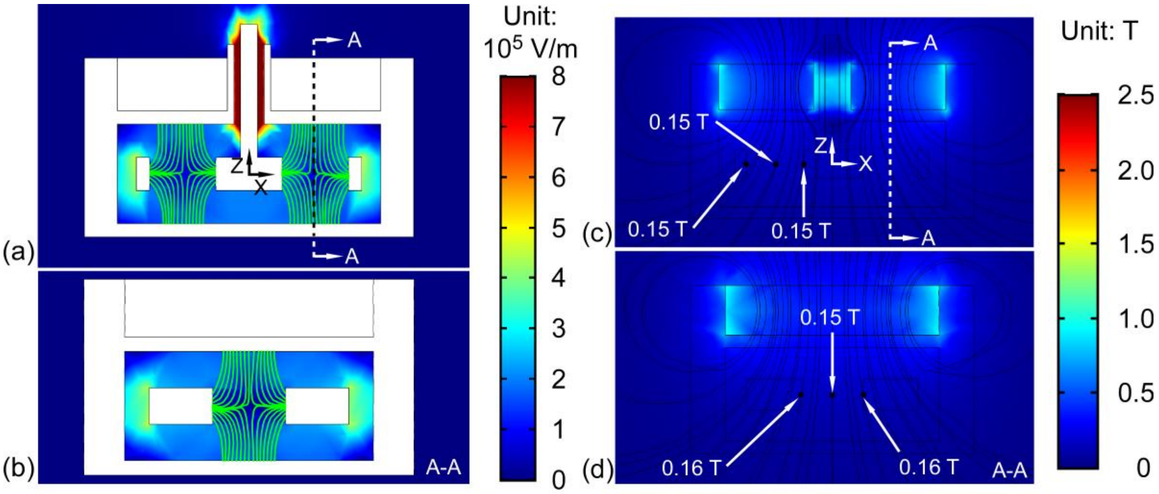

Figure 4-15: The simulation results of P.A.Sim. The electric field at (a) X-Z section view and (b) A-A section view (anode voltage $V_A$ of 200 V). The magnetic flux density at (c) X-Z section view and (d) A-A section view.

To investigate the impact of the asymmetrically distributed magnetic field on the electron trajectories, an electron is released from 8 different positions (labeled dots in Fig. 4-16). All these initial positions are 1 μm away from cathode surfaces and 60% of anode radius along the radial direction of anode. Again, the initial velocity of the electron is $1.229 \times 10^6$ m/s, normal to the cathode surface. The simulation results show that at an anode voltage $V_A$ from 200 V to 1000 V, only electrons being released from top right or bottom left (A and G in Fig. 4-16) can infinitely spiral; other electrons run into the anode directly. The trajectory profiles of infinitely spiraling electrons approximate the spindle shape of the magnetic field in anode perforation as shown in Fig. 4-17. Although the asymmetrical magnetic field and anode array is innovative, the electron can only spiral infinitely under certain initial conditions, which makes this design a risky approach.

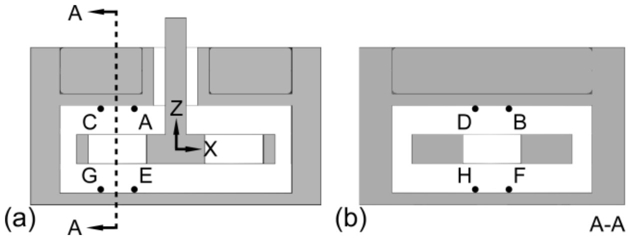

Figure 4-16: Electron releasing positions in electron trajectory simulations of Design P.A (red dots). These positions are located at 1 µm away from cathode surfaces and 60% of anode radius along radial direction of anode. (a) X-Z section view. (b) A-A section view.

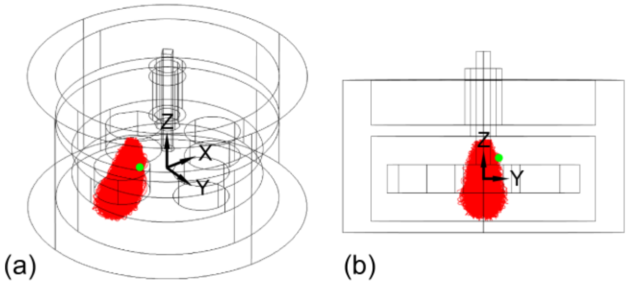

Figure 4-17: The electron trajectory at anode voltage $V_A$ of 200 V in P.A.Sim from the simulation result. Electron is released at (X, Y, Z) = (-1.4 mm, 0 mm, 1.499 mm). The red line is the integrated electron trajectory, and the green dot is the electron end position (inside the anode cylinder, without terminating into the anode). (a) 3D schematic. (b) Y-Z section view.

### 4.1.4 Non-Circular Designs

Two non-circular Penning cell designs are analyzed with the developed analytical approach. The flat cathodes design (Design P.F) has two flattened case surfaces to serve as cathodes. The embedded magnets design (Design P.E) encloses the magnets and the magnetic return path into the sensor case.

#### 4.1.4.1 Flat Cathodes Design (Design P.F)

The flat cathodes design (Design P.F) (Fig. 4-18) is similar to the curved cathode design (Design P.C) in section 4.1.3.1. One major difference is the shape of the gauge case – the interior of the cylindrical case (Design P.F) has two parallel and opposing flat surfaces that serve as the cathodes that are 6.4 x 12.0 $mm^2$ and spaced 6 mm apart. The active volume of the gauge is reduced to 0.58 $cm^3$ as opposed to 0.73 $cm^3$ in Design P.C. The magnetic circuit still consists of the same magnets and similar magnetic return path as Design P.C. However, the spacing between the two magnets is smaller, as both magnets are located outside the flat cathodes. The anode is still 5.0 mm in diameter and 4.0 mm in length, and is centered between the two parallel cathodes. The axes of the anode and magnets are collinear to provide the most favorable magnetic field inside the anode. The feedthrough for the anode is assumed to be sealed with glass that is excluded from the simulation model for Design P.F, P.F.Sim. This design can provide electric and magnetic fields that are similar to those in the traditional Penning cell gauge for better electron spiraling performance.

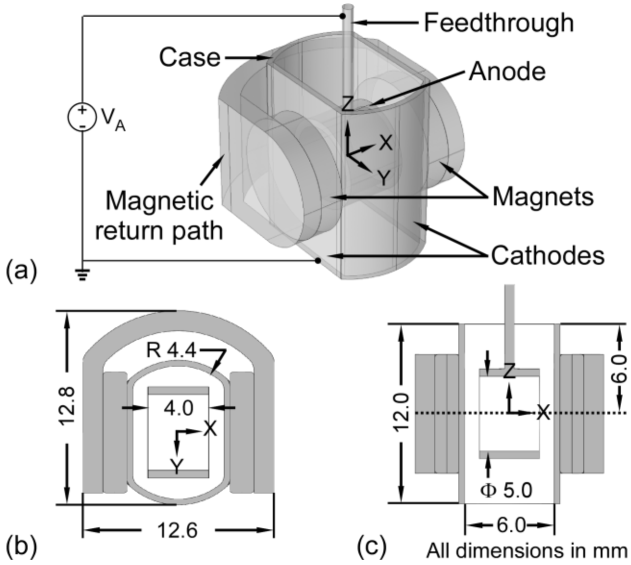

Figure 4-18: FEA model of Design P.F – P.F.Sim. Anode is biased at $V_A$, and cathodes are grounded. (a) 3D schematic. (b) X-Y section view. (c) X-Z section view.

The electric and magnetic fields that are determined from an analysis of P.F.Sim are axisymmetric about the anode axis (Fig. 4-19). The magnetic flux density is almost doubled compared to the curved cathode design (Design P.C) as shown in Fig. 4-19 (c) and (d). This flux density is 0.3 T in the center of the anode, which is large enough to enable infinite electron spiraling as suggested by the previously estimated critical magnetic flux density $B_c$ that ranges from 0.06 T to 0.12 T for geometries of this approximate size. In the electron trajectory simulation, an electron is released 1 µm away from the cathode surface at 60% of the anode radius along the radial direction of the anode. Simulations of electron trajectory (Fig. 4-20) show that the infinite electron spiraling exists at anode voltage $V_A$ from 600 V to 1000 V, and the trajectory profile is perfectly axisymmetric about the anode axis, similar to the profile from the simplified Penning cell model in section 4.1.2.

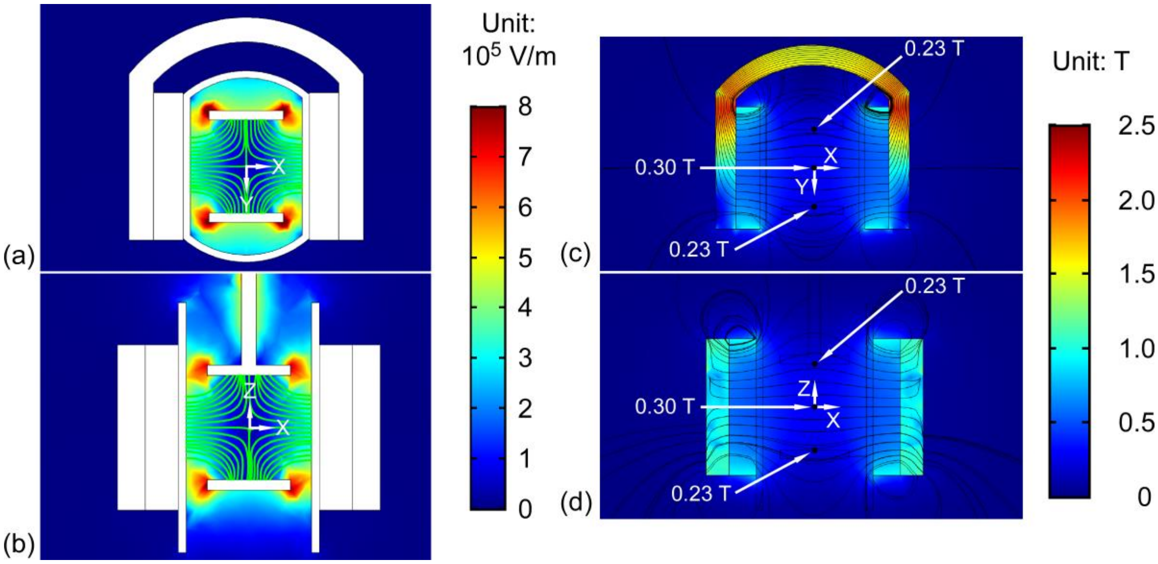

Figure 4-19: The simulation results of P.F.Sim. The electric field at (a) X-Y section view and (b) X-Z section view (anode voltage $V_A$ of 600 V). The magnetic flux density at (c) X-Y section view and (d) X-Z section view.

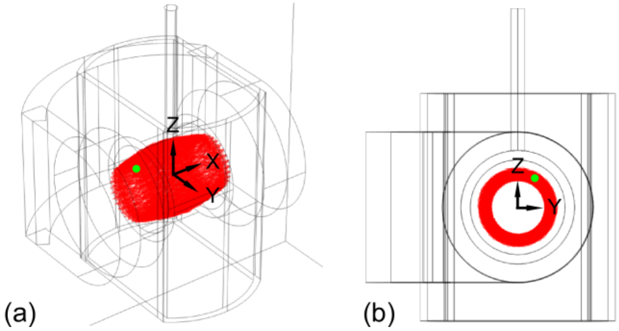

Figure 4-20: The electron trajectory at anode voltage $V_A$ of 600 V in P.F.Sim from the simulation result. Electron is released at (X, Y, Z) = (–2.999 mm, –1.5 mm, 0 mm). The red line is the integrated electron trajectory, and the green dot is the electron end position (inside the anode cylinder, without terminating into the anode). (a) 3D schematic. (b) Y-Z section view.

### 4.1.4.2 Embedded Magnets Design (Design P.E)

In the embedded magnets design (Design P.E) (Fig. 4-21), the overall dimension of the gauge is defined by the case, which is 13.8 mm in length, 7.3 mm in width, and 7.4 mm in height. Three square recesses hold the anode and magnets. This design is similar to the integrated magnetic circuit design (Design P.I), which encloses the magnetic circuit into the case. The center recess opens from the bottom of the case, and two flat surfaces (6.5 x 7.0 $mm^2$) act as parallel cathodes with a spacing of 6.0 mm. The anode cylinder (5.0 mm in diameter and 4.0 mm in height) is aligned along the X axis within the center recess, and centered between the two cathodes. The anode feedthrough is assumed to be glass sealed; the glass is not included in the simulation model P.E.Sim for Design P.E. The other two recesses open from the top of case, and are not intended to be held at vacuum. Two square magnets (K&J magnetics, B441-N52, 1/4" x 1/4" x 1/16", magnetization direction: thru thickness) and a U-shaped magnetic return path are enclosed within these two recesses to route magnetic flux through the anode. As the magnets are located on each side of the anode, rather than on the top of the anode as in the integrated magnetic circuit designs (Design P.I.1 and Design P.I.2), the gauge profile is much reduced compared to Design P.I.1 and Design P.I.2. This allows the entire gauge to be embedded within the case of the CDG, rather than extend outside the CDG as the other Penning cell designs described previously.

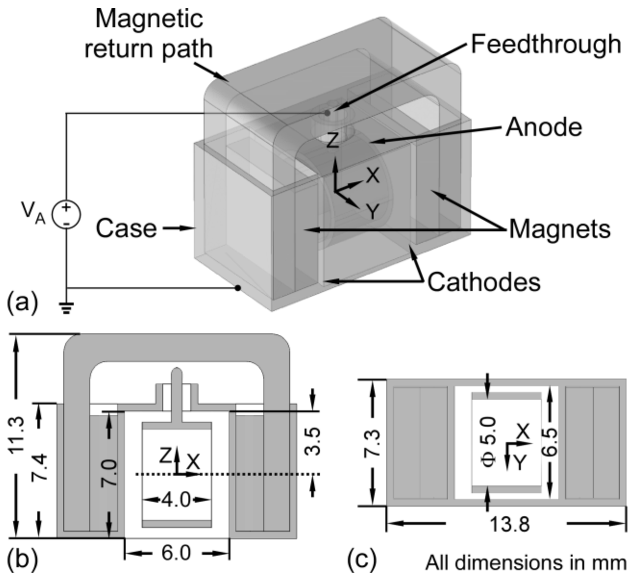

Figure 4-21: FEA model of Design P.E – P.E.Sim. Anode is biased at $V_A$, and cathodes are grounded. (a) 3D schematic. (b) X-Z section view. (c) X-Y section view.

The simulations show that the electric and magnetic fields (Fig. 4-22) present axial symmetry about the anode axis as in the traditional Penning cell gauge. The magnetic field strength is 5x higher than in Design P.I.2, as a consequence of the position of the magnets. To evaluate the electron spiraling under the electric and magnetic fields determined from the P.E.Sim analysis, the electron is released 1 µm away from cathode surfaces and 60% of anode radius along the radial direction of the anode. Again, the initial velocity of the electron is 1.229 x $10^6$ m/s, normal to the cathode surface. The integrated electron trajectory indicates the electron can infinitely spiral at anode voltage $V_A$ from 600 V to 1000 V (Fig. 4-23).

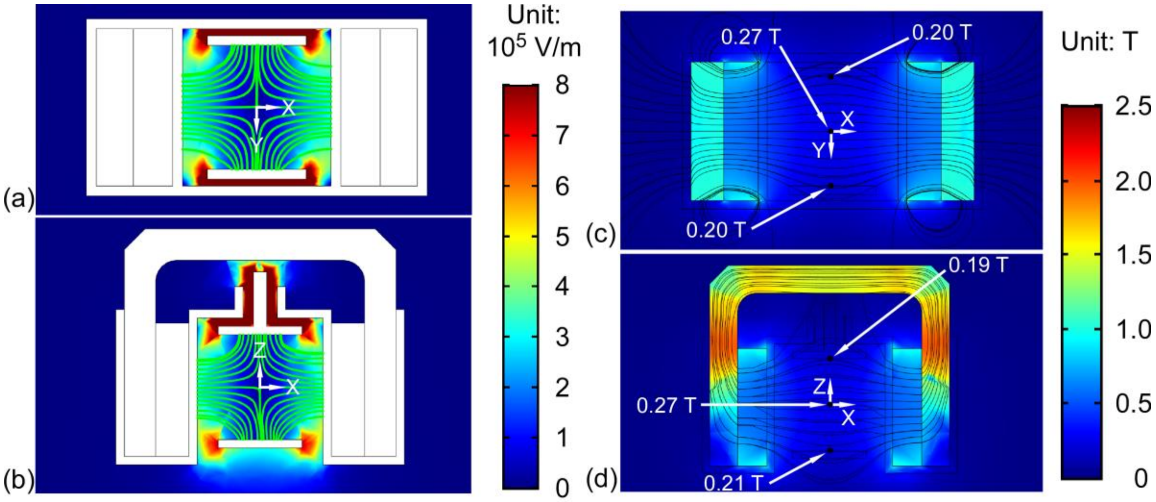

Figure 4-22: The simulation results of P.E.Sim. The electric field at (a) X-Y section view and (b) X-Z section view (anode voltage $V_A$ of 600 V). The magnetic flux density at (c) X-Y section view and (d) X-Z section view.

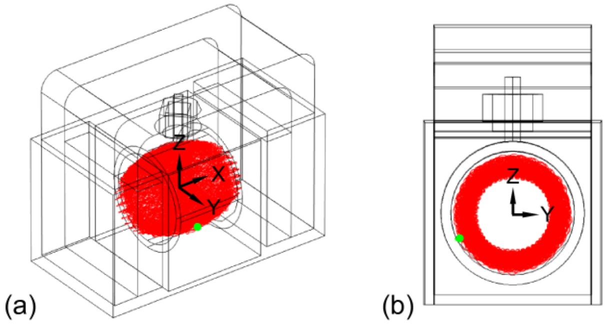

Figure 4-23: The electron trajectory at anode voltage $V_A$ of 600 V in P.E.Sim from the simulation result. Electron is released at (X, Y, Z) = (–3.0 mm+1 µm, –1.5 mm, 0 mm). The red line is the integrated electron trajectory, and the green dot is the electron end position (still within the anode cylinder, and not terminating into the anode). (a) 3D schematic. (b) Y-Z section view.

## 4.2 Magnetron Gauge Design (Design M.O)

The magnetron gauge is another type of CCG, as shown in Fig. 4-24 [Red59]. Similar to the Penning cell gauge, the electric fields are primarily radially directed between the cathode post and the anode when the cathode is grounded and the anode is biased at the voltage $V_A$. The magnetic field provided by the magnet is directed along the axis of the cylindrical anode. Electrons that are subjected to the crossed electric and magnetic fields are cycled between the cathode endplates with a superimposed cycloidal motion [Red59]. The cycloidal motion radius $R_c$ depends on both the magnetic field and the electron velocity component that is perpendicular to the magnetic field, as shown in Fig. 4-24 (b). Only the electron trajectory is extended by the crossed electric and magnetic fields; the ionized gas molecules are drawn to the cathode without delay because the ions are much heavier than the electrons and thus are minimally affected by the magnetic field.

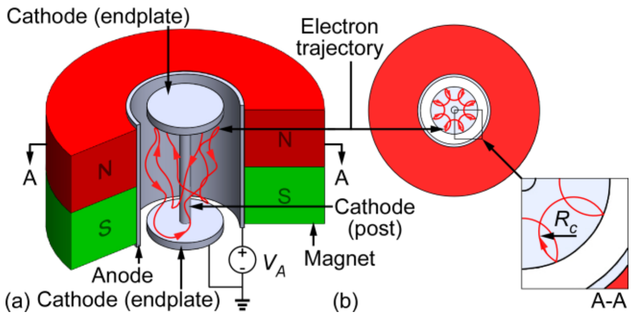

Figure 4-24: The magnetron gauge consists of an anode, a cathode, and a magnet. (a) 3D schematic. (b) A-A section view. The radius of the electron cycloidal motion $R_c$ is shown in the zoom in inset.

As shown in Fig. 4-25, the magnetron gauge design (Design M.O) has an anode, a cathode, and a magnet. However, the cathode consists of two endplates and a center post that interconnects them, rather than two separate cathode plates as in the Penning cell gauge designs. An anode cylinder with an inner diameter of 5.6 mm is used to enclose the cathode concentrically. Electric field lines are mostly radially-directed from the anode to the cathode post when the cathode is grounded and the anode is biased at $V_A$. A ring magnet (K&J magnetics, R844, 1/2" OD, 1/4" ID, 1/4" thick, magnetization direction: axial) encircles the anode, and the two cathode endplates are spaced 6.4 mm apart – coplanar with the magnet end surfaces. Magnetic flux lines passing through the magnet through-hole are mostly perpendicular to the cathode endplates, and parallel to the cathode post. Therefore, the electric and magnetic fields are more strongly crossed than the Penning cell gauge designs, which assists in confining the electrons within spiral loops inside the anode for gas ionization. The overall volume of this gauge is 0.18 cm$^3$ (excluding the magnet). Glass is assumed to seal the gauge between top cathode endplate and the anode, and whereas the lower perimeter is assumed to be sealed to the CDG to allow the interior pressure to equilibrate. The proposed geometry of Design M.O is analyzed with the simulation model M.O.Sim. The analysis is based on the approach described in section 4.1.1.

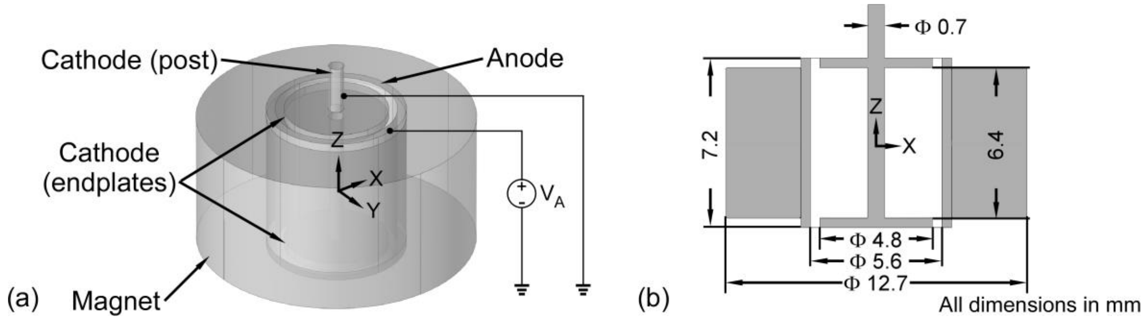

Figure 4-25: FEA model of Design M.O – M.O.Sim. Anode is biased at $V_A$, and cathodes are grounded. (a) 3D schematic. (b) X-Y section view. (c) X-Z section view.

The simulations show that the electric field lines are directed mostly radially, which is expected because the anode cylinder and cathode post are concentric (Fig. 4-26 (a)). The magnetic flux density ranges from 0.28 T to 0.43 T, as shown in Fig. 4-26 (b). While the flux densities in this range are larger than the critical flux densities $B_c$, found for Penning cell geometries in the parametric study (section 4.1.2), the critical flux densities for magnetron geometries have not been studied. To estimate the electron trajectory, electrons are released from two different positions – 1 µm away from the cathode endplate at the center point along the Y axis and 1.4 mm along the X axis, and 1 µm away from the cathode post at the center point along both Y and Z axes. Again, the initial velocity of the electron is 1.229 x $10^6$ m/s, normal to the cathode surface. Infinite electron spiraling starts at $V_A$ from 700 V to 1000 V for both cases, and patterns of both trajectories are the same (Fig. 4-27). The design parameters and simulation results of the Design M.O are summarized in Table 4-2.

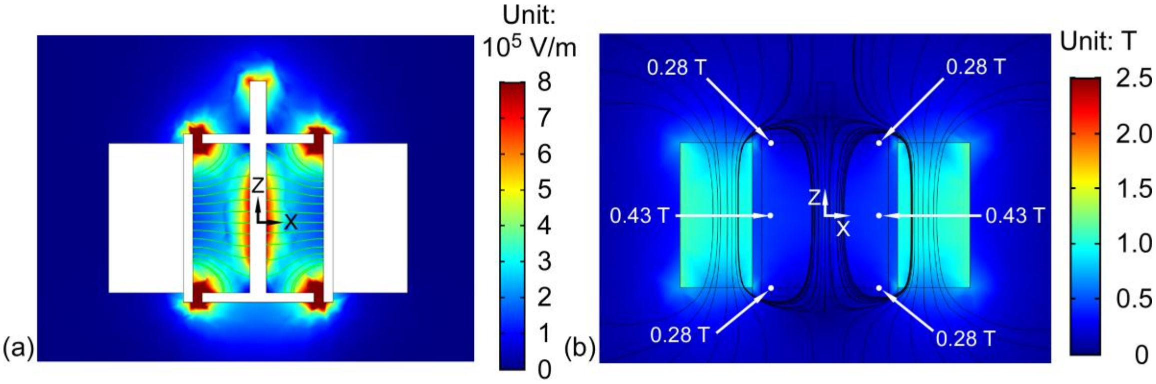

Figure 4-26: The simulation results of M.O.Sim. (a) The electric field at X-Z section (anode voltage $V_A$ of 700 V). (b) The magnetic flux density at X-Z section.

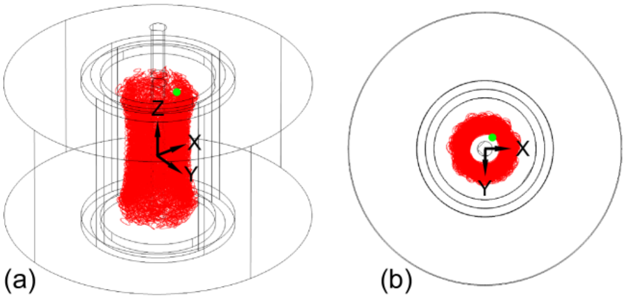

Figure 4-27: The electron trajectory at anode voltage $V_A$ of 700 V in M.O.Sim from the simulation result. The red line is the integrated electron trajectory, and the green dot is the electron end position (inside the anode cylinder, without terminating into the anode). (a) 3D schematic. (b) X-Y section view.

Table 4-2: Design parameters and simulation results of the Design M.O.

| | |
|---|---|
| Design parameters | Cathode endplates: 4.8 mm diameter, 6.4 mm gap;<br>Cathode post: 0.7 mm diameter;<br>Anode: 5.6 mm inner diameter, 6.4 mm outer diameter, 7.2 mm long;<br>Magnet: Neodymium N42 grade ring magnet, 6.4 mm inner diameter, 12.7 mm outer diameter, 6.4 mm long; |
| Simulation results | Axisymmetric electric and magnetic fields along the cathode post;<br>Infinite electron spiraling from 700 V to 1000 V; |

## 4.3 Designing for Manufacturability

All foregoing designs were based on loosely defined dimensional constraints. However, additional manufacturability requirements – such as fabrication processes and material selections – that are necessary to ensure the proposed CCGs can be integrated to the CDG.

### 4.3.1 Manufacturability Requirements

For all the designs considered, glass was assumed to seal the gauge and to provide electrical isolation between the anode and cathode. A high temperature glass reflow process is used to produce the seal by placing glass and metal parts on a conveyor (along with an alignment fixture) to go through an oven that consists of three consecutive temperature zones: 980 °C, 750 °C, and 550 °C. However, the axial thickness of the glass must be at least 1.6 mm (1/16") based on typical Ferran standards in order to withstand the differential pressure across the seal. Additionally, to prevent arcing through the air on the air side of the gauge, the electrodes must be sufficiently separated to limit the electric field well below the breakdown field strength for air of 3 kV/mm [Tip07]. In addition, the glass seal must be in a circular or ring shape as these shapes are less likely to experience an unevenly distributed stress (especially shear stress) after the high temperature glass reflow process. Shear stress can easily result in fracture of the glass. For a cascaded metal-glass-metal seal, the inner metal must have a lower coefficient of thermal expansion (CTE) than the outer metal. This allows a compressive stress to build across the seal for better glass-metal bonding strength after the glass reflow process. Titanium with a CTE of 8.6 ppm/°C is often used as the inner metal, and 316 stainless steel with a CTE of 15.9 ppm/°C is typically used as the outer metal. Both of the metal choices are vacuum compatible and paramagnetic, resulting in minimum effects on the resulting magnetic field.

Based on the application of the CDG, the gauge may be occasionally exposed to corrosive processing gases. Therefore, the gauge materials must be corrosion resistant. Titanium and 316 stainless steel are appropriately corrosion resistant. The commercially available magnets are nickel plated for corrosion resistance. The magnetic return path material, assumed to be low carbon steel or soft iron in the simulations in sections 4.1 and 4.2, is not sufficiently corrosion resistant. In this section, the simulations assume the magnetic return path material to be 430 stainless steel. A final consideration is the assembly process for integrating the gauge with the CDG. For this a hole is perforated through the CDG ring to the reference chamber, and the gauge case is then welded to the CDG ring at the bottom of the CDG ring. The following sections investigate designs that build on the previous designs while accommodating these manufacturability concerns.

### 4.3.2 Penning Cell Gauge Designs (Design P.MF.1, Design P.MF.2, Design P.MF.3)

Design P.MF.1 is refined from all the investigated Penning cell CCG designs to allow better electron confinement and gauge manufacturability. Design P.MF.2 is developed to investigate the adjustability of the magnetic circuit of Design P.MF.1. Design P.MF.3 is developed to investigate the further miniaturization of Design P.MF.1.

#### 4.3.2.1 Design P.MF.1

A Penning cell gauge design – Design P.MF.1 – is refined to allow better electron confinement. As shown in Fig. 4-28, Design P.MF.1 consists of a cylinder case, an anode, and a magnetic circuit that includes two circular magnets (K&J magnetics, D52-N52, 5/16" diameter, 1/16" thickness, magnetization direction: axial) and a U-shaped magnetic return path; all of these are similar to the gauge architecture of the curved cathode design (Design P.C). The case is 8.8 mm in diameter and 17.8 mm in height, which is 6 mm longer than Design P.C. Two flat cathode plates are added to the case to create flat cathode surfaces that are spaced 6 mm apart. These titanium plates have the same curvature as the case on one side, and are flat on the other side. Such adjustment is adapted from the flat cathodes design (Design P.F), as previous simulation results suggest the flat cathodes are much more likely to generate infinite electron spiraling. The anode with a diameter of 5 mm and length of 4 mm is centered between the flat cathode plates with its axis perpendicular to the flat cathode surfaces.

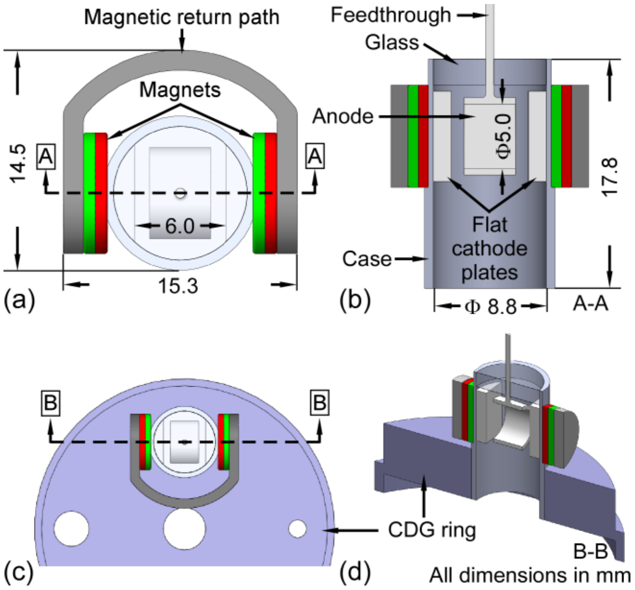

Figure 4-28: Schematic of Design P.MF.1 geometry (a) 3D, (b) A-A section. Relative position between Design P.MF.1 and CDG ring after assembly (c) top, (d) B-B section.

To address the manufacturability requirements in section 4.3.1, several structural improvements are adapted into Design P.MF.1. First, end notches and flat surfaces will be milled outside the case cylinder where the magnets are placed to hold the magnets (Fig. 4-29). The alignment of magnets is also simplified with this improvement because the notches have the same edge profile as the disc magnets. In addition, the extended length of the case allows the welding between the gauge and CDG ring, and provides enough clearance between the external magnetic circuit and CDG ring (Fig. 4-28 (c)). Second, glass will be used to seal the Design P.MF.1 between the case and the feedthrough that provides the electrical access to the anode. The axial thickness of the glass is 2 mm to withstand differential pressure. The radial separation between the feedthrough and case is 4 mm to prevent arcing in air. Third, the feedthrough and both flat cathode plates are to be made from titanium, and the case is to be made from 316 stainless steel rather than titanium to meet the CTE requirements for the glass seal.  The cathode plates can be welded to the case.

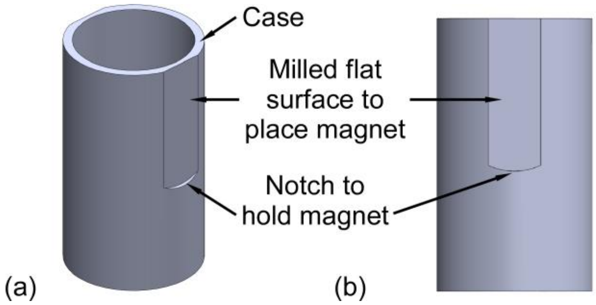

Figure 4-29: Case in Design P.MF.1.  Flat surfaces and end notches are machined to hold magnets.

Before simulating the Design P.MF.1 with the FEA approach that is defined in section 4.1.1, the geometry of Design P.MF.1 is simplified for simulation purposes in simulation model P.MF.1.Sim, as shown in Fig. 4-30.  First, a segment of the case is included in the simulation model, and flat surfaces are extended all the way from top to bottom outside the case; these features do not affect the resulting electric and magnetic fields inside anode.  Second, the volume where the glass is located is defined as part of the air block, as air shares similar electric and magnetic properties as glass.  In P.MF.1.Sim, the flat cathode plates and the case are grounded; the feedthrough and the anode are biased at $V_A$.  The flat cathode plates, the case, the feedthrough and the anode are assumed to be titanium in the model.  The magnetic return path material is assumed to be 430 stainless steel, and its non-linear magnetic property defined by the B-H curve in COMSOL (Fig. 4-31) is used to investigate potential magnetic saturation.

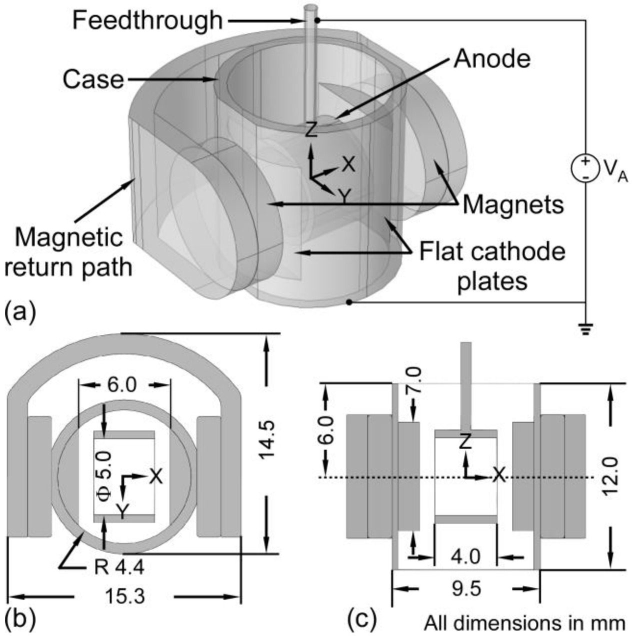

Figure 4-30: FEA model of Design P.MF.1 – P.MF.1.Sim. Anode is biased at $V_A$, and flat cathode plates and case are grounded. (a) 3D schematic. (b) X-Y section view. (c) X-Z section view.

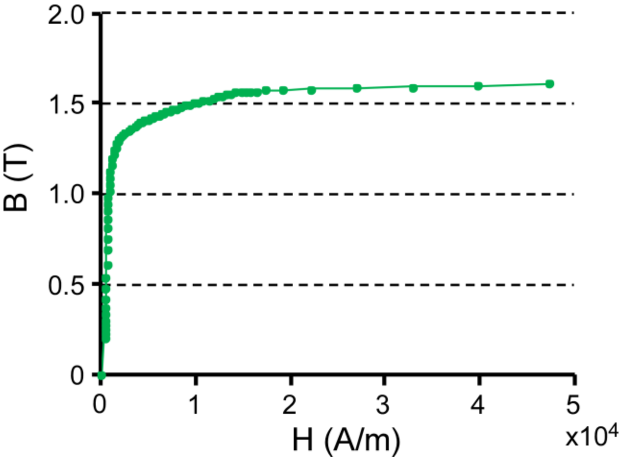

Figure 4-31: B-H curve of the 430 stainless steel [Bra06].

The resulting electric and magnetic fields are axisymmetric about the anode axis (Fig. 4-32), just as in the flat cathodes design (Design P.F). The estimated magnetic field strength is comparable to the magnetic field in the curved cathode design (Design P.C) when the magnetic return path consists of soft-iron. The magnetic field in the center of the anode is 0.18 T compared to a threshold $B_c$ of 0.10 T that was identified in section 4.1.2. An electron is released 1 µm away from the cathode plate at the center point along the Z axis, and radially at 1.5 mm from the center of the Y axis to simulate its trajectory under the electric and magnetic fields from P.MF.1.Sim. According to the simulation results, the electron spirals infinitely at anode voltage $V_A$ of 900 V and 1000 V (Fig. 4-33).

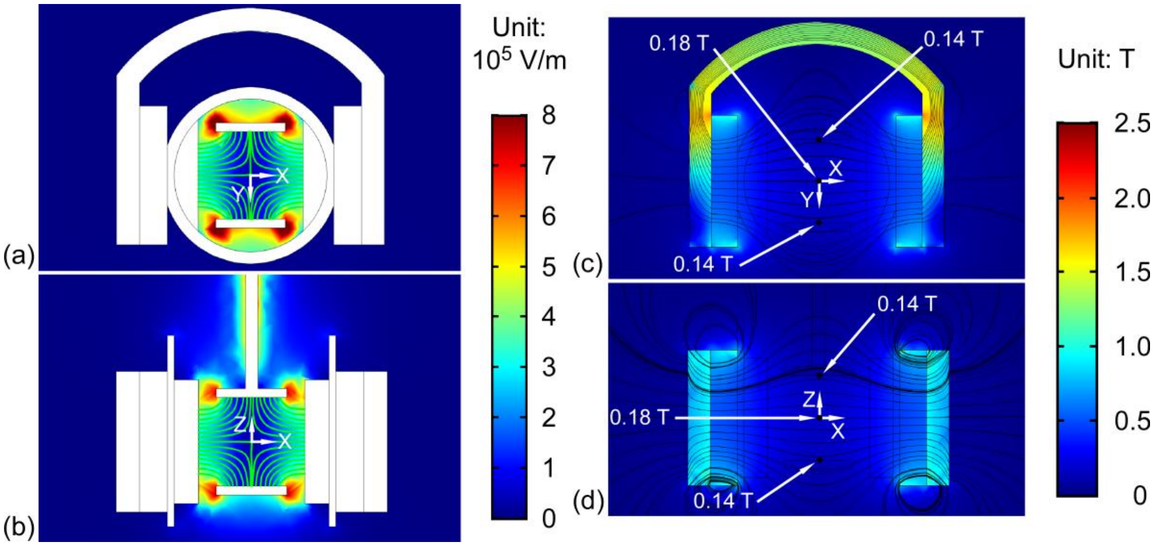

Figure 4-32: The simulation results of P.MF.1.Sim. The electric fields at (a) X-Y section view and (b) X-Z section view (anode voltage $V_A$ of 900 V). The magnetic flux density at (c) X-Y section view and (d) X-Z section view.

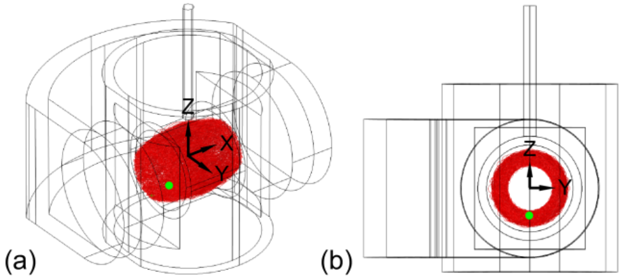

Figure 4-33: The electron trajectory at anode voltage $V_A$ of 900 V in P.MF.1.Sim from the simulation result. Electron is released at (X, Y, Z) = (–3.0 mm+1 µm, –1.5 mm, 0 mm). The red line is the integrated electron trajectory, and the green dot is the electron end position (inside the anode cylinder, not terminating into the anode). (a) 3D schematic. (b) Y-Z section view.

Although not a mandatory aspect of the gauge design, the material composition of Design P.MF.1 might allow the gauge to provide auxiliary (sputter) pumping. This is due to the fact that titanium, the flat cathode plate material, is a getter material that used is to chemisorb chemically reactive gasses. Any auxiliary pumping is desirable to extend the lifetime of the reference vacuum in the CDGs.

#### 4.3.2.2 Design P.MF.2

There are multiple perforations (opening 1, 2, 3 in Fig. 4-34 (b) and (d)) on the CDG ring that are reserved for other functional components (electrical connectors, pinch off tubes, etc.). To avoid potential interference between Design P.MF.1 and these functional components, the dimension of the external magnetic circuit is adjusted in Design P.MF.2. The Design P.MF.2 (Fig. 4-34 (c) and (d)) consists of two smaller diameter magnets (K&J magnetics, D41-N52, 1/4" diameter, 1/16" thickness, magnetization direction: axial) and a compact magnetic return path. The diameter of the magnets is 6.4 mm, which is still larger than the diameter of anode. The magnetic return path is flattened toward the case of the gauge, increasing the space between the path and the CDG opening 2.

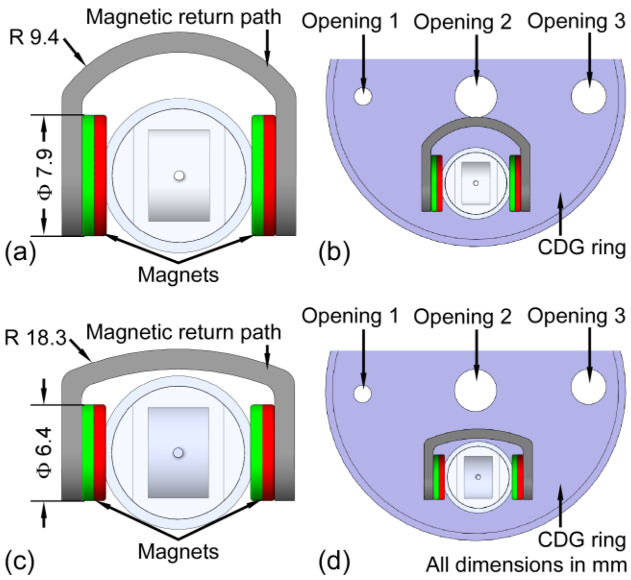

Figure 4-34: Design P.MF.2 with smaller magnets and compact magnetic return path. The Design P.MF.1 (a) top view, and (b) assembled to CDG ring. The Design P.MF.2 (c) top view, and (d) assembled to CDG ring.

The Design P.MF.2 is analyzed with the simulation model P.MF.2.Sim, which is similar to P.MF.1.Sim. Simulations show the electric field for this design (Fig. 4-35 (a) and (b)) is the same as that for Design P.MF.1. The magnetic field is 0.14 T at the center of the anode, which is 22% lower in magnitude (Fig. 4-35 (c) and (d)) when compared to the results in Design P.MF.1. The electron can spiral infinitely at $V_A$ of 900 V when the release position is moved inward radially from 60% of the anode radius to 40% of the anode radius (Fig. 4-36). This change in release point is required because the electron is less tightly confined radially by the reduced magnetic field. This modest compromise in the confinement is not expected to have a major effect on the basic functionality of the gauge. Since the magnetic circuit is external to the gauge, it can be changed if necessary even after the gauge is embedded into the CDG.

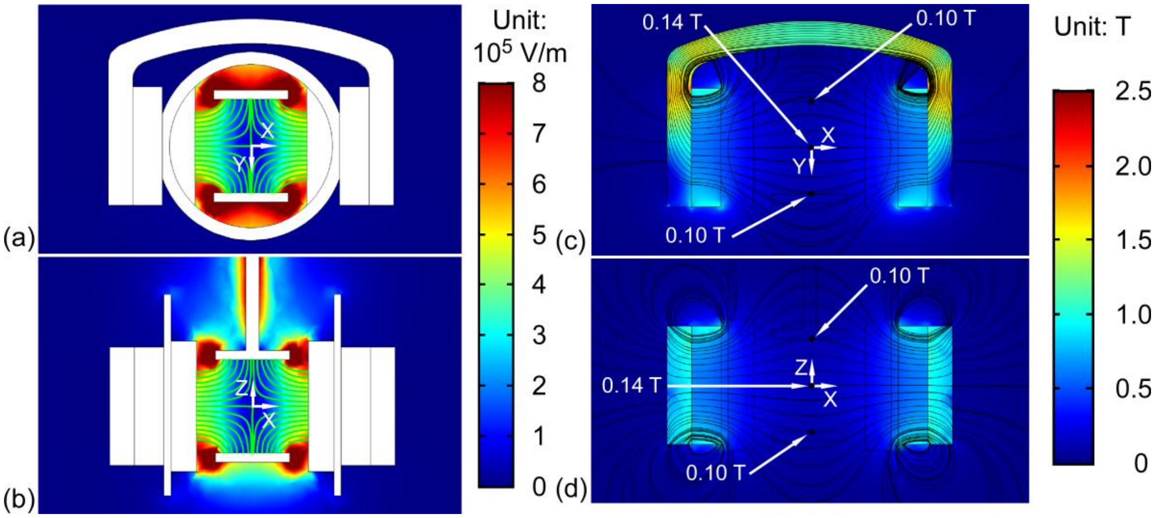

Figure 4-35: The simulation results of P.MF.2.Sim. The electric field at (a) X-Y section view and (b) X-Z section view (anode voltage $V_A$ of 900 V). The magnetic flux density at (c) X-Y section view and (d) X-Z section view.

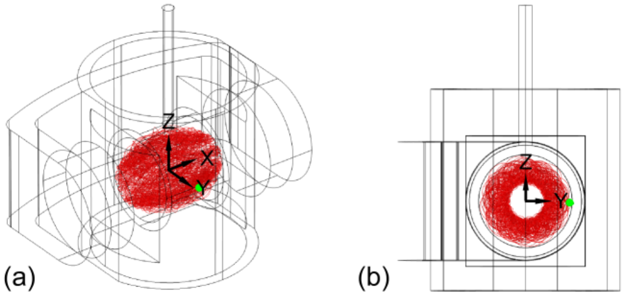

Figure 4-36: The electron trajectory at anode voltage $V_A$ of 900 V in P.MF.2.Sim from the simulation result. Electron is released at (X, Y, Z) = (–3 mm+1 μm, –1 mm, 0 mm). The red line is the integrated electron trajectory, and the green dot is the electron end position (inside the anode cylinder, not terminating into the anode). (a) 3D schematic. (b) Y-Z section view.

#### 4.3.2.3 Design P.MF.3

The Design P.MF.1 is further miniaturized to investigate the electron spiraling within a smaller geometry, as shown in Fig. 4-37. For this design, the case diameter is decreased to 5.7 mm, while two flat cathode plates are reduced in size and are separated by a gap of just 3.0 mm. The anode is 2.0 mm in diameter and 1.0 mm in thickness, maintaining 1.0 mm gaps between the anode and cathodes. The magnetic circuit is miniaturized accordingly, with two smaller magnets (K&J magnetics, D31-N52, 3/16" diameter, 1/16" thickness, magnetization direction: axial) and a smaller magnetic return path. Design P.MF.3 will provide a larger clearance to other CDG components after assembly. The gauge volume, not including the magnetic circuit, is reduced from 1.1 cm$^3$ in Design P.MF.1 to 0.3 cm$^3$ in Design P.MF.3. The distributions of electric and magnetic fields are similar as the simulation results in Design P.MF.1, but the magnetic field is almost doubled in magnitude inside the anode (from $\approx$0.26 T to $\approx$0.38 T) because the magnets are more closely spaced. This geometry is not within the range studied parametrically (section 4.1.2), so the critical flux density $B_c$ is not known. However, as shown in Fig. 4-38, the electron can spiral infinitely at anode voltage $V_A$ from 700 V to 1000 V when it is released near the cathode, 1 µm away from the cathode plate at the center point along the Z axis, and radially at 0.6 mm from the center of the Y axis.

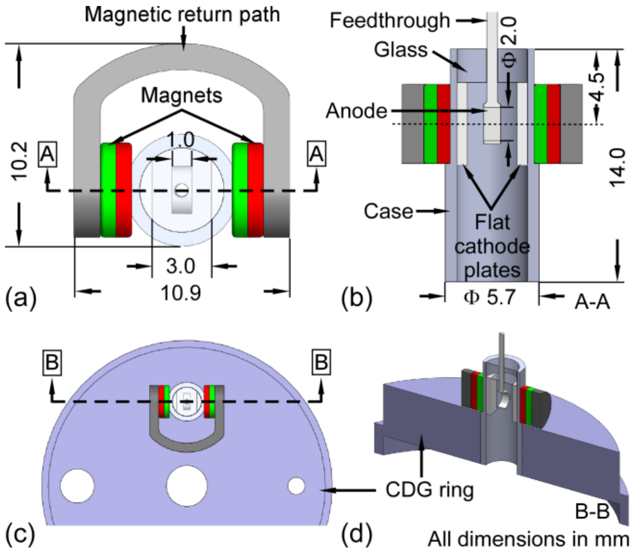

Figure 4-37: Schematic of Design P.MF.3 geometry (a) 3D, (b) A-A section. Relative position between Design P.MF.3 and CDG ring after assembly (c) top, (d) B-B section.

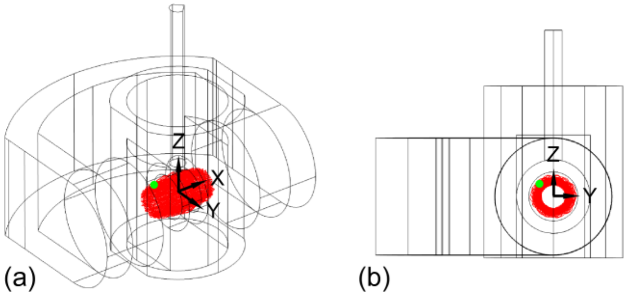

Figure 4-38: The electron trajectory at anode voltage $V_A$ of 700 V in Design P.MF.3 from the simulation result. Electron is released at (X, Y, Z) = (–1.5 mm+1 μm, –0.6 mm, 0 mm). The red line is the integrated electron trajectory, and the green dot is the electron end position (inside the anode cylinder, not terminating into the anode). (a) 3D schematic. (b) Y-Z section view.

Although Design P.MF.3 is capable of infinite electron spiraling, the ion current that represents the pressure may be smaller because total ion counts are fewer inside a smaller volume. The minimum ignition pressure for Design P.MF.3 may be slightly higher than that of Design P.MF.1 as well, due to an inability to store as much space charge within the miniaturized volume. In addition, Design P.MF.3 has a higher possibility of experiencing arcing in air, as the feedthrough and case are more closely spaced.

### 4.3.3 Magnetron Gauge Design (Design M.MF)

The magnetron design (Design M.O) has been improved in structure and electrical arrangement. The result of these refinements is defined as Design M.MF (Fig. 4-39). This design still consists of a cathode, an anode, and a ring magnet as in Design M.O. The cylinder anode is 5.6 mm in diameter and 17.3 mm in length, which is 10 mm longer than the anode in Design M.O. The ring magnet (K&J magnetics, R844, 1/2" OD, 1/4" ID, 1/4" thick, magnetization direction: axial) is the same compared to Design M.O. The center post of the cathode is 0.7 mm in diameter and connects the two 4.8 mm diameter cathode endplates that are spaced 7.2 mm apart. The cathode endplates are oriented concentrically with the anode and are offset by 0.4 mm from the end surfaces of the magnet on both ends. As the simulations will show, the offset provides orientations of electric and magnetic fields that are favorable for spiraling.

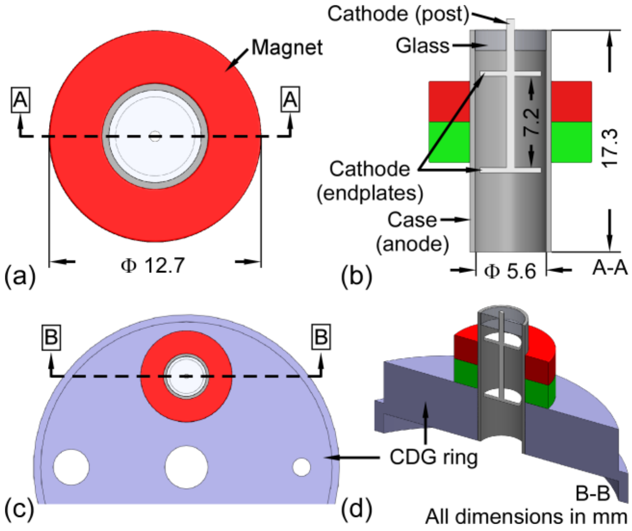

Figure 4-39: Schematic of Design M.MF geometry (a) 3D, (b) A-A section. Relative position between Design M.MF and CDG ring after assembly (c) top, (d) B-B section.

The geometry of Design M.MF is able to address the manufacturability requirements for gauge integration to the CDG. The extended case cylinder can bury both cathode endplates below the ring glass to address two manufacturability issues. First, the metal-glass-metal seal now appears between the case and cathode post rather than between the case and the cathode endplate as in Design M.O, which increases the separation between the cathode and the anode from 0.4 mm in Design M.O to 2.5 mm in Design M.MF on the air side of the gauge. This meets the separation requirement prevent electrical arcing in air. Second, the case is sealed to the bottom of CDG ring (Fig. 4-39 (d)), but the extended case length allows the external magnet and both cathode endplates to exist in an extension above the CDG opening. Since the anode as well as the case are electrically shorted to the grounded CDG ring, the cathode is biased at a negative high voltage $V_K$ to maintain the same potential difference between the anode and cathode.

The simulation model of Design M.MF (M.MF.Sim) that is based on the analytical approach described in section 4.1.1 is shown in Fig. 4-40. In consideration of computational efficiency, glass is not included and the full length of the case is not included in the simulation model. Both anode and cathode are assumed to be titanium. The anode is grounded, while the cathode is biased at $V_K$.

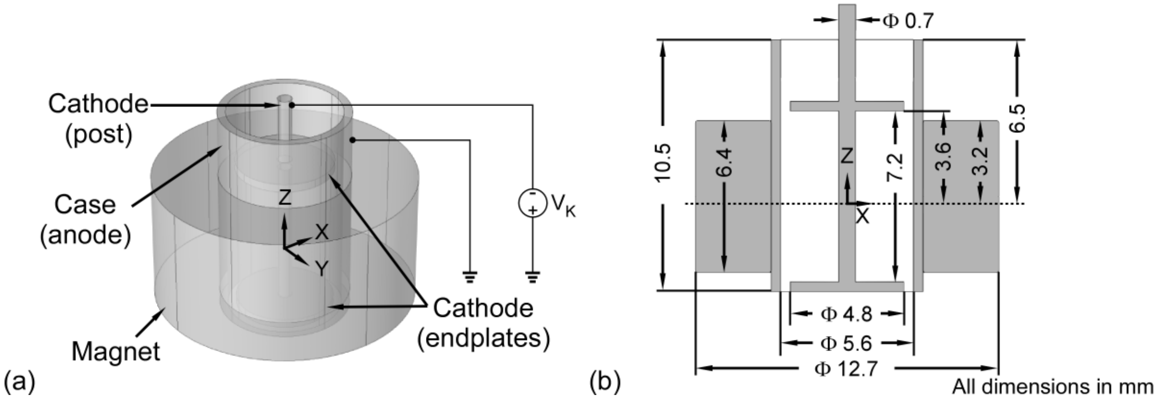

Figure 4-40: FEA model of Design M.MF – M.MF.Sim. Anode is grounded, and cathode is biased at negative high voltage $V_K$. (a) 3D schematic. (b) X-Z section view.

Simulations indicate that the electric and magnetic fields are identical to the previous magnetron design (Design M.O); however, the region where the electric and magnetic fields are crossed extends close to the cathode endplates (Fig. 4-41). This is expected, as magnetic flux lines are bent radially and electric field lines are directed towards the endplates when the cathode endplates are aligned slightly outside the end surfaces of the ring magnet. Infinite electron spiraling is initiated at a cathode voltage $V_K$ from –500 V to –1000 V for electrons released 1 μm away from the cathode endplate at the center point along the Y axis, and radially at 1.6 mm from the center of the X axis; and

1 µm away from the cathode post at the center point along both Y and Z axes. Both release locations result in identical spiraling patterns (Fig. 4-42). The magnitude of the required voltage for spiraling is slightly less for Design M.MF (500 V) compared to Design M.O (700 V) due to the different orientation of the electric and magnetic fields near the cathode plates.

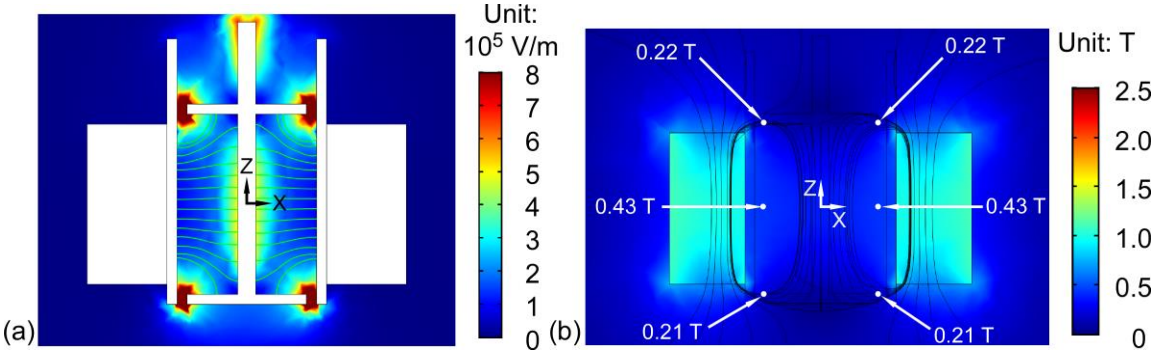

Figure 4-41: The simulation results of M.MF.Sim. (a) The electric field at X-Z section (cathode voltage $V_K$ of –500 V). (b) The magnetic flux density at X-Z section.

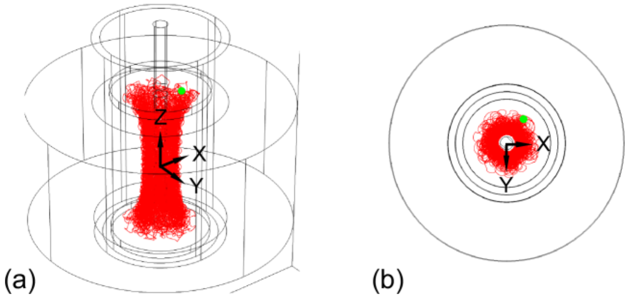

Figure 4-42: The electron trajectory at cathode voltage $V_K$ of –500 V in M.MF.Sim from the simulation result. Electrons release from cathode endplates or cathode post are spiraled infinitely in a same pattern. The red line is the integrated electron trajectory, and the green dot is the electron end position (inside the anode cylinder, without terminating into the electrode boundaries). (a) 3D schematic. (b) X-Z section view.

### 4.4 Design for a Standard Vacuum Feedthrough (Design M.S)

In section 4.3, four CCG designs were refined to meet additional manufacturability requirements for their integration to the CDG. However, those manufacturing refinements, such as the metal-glass-metal seal and the welding between the CCG and the CDG, are specific to the Ferran gauge. An alternative design that is compatible with standard vacuum feedthroughs is desirable, allowing more widespread use and retrofitting with existing vacuum chambers. Such an alternative is described in this section.

### 4.4.1 Design and Structure

Compatibility with a SHV feedthrough requires some adjustments from the previously described designs. The Design M.MF has been adjusted in structure and fabrication processes to result in Design M.S, as shown in Fig. 4-43. This design consists of an anode, a cathode, two spacers, and two ring magnets. The cylindrical anode is 44.8 mm long and is open on one end. On the other end, the 6.4 mm diameter anode endplate is perforated with multiple 0.6 mm diameter holes; these holes allow gas conductance through the anode and into the gauge. The anode outer diameter enlarges from 6.4 mm to 12.7 mm at 12.4 mm away from the anode endplate. This creates a ring flat against which to abut the two 6.4 mm thick ring magnets with an outer diameter of 12.7 mm and an inner diameter of 6.4 mm (K&J magnetics, R844, magnetization direction: axial). The cathode is 29.5 mm with two 3.5 mm diameter cathode endplates that are spaced 6.0 mm apart by a 1.0 mm diameter cathode post in the center. The 0.8 mm thick spacers, which have an inner diameter of 3.0 mm and an outer diameter of 5.0 mm, are used to prevent shorting between the anode and the cathode. Shallow annular grooves are engraved 1.0 mm away from the cathode post on the peripheral of both cathode endplates to hold these spacers on the circumferences of the cathode endplates. In addition, the spacers have a tooth-shape over their periphery to facilitate gas conductance.

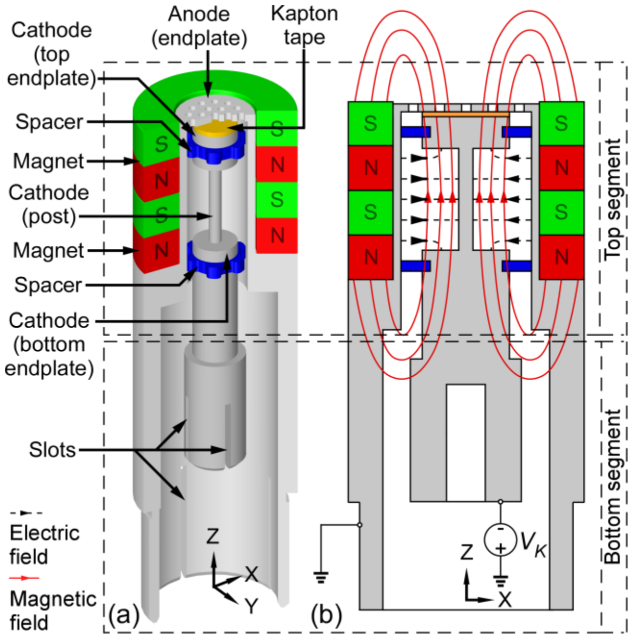

Figure 4-43: Schematic of Design M.S geometry (a) partially cropped 3D, (b) X-Z section.

From the design perspective, the geometry of Design M.S can be divided into two segments – the top segment and the bottom segment. The top segment is the active gauge where the electrons are trapped and energized for gas ionization and electric current measurement, while the bottom segment is similar to the standard vacuum side coaxial connector to the SHV feedthrough as shown in Fig. 4-44 (b). The gauge has an internal volume of 2.34 cm$^3$, and this volume is reduced to 0.30 cm$^3$ when only considering the active gauge volume. Such a modular design permits reliable electrical connections, precise alignment, and quick vacuum installation. Additionally, the Design M.S can be easily reconstructed to be retrofitted with other vacuum connections by only changing the bottom segment.

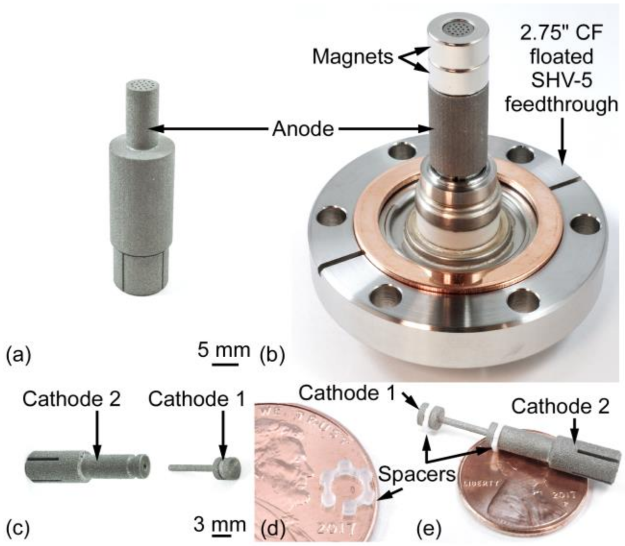

Figure 4-44: (a) The DMLS fabricated anode. (b) The assembled Design M.S on the 2.75" CF floated SHV-5 feedthrough. (c) The DMLS fabricated cathode 1 and cathode 2. (d) The 3D printed spacer. (e) The assembled cathode with spacers in place.

In this Design M.S, the diameter of the bottom cathode endplate is enlarged to 4.8 mm, and a 2.4 mm diameter and 9.2 mm deep pin well is designed on the bottom cathode endplate to allow the cathode to be pushed onto the center pin of a floated SHV feedthrough. This controls the relative position between the cathode and the feedthrough. The anode is designed to be pushed onto the grounding shield of the same feedthrough by increasing its inner diameter from 5.0 mm to 9.7 mm at 15.8 mm away from the anode endplate to avoid the interference between the anode and the center pin base of the feedthrough. The anode outer diameter reduces from 12.7 mm to 11.4 mm at 10.2 mm away from the opening of the anode. This defines the depth that the anode can be pushed into the ground shield of the feedthrough, and the relative position between the ring magnets and the cathode. Additionally, slots are included in the cathode and the anode where the electrodes connect to the feedthrough. These slots allow these portions of the cathode and anode to slightly deform to result in reliable push-on connections to the feedthrough. Through these efforts, all parts are oriented concentrically.  The space between the two cathode endplates is fully enclosed inside the ring magnets where the magnetic field is the strongest and the most uniform.

In order to minimize the stray electric field when using the magnetron gauge, the electrical biasing of the Design M.S is different compared to the typical magnetron gauge where the anode is biased at a positive high voltage $V_A$ while the cathode is grounded [Red59].  In Design M.S, the anode is grounded and the cathode is biased at a negative high voltage $V_K$ to maintain the same electric field between the anode and the cathode as in the traditional biasing scheme.  This adjustment allows the high voltage to be fully shielded inside the anode.

### 4.4.2 Fabrication and Materials

To expedite the fabrication of Design M.S and to explore the suitability of such rapid prototyping processes for vacuum devices, different 3D printing technologies are used. Both the cathode and the anode are fabricated with the direct metal laser sintering (DMLS) process – provided by the GPI Prototype & Manufacturing Services® – from 316L stainless steel powder [DML17].  This DMLS process is capable of building complex parts layer-by-layer (layer thickness as small as 20 µm) with high detail resolution, good surface quality, and superior material consistency.  The 316L alloy of stainless steel is frequently used in all kinds of vacuum products, due to its low outgassing rates.  It also is considered a non-magnetic material.  Thus, the gauge material has little reaction to the magnetic field, which desirably maintains uniformity of the magnetic field inside the top segment of the gauge.  The spacers are 3D printed with ProJet® 3500 HD from M3 crystal, which is an acrylic based resin [Pro17].  Acrylic has a high enough dielectric strength at 17 kV/mm to prevent the electrical breakdown between the cathode and the anode [Acr17]. The final piece added to prevent shorting between the electrodes is a circular KAPTON® (polyimide) tape placed on top of the top cathode endplate (300 μm thick, 233 kV/mm dielectric strength [Dia10]). The ring magnets are N42 grade neodymium magnets with the decision criteria including cost, magnetic field strength versus size, and commercial availability.

To allow the production of the cathode while utilizing the DMLS process, the original design of the cathode is separated into two parts – cathode 1 and cathode 2. Cathode 1 consists of the top cathode endplate and the cathode post of the original (one piece) cathode. However, the post is elongated for an additional 3.0 mm. Cathode 2 consists of the rest of the original (one piece) cathode, but a 1.0 mm diameter and 3.0 mm deep center hole is perforated on bottom endplate. To assemble a single cathode, the post of cathode 1 is inserted into the center hole of cathode 2, and a small interference between the two parts at this location maintains the assembly. The DMLS fabricated anode and cathodes are shown in Fig. 4-44 (a) and (c). The printed spacer is shown in Fig. 4-44 (d), and the assembled cathode with the spacers in place is shown in Fig. 4-44 (e).

### 4.4.3 Modeling

For investigation of the electron spiraling in the Design M.S, a three-dimensional finite element analysis model (M.S.Sim) incorporating electrostatic field and magnetic field physics modules is developed in COMSOL Multiphysics based on the analytical approach discussed in section 4.1.1 [COM17]. In the M.S.Sim, only the top segment of the Design M.S that contains the active gauge geometry is considered for computational efficiency, as shown in Fig. 4-45. In addition, two spacers, the grooves around the cathode endplates, and the anode endplate are not included in the model; these features are expected to be inconsequential in the electron spiraling performance.  The considered gauge geometry is centered and enclosed in a large air block (12 x 12 x 12 $cm^3$), and the material properties are assigned to different gauge parts and air accordingly to reflect their magnetic properties.  Both the anode and the cathode are assigned 316L stainless steel magnetic properties with a relative permeability of 1.6 [Wil91].  The modeling domains that represent the N42 grade magnets are assigned a remanent magnetic flux density $\boldsymbol{B_r}$ of 1.3 T along their axial magnetization direction, and a relative permeability of 1.05 [Neo17].

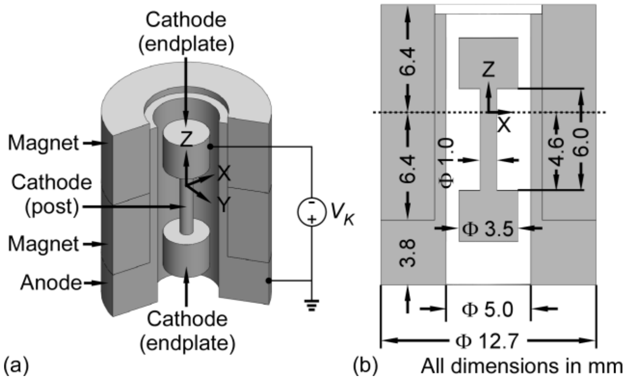

Figure 4-45: FEA model of Design M.S – M.S.Sim.  Anode is grounded, and cathode is biased at negative high voltage $V_K$.  (a) 3D schematic.  (b) X-Z section view.

Simulation results show that the electric field lines are mostly radially directed from the cathode post to the anode (Fig. 4-46 (a)), which is expected because the anode cylinder and cathode post are concentric.  From the simulation result in Fig. 4-46 (b), the magnetic flux lines passing through the magnet through-hole are mostly perpendicular to the cathode endplates and parallel to the cathode post.  In the volume between two cathode endplates, the magnetic flux density is 0.25 T at the bottom of the top cathode endplate at its maximum value, and is 0.19 T at the top of the bottom cathode endplate at its minimum value.  The cathode features are not centered inside the stacked ring magnets along the Z axis, which leads to the asymmetric distribution of the flux density along the X-Z plane.

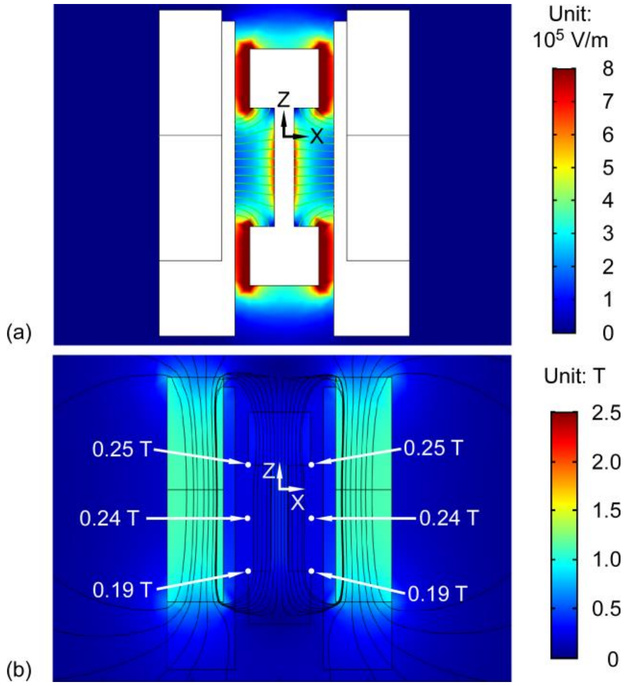

Figure 4-46: The electric and magnetic simulation results of M.S.Sim. (a) The electric field at X-Z section (cathode voltage $V_K$ of –600 V). (b) The magnetic flux density at X-Z section.

For the electron spiraling capability of the Design M.S, it is found that the infinite electron spiraling can be initiated at a $V_K$ from –600 V to –1000 V for electrons released 1 μm away from the cathode endplate at the center point along the Y axis, and radially at 1.2 mm from the center of the X axis; and 1 μm away from the cathode post at the center point along both Y and Z axes. The spiraling patterns for both releasing locations are identical (Fig. 4-47 (a)). For $V_K$ that is more positive than –600 V, –500 V for example, the released electron collides with the electrodes in the first few integration steps (Fig. 4-47 (b)). Note, the M.S.Sim model only considers the motion of a single electron that is emitted from the cathode surfaces in an ideal gauge. In reality, electrons can be produced from ionization events with a probabilistic velocity and position distribution, and their motion can be affected by the non-idealities of the gauge, such as localized electric field concentration due to the surface roughness, or such as misalignment of the magnetization axis to the gauge axis.

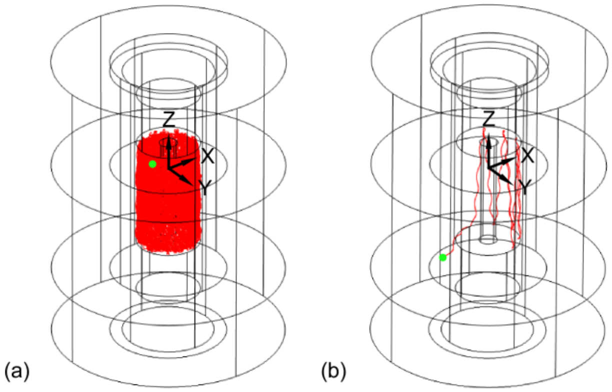

Figure 4-47: (a) The electron trajectory at cathode voltage $V_K$ of –600 V in M.S.Sim from the simulation result. The red line is the integrated electron trajectory, and the green dot is the electron end position (inside the anode cylinder, without terminating into the electrode boundaries). (b) The electron trajectory at cathode voltage $V_K$ of –500 V in M.S.Sim from the simulation result. The electron is terminated into cathode in the first a few integrations.

To estimate the gauge current $I_D$ at any given pressure $P$, Schuurman classified the modes and developed theories of crossed field discharges under different magnetic fields to correlate the $I_D$ with the gauge geometry and the experimental conditions [Sch67]. Typically, there are two modes of discharges in the crossed field gauges – the low magnetic field (LMF) and the high magnetic field (HMF) modes. In the LMF mode, the gauge current $I_D$ is independent of the anode voltage $V_A$, whereas in the HMF mode, the $I_D$ is sensitive to the $V_A$. The transition magnetic field $B_{tran}$ between these two modes is defined by [Sch67]:

$$B_{tran} = \sqrt{\frac{16V_A}{3\eta\beta r_a^2}} \tag{4-8}$$

where $\eta$ is the charge to mass ratio of the electron ($1.76 \times 10^{11}$ C/kg), $\beta$ is the probability of a gas ionization collision, and $r_a$ is the anode radius ($2.5 \times 10^{-3}$ m, in this case). The factor $\beta$ is experimentally acquired and the typical value is near 0.1 at various pressures, magnetic fields, and anode voltages [Sch67]. For the Design M.S, the estimated $B_{tran}$ at the $V_A$ of 1 kV is 0.048 T. The simulation results indicate that the magnetic field in the gauge is 4-5 times larger than this value. Therefore, the Design M.S should be operating in the HMF mode, in which the $I_D$ is given by [Pea90]:

$$I_D = kP^m \tag{4-9}$$

where $P$ is pressure in Torr; $k$ is the gauge sensitivity determined from experiments for given electric and magnetic fields, gauge geometry, and gas species (A/Torr); and $m$ is a pressure dependent exponent that is typically close to 1 for pressures above $10^{-8}$ Torr [Ken00].

### 4.4.4 Experimental Methods and Results

To characterize the Design M.S assembled on a 2.75" CF floated SHV feedthrough, the gauge is fully enclosed in a 2.75" CF flange vacuum chamber. The chamber is pumped by an all-in-one turbo pump (Agilent, Mini-TASK AG81). As shown in Fig. 4-48, the chamber pressure $P$ is adjusted by changing the leaking rate of a leak valve (Agilent, Variable Leak Valve) and is monitored by a commercial ion gauge (Adixen, AHC 2010). To bias the cathode at a negative high voltage $V_K$, a high voltage power supply (Stanford Research Systems, Model PS350) that supplies a source voltage of $V_S$ is in series with a 10 MΩ series ballast resistor to connect to the center pin of the SHV feedthrough. The anode is grounded through a low noise current pre-amplifier (Stanford Research Systems, Model SR570) at the floated shield of the SHV feedthrough while the current $I_D$ is measured by the same current pre-amplifier. In case of an unexpected short between the anode and the cathode, the current is limited by both the current limit of the high voltage power supply and the ballast resistor.

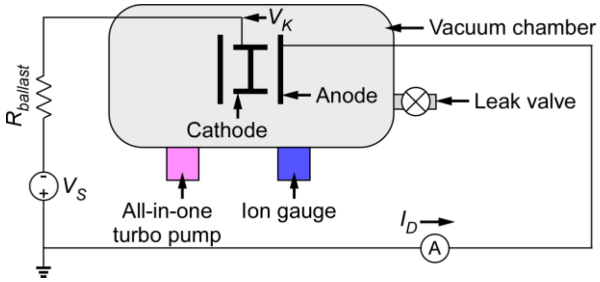

Figure 4-48: Experimental setup. The assembled Design M.S is placed in a vacuum chamber. The cathode is biased at a negative high voltage $V_K$. The anode is grounded. A 10 MΩ ballast resistor is used to limit the current. The gauge current $I_D$ is measured at anode. The chamber is pumped by an all-in-one turbo pump. The pressure is controlled by a leak valve and is monitored by a commercial ion gauge in the vacuum chamber.

The Design M.S was characterized at $V_S$ from –500 V to –3000 V. Before powering on the high voltage power supply at a $V_S$, the chamber was stabilized at a specific pressure. Upon switching the high voltage power supply on, a charging current occurred over several seconds. Once the target voltage was reached, the stable $I_D$ was immediately observed. The experimental conditions, such as the target $V_S$ and the pressure, were adjusted between tests when the high voltage power supply was off.

In the characterized pressure range and voltage range, the measured current $I_D$ is very repeatable. The $I_D$ as a function of chamber pressure at different $V_S$ that range from –750 V to –3000 V are plotted in Fig. 4-49. The variations of the $I_D$ at all characterized $V_S$ over separate tests were less than 2% when the pressure was higher than $10^{-4}$ Torr. For pressures lower than $10^{-4}$ Torr, the $I_D$ had higher variability over separate tests under some tested $V_S$, the ranges of which are represented by the vertical error bars in Fig. 4-49. Typically, the $I_D$ increased with the pressure at a specific $V_S$. The gauge startup pressure

$P_s$ – the lowest pressure at which the gauge provided a measurable current for a given voltage – from this data set is summarized as a function of $|V_S|$ in Fig. 4-50. The lowest $|V_S|$ that the gauge could start was 750 V, and the lowest $P_s$ was 10.5 µTorr at a $|V_S|$ of 750 V. The $P_s$ increased with increasing $|V_S|$. The $I_D$ versus $|V_S|$ at 50 µTorr, 100 µTorr, and 200 µTorr from this data set are replotted in Fig. 4-51. At the chamber pressure of 50 µTorr, the $I_D$ increased with the $|V_S|$ from 750 V to 1500 V and peaked at 5.7 µA when the $|V_S|$ was 1500 V. For $|V_S|$ higher than 1500 V, the $I_D$ decreased with increasing $|V_S|$ at this pressure level. Similar trends were observed at the chamber pressures of 100 µTorr and 200 µTorr, but the $I_D$ peaked at 18.7 µA when the $|V_S|$ was 1750 V at 100 µTorr, and at 74.0 µA when the $|V_S|$ was 2500 V at 200 µTorr.

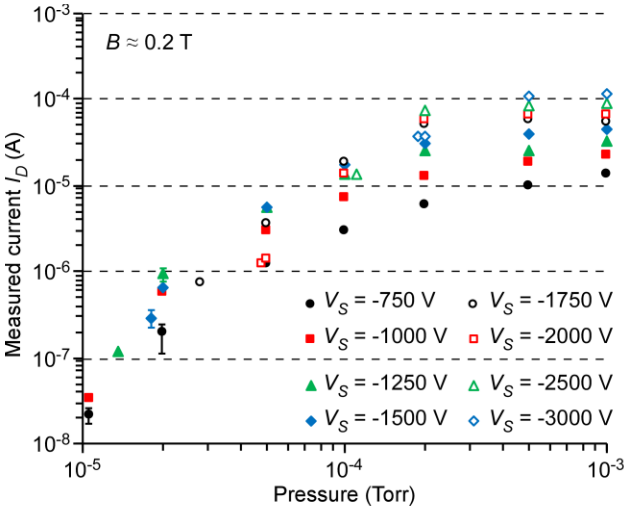

Figure 4-49: The gauge current $I_D$ at different $V_S$ and pressures from $10^{-3}$ Torr to $10^{-5}$ Torr. The lowest pressure data point at a specific $V_S$ is the gauge startup pressure at that specific $V_S$. Unless specified by the error bars at plotted data points, the variations of the measured $I_D$ are less than 2%.

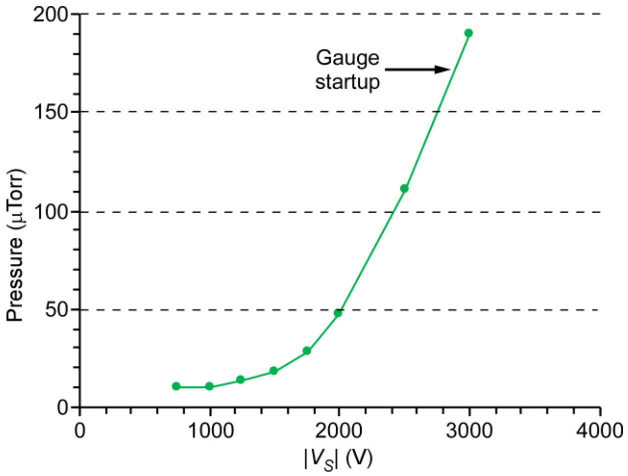

Figure 4-50: The gauge startup pressure versus the magnitude of $V_S$.

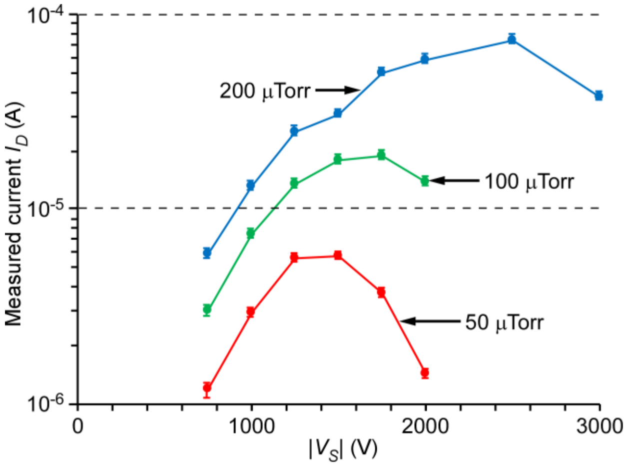

Figure 4-51: The gauge current $I_D$ versus the magnitude of $V_S$ at 50 µTorr, 100 µTorr, 200 µTorr.

### 4.4.5 Discussion

From the gauge startup results in Fig. 4-50, the lowest gauge startup $|V_S|$ was 750 V. This is close to the lowest voltage that led to an infinitely spiraling electron as identified by the simulation results (600 V). There are two possible reasons that impede the gauge from starting at a voltage lower than a $|V_S|$ of 750 V. First, the crossed electric and magnetic fields are unable to spiral the electrons over a long enough trajectory, as shown in the simulation result (Fig. 4-47 (b)). Thus, the electrons collide with the gauge surface rather than colliding with a gas molecule for gas ionization. Second, at pressures where the electrons are able to spiral longer than the mean free path for efficient collisions with gas molecules, the electric field at this low of a voltage is too weak to energize the electrons to gain enough kinetic energy for ionizing collisions. Similarly, these low electric fields and higher pressures result in low-energy ions upon collision with the cathode surfaces, resulting in lower secondary electron yield and an inability to sustain the discharge. For $|V_S|$ ranging from 750 V to 3000 V, the $P_s$ increased with $|V_S|$. The reason for this trend is that the average electron trajectory length is reduced at higher $|V_S|$, because the electrons gain more kinetic energy from the higher electric field and have a faster velocity that results in a motion with a larger cycloidal radius $R_c$ due to the magnetic field. This larger $R_c$ increases the probability of electrons to terminate into the electrode surfaces while cycling between the two cathode endplates. Therefore, the gauge could only start at a higher pressure at higher $|V_S|$, where the mean free path of the electron is comparable to the reduced electron trajectory.

At a chamber pressure of 50 µTorr, the $I_D$ peaked at 5.7 µA when $|V_S|$ was 1500 V in Fig. 4-51. For the $|V_S|$ lower than 1500 V, the $I_D$ increased with the $|V_S|$ for two reasons. First, the electron ionization rate is proportional to the $|V_S|$. At higher $|V_S|$, the average kinetic energy of the trapped electrons is higher, resulting in a larger ionizing cross-section and promoting more efficient gas ionization collisions [Lie94]. Second, the average electron trajectory increases with the $|V_S|$, because the cycloidal radius of the trapped electrons is larger when the speed of the electrons is faster at higher $|V_S|$. This increases the collision probability between the electrons and the gas molecules. Also, this experimental trend indicates the gauge is operated at HMF mode, because the $I_D$ is sensitive to the $|V_S|$ [Sch67]. Then, for the $|V_S|$ higher than 1500 V, the $I_D$ decreases as $|V_S|$ increases. As $|V_S|$ increases, the cycloidal radius of the electrons increases to be comparable to the gauge geometry, which dramatically increases the probability of the electrons to run into gauge surfaces. The average electron trajectory is reduced to be smaller than the mean free path of the electrons. In turn, the gas ionizations are limited by the reduced probability of collision between the electrons and the gas molecules. Such $I_D$ versus $V_S$ trend was similar to the work reported by Vesel [Vel02]. Additionally, the peak $I_D$ exists at a higher $|V_S|$ when the pressure increases. There are two reasons for this trend. First, the mean free paths of the electrons and gas molecules are shorter at higher pressure. Second, the average electron trajectory decreases with the $|V_s|$, as described previously. Thus, the average electron trajectory is comparable to the mean free path of the particles at a higher pressure when the Design M.S operates at a higher $|V_S|$. Finally, note that the $I_D$ increases with pressure at a given $|V_S|$ level, because the gas density increases with increasing pressure according to the ideal gas law. Therefore, more gas molecules are ionized to produce a larger $I_D$.

At $V_S$ of –750 V, the data points from $10^{-3}$ Torr to $10^{-4}$ Torr are used to fit the sensitivity $k$ for Equation (4-9). As previously discussed, the average electron trajectory with this $V_S$ is likely comparable to or longer than the mean free path of the gas molecule at these pressures and this allows efficient gas ionization. Therefore, the $I_D$ should be proportional to the pressure as the $I_D$ is not limited by the collision probability between the electrons and the gas molecules. As shown in Fig. 4-52, the fitted curve that has a sensitivity of 0.0206 A/Torr is linearly dependent on the pressure and matches reasonably well with the measured data points from $10^{-3}$ Torr down to 2 x $10^{-4}$ Torr. This indicates the gas ionization frequency of the gauge is proportional to the pressure over this range. For pressure from 2 x $10^{-4}$ Torr to 5 x $10^{-5}$ Torr, the fitted equation returns a value of $I_D$ slightly smaller than the measured $I_D$. At pressure higher than 2 x $10^{-4}$ Torr, the $I_D$ is high enough to cause significant voltage drop across the ballast resistor. For example, the $|V_K|$ is 618 V at $10^{-3}$ Torr when the $|V_S|$ is 750 V, but the $|V_K|$ is 739 V at 5 x $10^{-5}$ Torr, which is closer to the $|V_S|$. Note, the $k$ in Equation (4-9) is determined by the electric field, and the electrons gain higher kinetic energy in a stronger electric field [Red58]. Therefore, the fitted $k$ in Equation (4-9) is smaller than the actual $k$ value at pressure levels lower than 2 x $10^{-4}$ Torr, because the $|V_K|$ is closer to the $|V_S|$ to result in a stronger electric field when the gauge operates at pressure higher than 2 x $10^{-4}$ Torr. In other words, the fit over this entire range may improve if either the ballast resistor was removed from the circuit, or if a control scheme was used that fixed the $V_K$ regardless of $I_D$. For pressure lower than 5 x $10^{-5}$ Torr, the measured $I_D$ is smaller than the calculated $I_D$ from the fitted equation. This is expected, because the mean free path of the gas molecule increases to be comparable with the average electron trajectory to limit the collision probability between the electrons and the gas molecules and thus limit the $I_D$. Similar trends are observed for the fitted $k$ at other $|V_S|$. These $k$ values are summarized in Table 4-3.

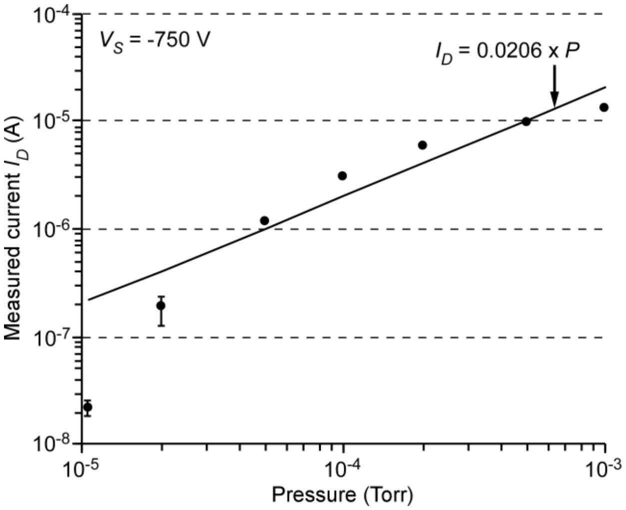

Figure 4-52: The measured current $I_D$ at various pressures for a $V_S$ of –750 V and the fitted curve. Unless specified by the error bars at plotted data points, the variations of measured $I_D$ are less than 2%.

Table 4-3: The fitted $k$ values at different $V_S$.

| $V_S$ (kV) | -0.75 | -1.00 | -1.25 | -1.50 |
|---|---|---|---|---|
| $k$ | 0.0206 | 0.0404 | 0.0612 | 0.0842 |
| $V_S$ (kV) | -1.75 | -2.00 | -2.50 | -3.00 |
| $k$ | 0.1115 | 0.1205 | 0.1437 | 0.1717 |

## 4.5 Summary and Conclusion

This work investigated the crossed-fields electron spiraling capabilities of seven preliminary CCG designs with the developed analytical approach. The Design P.C has the simplest structure that can be easily manufactured. The Design P.I.1 and Design P.I.2 integrate the gauge case and magnetic circuit, which promote the gauge integration to the next level. However, these three designs can hardly spiral electrons infinitely within the compact gauge space according to the simulation results. The Design P.A is innovative in utilizing an array of anode perforations and an asymmetrical magnetic field for electron spiraling, but the spiraling pattern is asymmetrical and can only happen under limited pre-conditions in the simulations, which is risky. The rest of the three evaluated designs – Design P.F, Design P.E and Design M.O – have the best resulting electron spiraling performance from the simulation results; however, the incompatibility of the manufacturability of components associated with these designs impedes their integration to the CDGs. To address the disadvantages and adapt the advantages of all the preliminary designs, three Penning cell gauge designs and a magnetron gauge design are finalized with refined geometries and fabrication processes to meet the manufacturing requirements of the CDGs. Design P.MF.1 has an internal volume of 1.1 $cm^3$ and can initiate infinite electron spiraling when the anode is biased at 900 V, according to the simulation results. Design M.MF has an even smaller internal volume of 0.4 $cm^3$ and can initiate infinite electron spiraling at a 500 V potential difference between the anode and the cathode in the simulation model. All four designs are constructed much smaller than the commercially available CCGs to enable the pressure monitoring of the reference vacuum in the CDGs. A magnetron design (Design M.S) is refined from Design M.MF and fabricated by 3D printing techniques, and is capable of being mounted on a standard vacuum feedthrough. Repeatable current $I_D$ versus pressure characteristics of the Design M.S at various supplied voltages $V_S$ were measured. The gauge started at a pressure as low as 10.5 µTorr when the $V_S$ was –750 V, and the gauge startup pressure $P_s$ increased with the $V_S$. At a specific $V_S$, the $I_D$ had a fixed sensitivity $k$ to the pressure, except at pressure levels near to the associated $P_s$ where the gas ionization collisions were limited by the collision probability between the electron and the gas molecules.

# CHAPTER 5:

## CONCLUSIONS AND FUTURE WORK

### 5.1 Conclusions and Major Contributions

This chapter concludes the efforts to develop miniaturized RF electron traps and cold cathode gauges (CCGs) for microsystems that require a high vacuum or ultra-high vacuum environment. Major contributions of each research effort are summarized. Future work toward the pumping demonstration with the enhanced-efficiency electron trapping module ($E^3$TM) and startup assistance for the miniaturized CCGs is proposed.

### 5.1.1 Miniaturized RF Electron Traps

The first-generation RF electron trap, the electron trapping module (ETM), demonstrates the RF electron trapping at centimeter scale. At a transmitted RF power of 0.033 W and RF frequency of 143.6 MHz, the estimated electron density is approximately $3 \times 10^5$ $cm^{-3}$ near the walls of the trapping region with the measured steady state electrode potential, which is 1000x higher than the electron density in the electron beam. One big advantage of such an RF electron trap is that it can elongate the electron pathway without using the magnetic field, which is the basis for the miniaturized magnet-less ion pump with fewer long-lived electrons that was introduced in Chapter 1. The major contributions of the ETM work include the proof-of-concept results of the ETM in demonstrating RF electron trapping, the development of an analytical model for modeling the electron trajectory in an RF electron trap, and the development of a DC blocking electrode testing scheme for characterizing electron density.

The second-generation RF electron trap, the $E^3$TM, demonstrates a higher RF electron trapping efficiency than the ETM. At a transmitted RF power of 0.273 W and an operating RF frequency of 96.9 MHz, the estimated electron density is $2.24 \times 10^6$ $cm^{-3}$ in the trap based on the measured steady state probe potential, which is 10x higher than the estimated peak electron density in the ETM. Major contributions of the $E^3$TM include following. First, the $E^3$TM utilizes finely perforated electrodes and micromachined parts, which results in a higher trap-to-device volume ratio and less parasitic. Second, the simple RF characteristics of the $E^3$TM enable the tunability of the operation frequency. Third, the $E^3$TM is structurally feasible for a gas pumping demonstration as it is configured in a full ion pump structure in terms of electrode composition and materials selection.

In summary, there are two guiding principles that can benefit the future developments and investigations of the RF electron traps. First, symmetric trap geometries, smooth and micro-perforated electrodes, and minimal utilization of non-conductive materials are highly preferred to achieve a more uniform RF electric field in the trapping region for better RF electron trapping efficiency. Second, the trap structure and the device has to be designed with RF operation in mind to reduce the unwanted parasitics for simple RF characteristics and low power operations.

### 5.1.2 Miniaturized Cold Cathode Gauges

A total of seven preliminary CCG designs are investigated in this work. With the developed analytical approach, the electric and magnetic fields of each design are analyzed to simulate the electron trajectory. Four designs are refined based on the designs that have the best electron spiraling capability, while the manufacturability and volume advantages from other designs are adapted into these refined designs. Design P.MF.1 (Penning cell gauge) has an internal volume of 1.1 $cm^3$, and the electron spiraling starts at an anode voltage of 900 V, as suggested by the simulation results. To meet potential additional volume constraints of Design P.MF.1, the magnetic circuit is adjustable (Design P.MF.2) and further miniaturization of the gauge (Design. P.MF.3) is also feasible without sacrificing its electron spiraling capability. Design M.MF (magnetron gauge) has an internal volume of 0.4 $cm^3$. The electron spiraling starts at a cathode voltage of –500 V, according to the simulation results. Similar to the structure of the Design M.MF, a magnetron design (Design M.S) is fabricated with advanced 3D printing technologies. The Design M.S can start at a pressure as low as 10.5 μTorr at a supply voltage $V_S$ of –750 V, and has a repeatable gauge current up to 1 mTorr at $V_S$ from –750 V to –3000 V. Assessment of all proposed designs are summarized in Table 5-1. The major contributions of this work are as follows. First, all CCG designs are at least 10x smaller than the commercially available CCGs. Second, a Multiphysics model is developed for simulating the electric and magnetic fields, and is capable of analyzing the electron trajectory as well. Third, the manufacturability of the designs is well considered. The fabrication processes of CCGs are compatible with the fabrication processes of CDG; the material composition of the CCG designs allow an appropriately cascaded vacuum seal, and the magnetic material has anti-corrosion properties.

Table 5-1: Assessment of the investigated CCG designs.

| | Name | Performance rating (4-point scale with 4 being the best) | | | |
|---|---|---|---|---|---|
| | | Electron spiraling | Manufacturability | Volume | Overall |
| Preliminary designs | Penning cell (Design P.C) | 1.5 | 4 | 3 | 2.5 |
| | Penning cell (Design P.I.1, Design P.I.2) | 1 | 2 | 3 | 2.0 |
| | Penning cell (Design P.A) | 2 | 2 | 2 | 2.0 |
| | Penning cell (Design P.F) | 4 | 2 | 4 | 3.0 |
| | Penning cell (Design P.E) | 4 | 1 | 3 | 2.5 |
| | Magnetron (Design M.O) | 4 | 3 | 3 | 3.5 |
| Refined designs | Penning cell (Design P.MF.1, Design P.MF.2) | 4 | 3 | 3 | 3.5 |
| | Penning cell (Design P.MF.3) | 4 | 3 | 4 | 3.5 |
| | Magnetron (Design M.MF) | 4 | 3.5 | 3.5 | 3.7 |
| | Magnetron (Design M.S) | 4 | 3.5 | 4 | 3.8 |

From the analysis in this work and other research efforts from the literatures, the magnetron or the inverted magnetron CCGs have a lower operating pressure than the Penning cell CCG. This observation is useful in guiding future work. Additionally, it has been observed that the gauge is preferred to have axisymmetric geometry along the anode axis and to have concentrically-aligned anode and cathode. This guiding principle is valuable for gauge developments in the future, because such gauge structures allow more gauge volume to be covered in crossed electric and magnetic fields for higher efficiency electron spiraling. Note that the analytical approach described in section 4.1.1 is solely used to model the trajectory of a single electron in the CCG designs. To allow the analysis of more complicated gauge behaviors or responses, such as dynamic range and current versus pressure relations, a plasma model that considers electron-electron and electron-gas particle interactions is preferred.

## 5.2 Future Work

### 5.2.1 Pumping Demonstration with the E$^3$TM

As noted in Chapter 3, the E$^3$TM – along with the electron source – contains all of the components necessary to demonstrate gas pumping via the proposed magnet-less ion pump concept that is discussed in Chapter 1. However, there are additional requirements to be met for gas pumping demonstrations in the future. First, further adjustments of the vacuum setup are required as the chamber needs to be isolated from other vacuum pumps during the testing. A 1.33" CF gate valve needs to be placed between the reducer and the 1.33" CF vacuum chamber to allow the isolation of the small vacuum chamber. A miniature ion gauge with a 1.33" CF flange is required for continuous chamber pressure monitoring. The probe should be removed and the associated feedthrough flange should be replaced with a blank flange to further minimize disturbance to the RF electron trap. Heating tape can be wrapped around the chamber and associated vacuum components to de-gas before the isolation from the commercial vacuum pumps. Second, as described in Chapter 1, the operation of the RFT-CHIP consists of two consecutive steps: gas ionization and gas pumping. The pulsed DC approach to achieving this operation with the E$^3$TM is conceptually shown in Fig. 5-1. For the first 98% of a duty cycle, the E$^3$TM will utilize the established RF electron trap to ionize gas molecules via the application of an RF electric field. Then, the high-power RF switch will switch from J1 to J2 to bias the bottom RF electrode to a negative high DC voltage for accelerating and burying the ionized gas molecules. The E$^3$TM will operate under this pulsed DC approach for a long period of time (~10 hours) in the isolated vacuum chamber to record the chamber pressure over time.

The pumping speed of the E$^3$TM can be calculated by comparing the pressure data to a control experiment in which the E$^3$TM is not RF or DC powered.

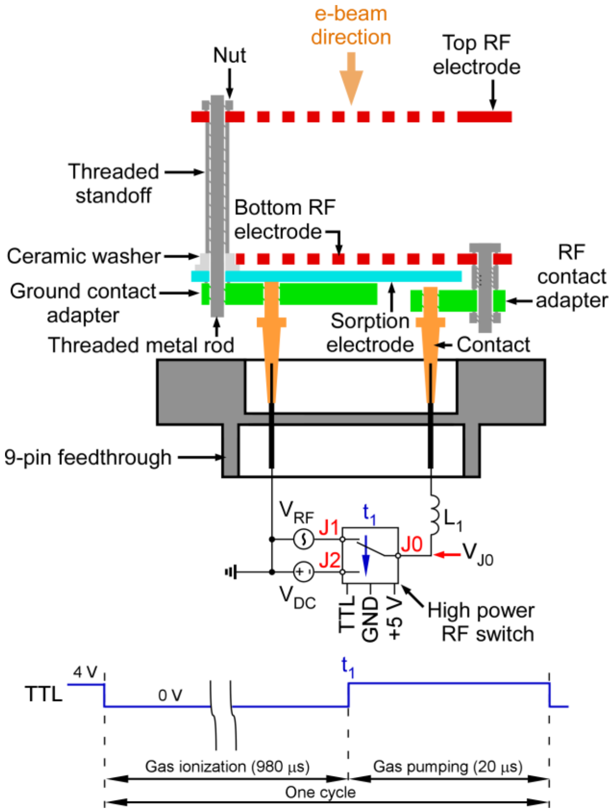

Figure 5-1: Pumping cycle of the E$^3$TM. The E$^3$TM is RF powered to trap the electrons for gas ionization in the first 98% of a cycle, followed by switching the RF switch from J1 to J2, which negatively biases the bottom RF electrode to a DC voltage to accelerate and bury the ions for gas pumping.

### 5.2.2 Startup Assistance in the CCGs

A startup delay has been documented as an issue for magnetron and inverted magnetron gauges since their invention in the late 1950s [Dus62]. In order to evaluate the potential magnitude of this issue in the proposed miniaturized CCGs, the relevant literature is first summarized here. Then, a plan is proposed to address this issue for the miniaturized CCGs. One parameter that is useful in assessing the results is the pressure-startup-delay product (PSDP), typically in units of Pa-s (nTorr-s). A lower value of PSDP indicates a faster startup at a given pressure. This parameter is not always explicitly reported, but if the parameter is possible to calculate from the results, it is reported here.

First investigations with 30 mm diameter inverted magnetron gauges showed a startup lag of about 10 minutes at pressures of $10^{-12}$ Torr (PSDP of $\approx$0.8 x $10^{-7}$ Pa-s, or $\approx$0.6 nTorr-s) [Red58]. The cross-sectional structure of an inverted magnetron gauge has a similar structure to a magnetron gauge except with the anode and cathode exchanged, as shown in Fig. 5-2 [Ken00]. Subsequent investigations with magnetron gauges (30 mm diameter, 15 mm length) indicated startup delays on the order of minutes at 1.5 nTorr (PSDP of ~130 x $10^{-7}$ Pa-s, or ~100 nTorr-s) [Las68]. The dependence of the startup delay upon the applied voltage – up to a decade of startup delay increase for a reduction in anode voltage from 1500 V to 1300 V – was also reported [Las68]. These studies were conducted with mercury lamps illuminating on the device in order to reduce the startup delay via a photoelectric emission effect, or by localized surface gas release due to heating.

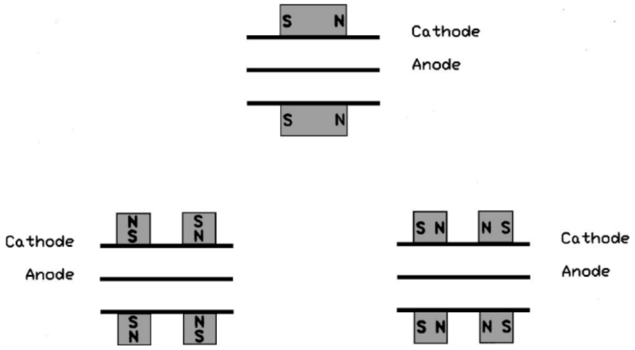

Figure 5-2: Cross-sections of inverted magnetron gauge structures (top) and double inverted magnetron gauge structures (bottom) [Ken00]. Spacers, yokes, and shims are omitted.

For configurations where the Penning cell is used as a pump rather than a gauge, a theoretical model was developed for startup delay [Che69]. The size of the Penning cell studied was not described in [Che69], but the cells likely were on the order of 30 mm in diameter and length. A grid/mesh cathode structure was utilized, which may aid in field emission (and thus reduce startup delays). Experimentally, it was found that a starting delay of about 100-300 seconds was typical at $10^{-11}$ Torr (PSDP of $1.3 \times 10^{-7}$ to $4 \times 10^{-7}$ Pa-s, or 1-3 nTorr-s) [Che69]. As anticipated by the presented theoretical model, the starting delay was found to be inversely proportional to the pressure for a given applied voltage. The investigators also found a rapid increase in starting delay for a relatively small decrease in applied voltage – for instance, changing the applied voltage from 5 kV to 4 kV increased the starting delay by a factor of 10.

More recent work also investigated Penning cell discharge formation at low pressures, including the use of a “triggering pin” [Kag84]. The dimensions of the anode in this cell were 10 mm diameter, and 10 mm length, with a 1 mm gap between the anode and each cathode. The “triggering pin” was a 0.2 mm diameter by 1 mm long tungsten pin attached to one cathode, concentric with the anode. Pressures in this study were as low as 15 nTorr, and the product of pressure and startup delay was $2 \times 10^{-7}$ Pa-s (1.5 nTorr-s). The authors indicated that devices without the “triggering pin” had more variability in startup delay, and in particular required higher voltages (up to 10 kV) for “orderly” startup delays.

A more recent study of magnetron and inverted magnetron gauges was performed with the specific intent of evaluating startup delays at low pressures and with various starting devices (radiation, field emission, photoelectric emission) [Ken96]. Gauges used in this study were of the typical Redhead gauge dimensions – 30 mm in diameter, 15 mm in length. This study found that, in the absence of any starting device, a basic "double inverted magnetron" gauge (Fig. 5-2) took about 2000 seconds to start at 1 nTorr of pressure, and around 200 seconds at 100 nTorr of pressure (PSDP of $3 \times 10^{-4}$ Pa-s to $3 \times 10^{-3}$ Pa-s, or 2-20 μTorr-s). With an "igniter" – described as thin, sharp-edged washers mounted on the anodes just outside the discharge areas – the starting delays were typically reduced by an order of magnitude at any pressure (PSDP of $3 \times 10^{-5}$ Pa-s to $3 \times 10^{-4}$ Pa-s, or 0.2-2 μTorr-s). The authors also found that the ion current versus time characteristics could be described by two periods – a dormant period initially, where the ion current was not measurable, followed by a growth period of exponential increase with a time constant inversely proportional to pressure. For gauges without igniters, the dormant period varied significantly from turn-on to turn-on and dominated the overall starting time at low pressures. Meanwhile, the growth period was repeatable for all gauges, and on the order of a few 10s of seconds at the lowest pressures ($10^{-10}$ Torr). This indicates that the ignition at the lowest pressures is reliant upon random processes such as background radiation ionization.

A set of compact cold-cathode (double inverted magnetron) gauges were studied in [Ken00] (Fig. 5-2). Cathode internal diameters were 13-16 mm and anodes ranged from 1.5 to 6 mm in diameter (2.5 mm diameter anodes were typically used). For these gauges, a typical product of starting delay and pressure ranged from $0.13 \times 10^{-4}$ Pa-s to $16 \times 10^{-4}$ Pa-s (0.1 to 12 μTorr-s), depending on operating voltage (2 kV to 4 kV, with smaller products at the larger voltages). Pressures of $10^{-10}$ were measurable, as long as the applied flux density was 0.09 T or higher (larger magnetic fields significantly reduced the starting delay-pressure product: an increase from 0.1 T to 0.14 T reduced the starting delay-pressure product by a factor of 20).

In summary, the literature indicates that starting delays are inversely proportional to pressure for cold cathode gauges of all types (Penning cell, magnetron, inverted magnetron, double inverted magnetron). Increasing the operating voltage and/or magnetic flux density tends to significantly reduce starting times. Though comparisons of dimensional scaling effects on startup time are sparse, there is some evidence between [Ken96] and [Ken00] that halving the gauge diameter does not significantly affect the starting delay-pressure product. While the more compact gauges operated at $10^{-10}$ Torr with sufficient operating voltage and flux density, the starting delays were on the order of a few hours – not an acceptable time frame for the application studied here. In all literature examining "starting devices", such devices typically reduced the starting delays to 10s of seconds even at the lowest measurable pressures.

To reduce startup delays, a field emitter array is proposed to be integrated with miniaturized CCGs in the future. For example, a microfabricated field emitter array could be placed near the edge of the bottom cathode endplate in Design M.MF (Fig. 5-3). The electric field near these lithographically patterned sharp metal tips (20 nm radius) is at least 500x the electric field between the cathode and the anode, which allows electrons to be emitted via field emissions. Detailed future efforts include the design and fabrication of the field emitter array, and the integration of the field emitter array into the miniaturized CCGs.

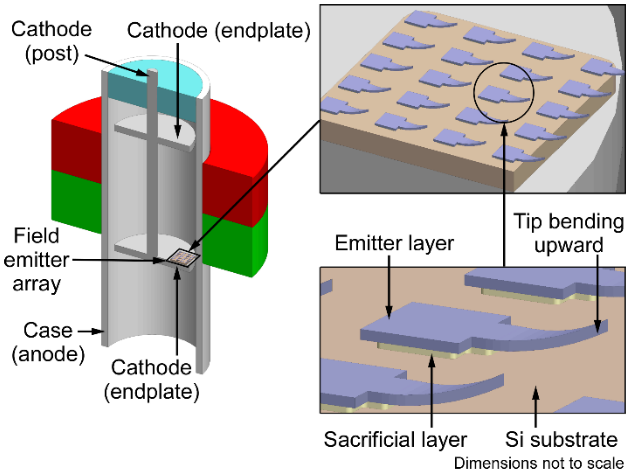

Figure 5-3: Design M.MF with the integrated, microfabricated field emitter array to address the potential startup delay issue.

# APPENDIX A DRAWINGS AND PARTS LISTS

Table A-1: Commercially available parts used to build the ETM.

| Name | Supplier | P/N | Product information |
|---|---|---|---|
| Screw | McMASTER-CARR® | 92196A060 | 18-8 stainless steel socket head cap screw, thread size: 0-80, length: 1’’ |
| Split lock washer | McMASTER-CARR® | 92146A510 | type 18-8 stainless steel, ID: 0.062’’, OD: 0.137’’, thickness: 0.015’’, screw Size: No. 0 |
| Nut | McMASTER-CARR® | 90480A001 | 18-8 stainless steel, thread size: 0-80, width: 5/32’’, height: 3/64’’ |
| Ceramic washer | McMASTER-CARR® | 94610A205 | Macor®, ID: 0.068", OD: 0.188", thickness: 0.025" |

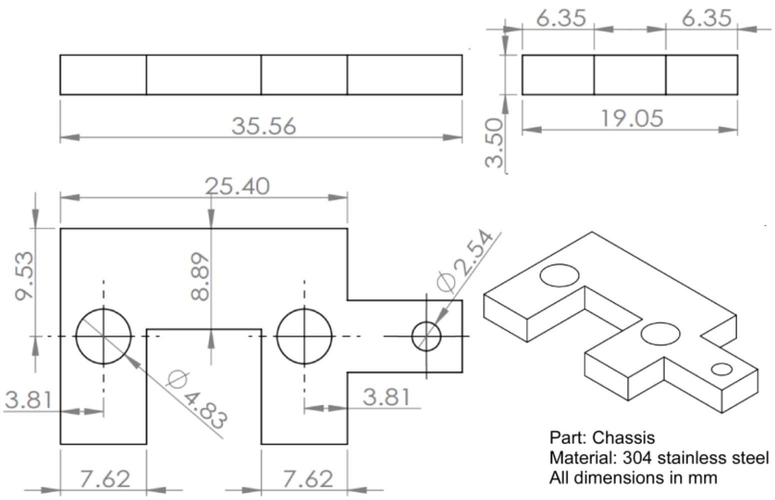

Part: Chassis
Material: 304 stainless steel
All dimensions in mm

Figure A-1: Chassis of the ETM.

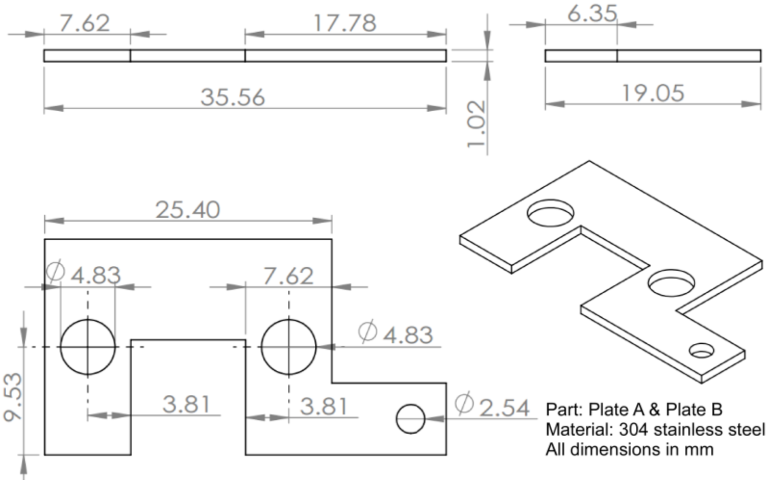

Figure A-2: Plate A and Plate B of the ETM.

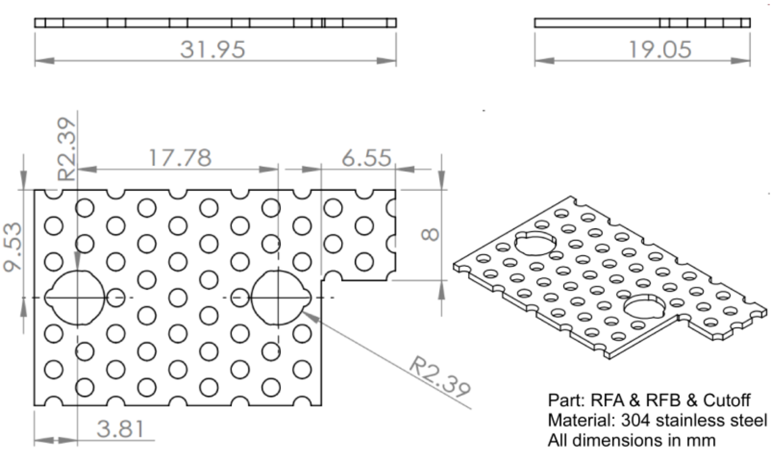

Figure A-3: RFA, RFB, and Cutoff electrode of the ETM.

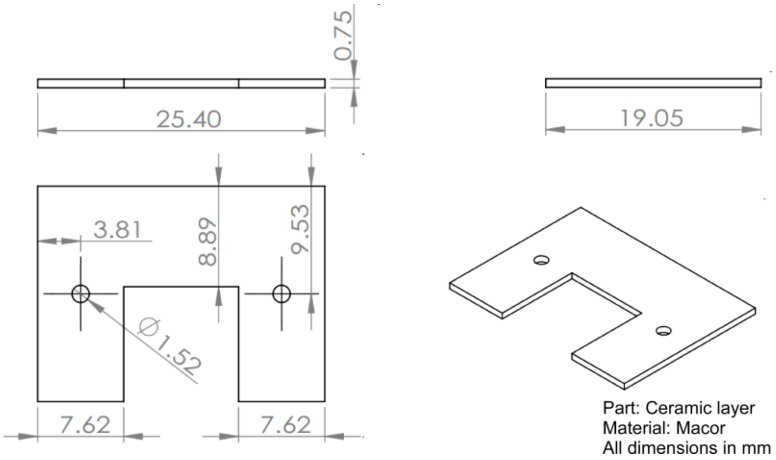

Figure A-4: U-shaped ceramic layer in the ETM.

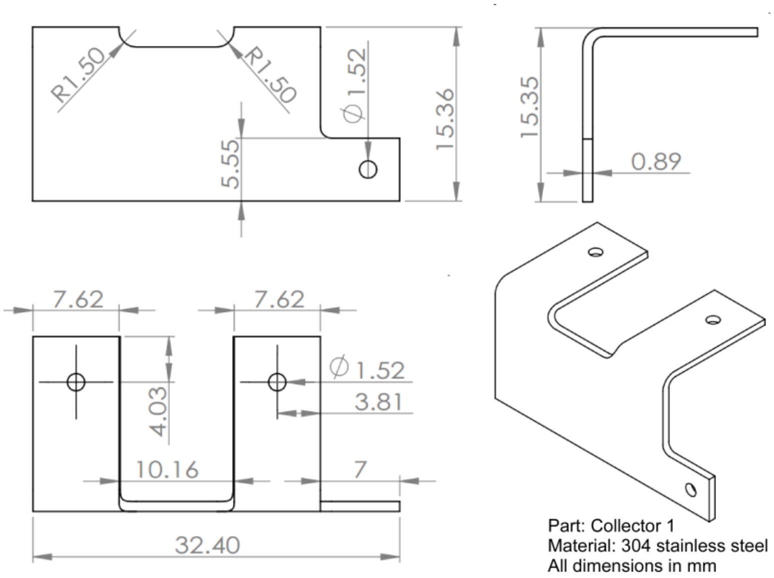

Part: Collector 1
Material: 304 stainless steel
All dimensions in mm

Figure A-5: Collector 1 of the ETM.

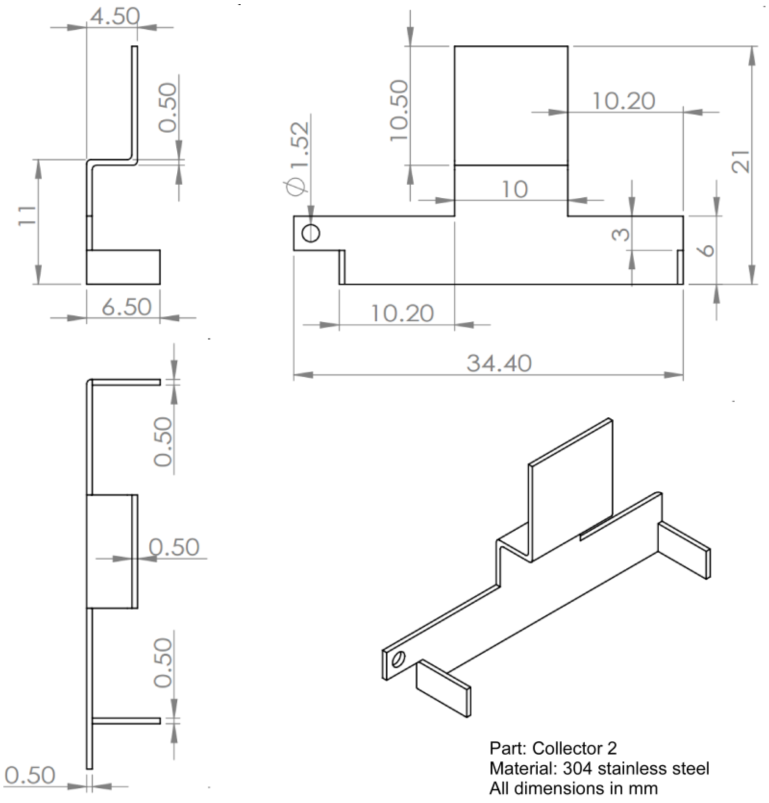

Part: Collector 2
Material: 304 stainless steel
All dimensions in mm

Figure A-6: Collector 2 of the ETM.

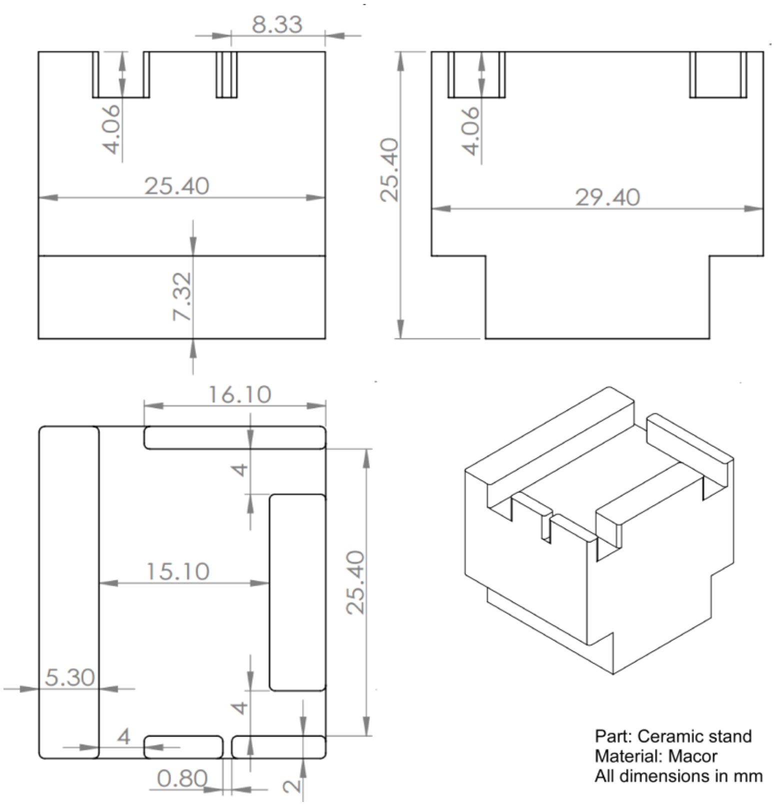

Part: Ceramic stand
Material: Macor
All dimensions in mm

Figure A-7: Ceramic stand of the ETM.

Table A-2: Commercially available parts used to build the E$^3$TM.

| Name | Supplier | P/N | Product information |
|---|---|---|---|
| Spring washer | McMASTER-CARR | 92146A510 | 18-8 stainless steel, #0 screw size (0.062"), ID: 0.062", OD: 0.137" |
| Threaded metal rod | McMASTER-CARR | 95412A898 | 18-8 stainless steel, #0-80 thread (0.06"), length: 0.5" |
| Hex nut (#0-80) | McMASTER-CARR | 90730A001 | 18-8 stainless steel, #0-80 thread (0.06"), width: 1/8", thickness: 3/64" |
| Tapped standoff | McMASTER-CARR | 91125A009 | 18-8 stainless steel, #0-80 thread (0.06"), OD: 0.125", length: 0.25" |
| Ceramic washer | McMASTER-CARR | 94610A205 | Macor®, ID: 0.068", OD: 0.188", thickness: 0.025" |
| Acetal rod | McMASTER-CARR | 8497K11 | diameter: 1/8", length: 4 ft, color: white |
| #000-120 screw | McMASTER-CARR | 90910A600 | 18-8 stainless steel, #000-120 thread (0.034"), length: 0.125" |
| Hex nut (#000-120) | McMASTER-CARR | 90001A302 | 18-8 stainless steel, #000-120 thread (0.034"), width: 5/64", thickness: 1/32 |
| Contact | Accu-Glass | 110909 | Au plated copper alloy, accepts 0.04" pin, ID of crimp barrel: 0.023", OD of crimp barrel: 0.07" |

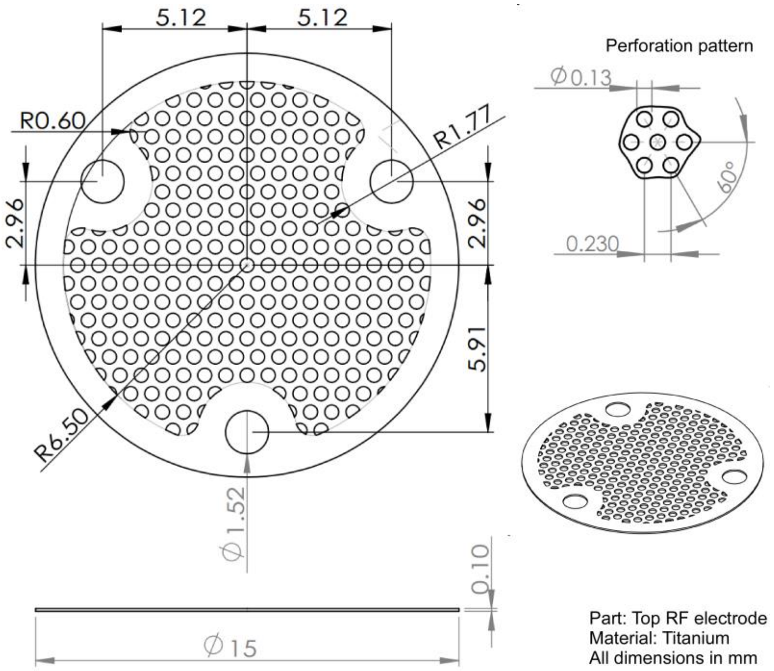

Figure A-8: Top RF electrode of the E$^3$TM.

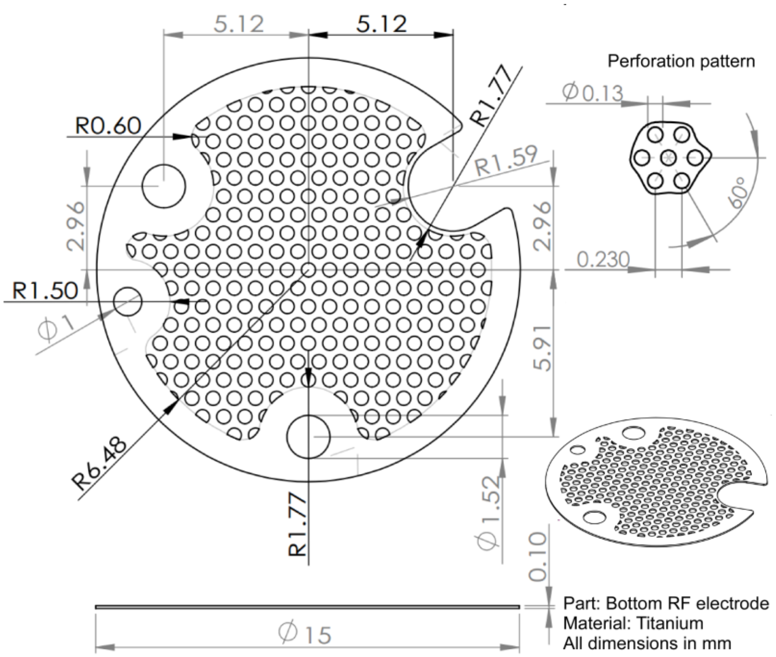

Figure A-9: Bottom RF electrode of the E$^3$TM.

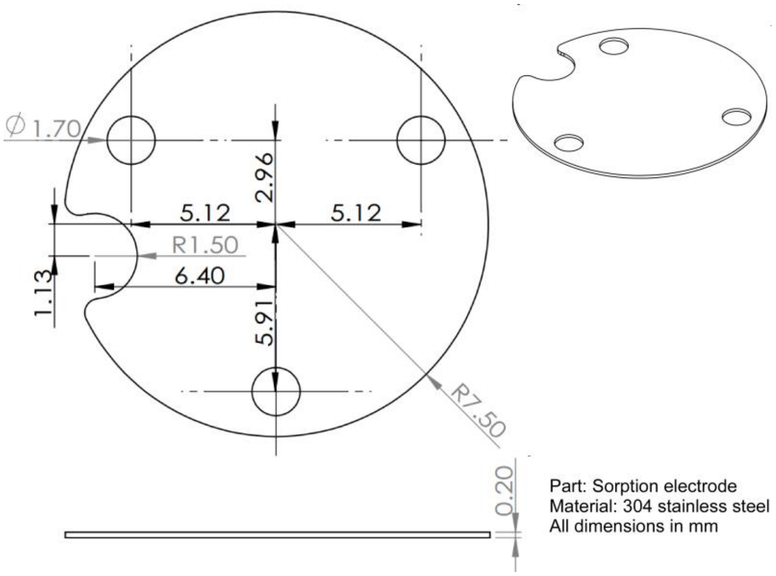

Part: Sorption electrode
Material: 304 stainless steel
All dimensions in mm

Figure A-10: Sorption electrode of the E$^3$TM.

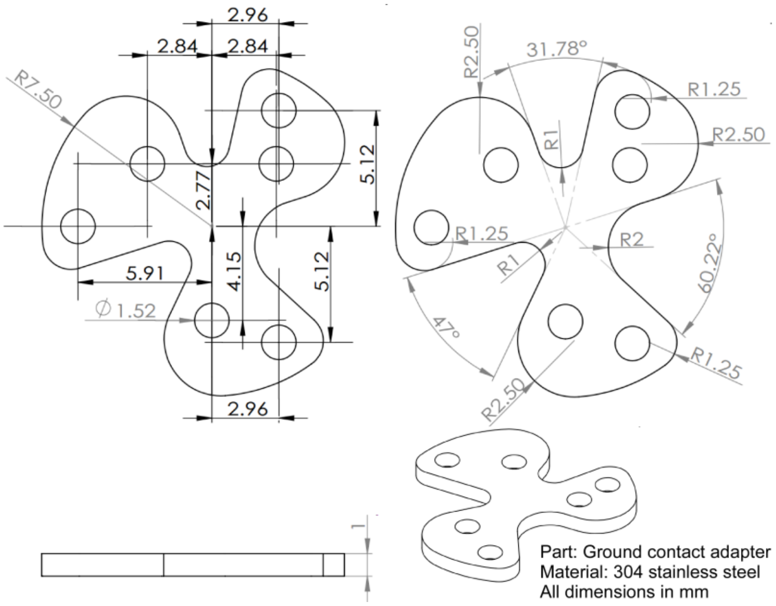

Part: Ground contact adapter
Material: 304 stainless steel
All dimensions in mm

Figure A-11: Ground contact adapter of the E$^3$TM.

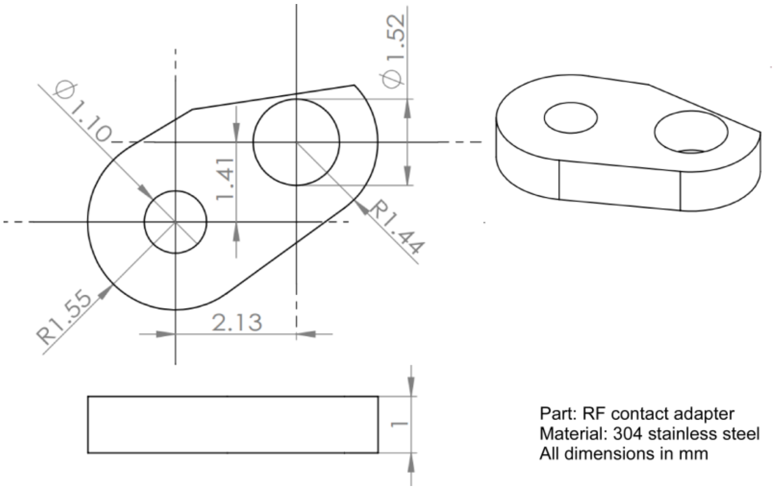

Part: RF contact adapter
Material: 304 stainless steel
All dimensions in mm

Figure A-12: RF contact adapter of the E$^3$TM.

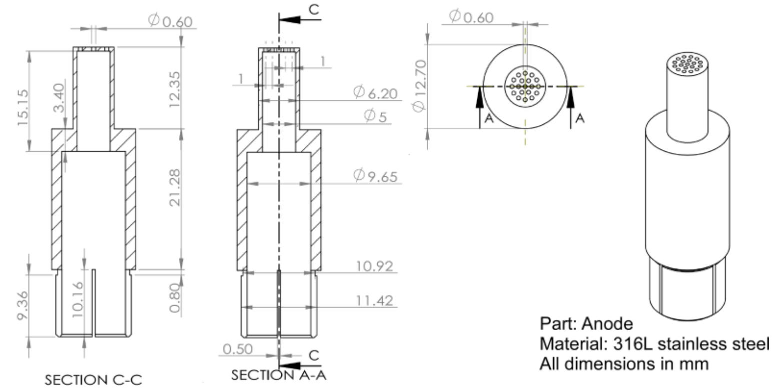

Part: Anode
Material: 316L stainless steel
All dimensions in mm

Figure A-13: Anode of Design M.S.

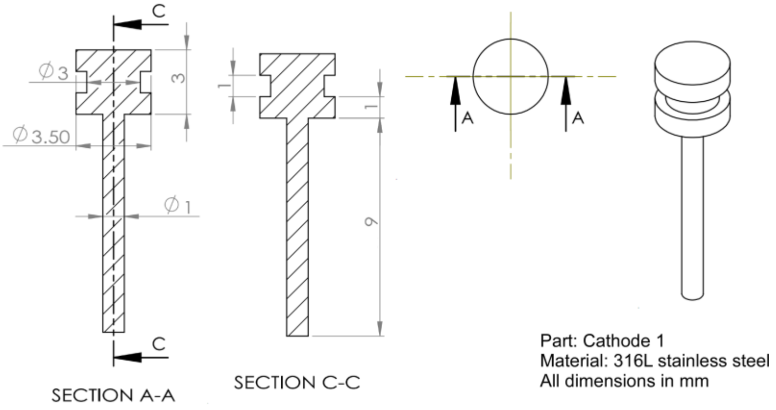

Part: Cathode 1
Material: 316L stainless steel
All dimensions in mm

Figure A-14: Cathode 1 of Design M.S.

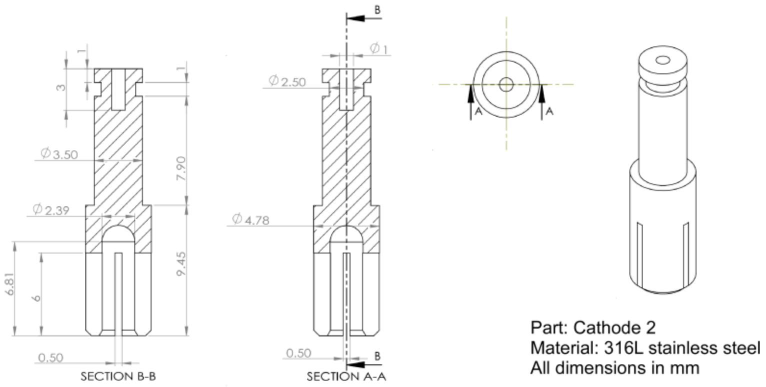

Part: Cathode 2
Material: 316L stainless steel
All dimensions in mm

Figure A-15: Cathode 2 of Design M.S.

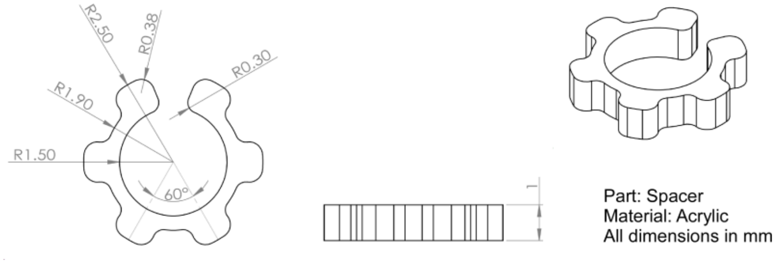

Part: Spacer
Material: Acrylic
All dimensions in mm

Figure A-16: Spacer of Design M.S.

# REFERENCES

[Abo12] S. N. Abolmasov, "Physics and engineering of crossed-field discharge devices," *Plasma Sources Science and Technology*, Vol. 21, No. 3 pp. 035006, 2012.

[Acc17] Accu-Glass Circular 9-Pin Feedthrough. [Online].

https://accuglassproducts.com/product.php?productid=16160, Accessed Jul. 2017.

[Acr17] Overview of materials for Acrylic. [Online].

http://www.matweb.com/search/datasheet.aspx?bassnum=O1303, Accessed Jul. 2017.

[An14] S. An, N. K. Gupta, Y. B. Gianchandani, "A Si-micromachined 162-stage two-part Knudsen pump for on-chip vacuum," *Journal of Microelectromechanical Systems*, Vol. 23, pp. 406-416, 2014.

[Aud87] M. Audi, M. de Simon, "Ion pumps," *Vacuum*, Vol. 37, No. 8-9, pp. 629-636, 1987.

[Bas16] A. Basu, and L. F. Velásquez-García, "An electrostatic ion pump with nanostructured Si field emission electron source and Ti particle collectors for supporting an ultra-high vacuum in miniaturized atom interferometry systems," *Journal of Micromechanics and Microengineering*, Vol. 26, No. 12, p.124003, 2016.

[Bay50] R. T. Bayard, and D. Alpert, "Extension of the low pressure range of the ionization gauge," *Review of Scientific Instruments*, Vol. 21, No. 6, pp. 571-572, 1950.

[Bes12] A. Besharatian, K. Kumar, R. L. Peterson, L. P. Bernal, K. Najafi, "A Scalable, Modular, Multi-stage, Peristaltic, Electrostatic Gas Micro-pump," *IEEE International Conference on Micro Electro Mechanical Systems (MEMS)*, Paris, France, pp. 1001-1004, 2012.

[Bid17] Bi-directional Coupler. [Online].

https://www.minicircuits.com/pdfs/ZFBDC20-62HP+.pdf, Accessed Jul. 2017.

[Bor02] C. Borde, "Atomic Clocks and Inertial Sensors," *Metrologia*, Vol. 39, pp. 435-463, 2002.

[Boz93] R. M. Bozorth, *Ferromagnetism*, Wiley-IEEE Press, 1993.

[Bra06] J. R. Brauer, *Magnetic Actuators and Sensors*, John Wiley & Sons, 2006.

[Can06] B. Canuel, F. Leduc, D. Holleville, A. Gauguet, A. Virdis, A. Clairon, and P. Bouyer, "Six-axis inertial sensor using cold-atom interferometry," *Physical review letters*, Vol. 97, No. 1: 010402, 2006.

[Cha05] J. Chae, B. H. Stark, and K. Najafi, "A micromachined Pirani gauge with dual heat sinks," *IEEE Transactions on Advanced Packaging*, Vol. 28, No. 4, pp. 619-625, 2005.

[Che69] L. de Chernatony, R. D. Craig, "The discharge mechanism in a magnetic ion pump," *Vacuum*, Vol. 19, No. 9, pp. 393-395, 1969.

[Chi11] F. C. Chiang, P. Pribyl, W. Gekelman, B. Lefebvre, L. Chen, and J. W. Judy, " Microfabricated flexible electrodes for multiaxis sensing in the large plasma device at UCLA," *IEEE Trans. Plasma Sci.*, Vol. 39, No. 6, pp. 1507-1515, 2011.

[Chi14] E. F. C. Chimamkpam, E. S. Field, A. I. Akinwande, and L. F. Velasquez-Garcia, " Resilient batch-fabricated planar arrays of miniaturized Langmuir probes for real-time measurement of plasma potential fluctuations in the HF to microwave frequency range," *J. Microelectromech. Syst.*, Vol. 23, No. 5, pp. 1131-1139, 2014.

[COM17] COMSOL AC/DC module user's guide. [Online].

http://www.lmn.pub.ro/~daniel/ElectromagneticModelingDoctoral/Books/COMSOL4.3/acdc/ACDCModuleUsersGuide.pdf, Accessed Jul. 2017.

[Del16] A. Dellis, V. Shah, E. Donley, S. Knappe, J. Kitching, "Low helium permeation cells for atomic microsystems technology," *Optics Letters*, Vol. 41, No. 12, pp. 2775-2778, 2016.

[Del17] DELRIN® Acetal Homopolymer datasheet. [Online].

http://www.sdplastics.com/delrin/delrin[1].pdf, Accessed Jul. 2017.

[Den17] S. Deng, S. R. Green, A. H. Markosyan, M. J. Kushner, Y. B. Gianchandani, "*A Miniaturized Magnet-less RF Electron Trap: II. Experimental Verification*," *Journal of Vacuum Science and Technology B*, Vol.35, No.4, 2017.

[Dia10] S. Diaham, S. Zelmat, M-L. Locatelli, S. Dinculescu, M. Decup, and T. Lebey, "Dielectric breakdown of polyimide films: Area, thickness and temperature dependence," *IEEE Transactions on Dielectrics and Electrical Insulation*, Vol. 17, No. 1, pp. 18-27, 2010.

[DML17] Direct Metal Laser Sintering. [Online].

http://gpiprototype.com/services/dmls-direct-metal-laser-sintering.html, Accessed Jul. 2017.

[DUP17] DUPONT™ KAPTON® datasheet. [Online]

http://www.dupont.com/content/dam/dupont/products-and-services/membranes-and-films/polyimde-films/documents/DEC-Kapton-HN-datasheet.pdf, Accessed Jul. 2017.

[Dus62] S. Dushman, J. Lafferty (ed.), *Scientific Foundations of Vacuum Technique*, *2nd ed.*, John Wiley & Sons, London and New York; 1962.

[Els75] R. J. Elsey, "Outgassing of vacuum materials-II," *Vacuum*, Vol. 25, No. 8, pp. 347-361, 1975.

[Fer17] Ferran-Tech. [Online]. http://www.ferrantech.com/technology#product, Accessed Jul. 2017.

[Fom14] A. A. Fomani, L. F. Velásquez-García, and A. I. Akinwande, "Challenges of high vacuum pumping based on impact ionization and implantation processes," *27th International Vacuum Nanoelectronics Conference (IVNC)*, pp. 210-211, 2014.

[God02] V. A. Godyak, R. B. Piejak, and B. M. Alexandrovich, " Electron energy distribution function measurements and plasma parameters in inductively coupled argon plasma," *Plasma Sources Sci. Technol.*, Vol. 11, No. 4, pp. 525-543, 2002.

[Gor09] A. Górecka-Drzazga, "Miniature and MEMS-type vacuum sensors and pumps," *Vacuum*, Vol. 83, No. 12, pp. 1419-1426, 2009.

[Gra03] S. Graf, J. Sekler, K. Altwegg, L. Duvet, and U. Rohner, "COPS-a novel pressure gauge using MEMS devices for space," *Materials in a Space Environment*, Vol. 540, pp. 439-443, Sep. 2003.

[Gra91] I. S. Grant, and W. R. Phillips, *Electromagnetism, 2nd ed.*, Wiley, 1991.

[Gre13] S. R. Green, R. Malhotra, Y. B. Gianchandani, "Sub-Torr Chip-Scale Sputter-Ion Pump Based on a Penning Cell Array Architecture," *Journal of Microelectromechanical Systems*, Vol. 22, pp. 309-17, 2013.

[Grz14] T. Grzebyk, A. Górecka-Drzazga, J. A. Dziuban, "Glow-discharge ion-sorption micropump for vacuum MEMS," *Sensors and Actuators A*, Vol. 208, pp. 113-119, 2014.

[Grz16] T. Grzebyk, and A. Górecka-Drzazga, "MEMS type ionization vacuum sensor," *Sensors and Actuators A: Physical*, Vol. 246, pp. 148-155, 2016.

[Hal81] D. Halliday, R. Resnick, *Fundamentals of physics*, John Wiley & Sons, 1981.

[Hay11] W. H. Hayt, J. A. Buck, *Engineering Electromagnetics (8th ed.)*, McGraw-Hill, New York, NY; 2011.

[Hay16] W. M. Haynes, D. R. Lide, T. J. Bruno, *CRC Handbook of Chemistry and Physics, 97th ed.*, Taylor & Francis Group, Boca Raton, FL, 2016.

[Hel66] J. C. Helmer, and W. H. Hayward, "Ion Gauge for Vacuum Pressure Measurements below $1 \times 10^{-10}$ Torr," *Review of Scientific Instruments*, Vol. 37, No. 12, pp. 1652-1654, 1966.

[Hob58] J. P. Hobson, and P. A. Redhead, "Operation of an inverted-magnetron gauge in the pressure range $10^{-3}$ to $10^{-12}$ mm. Hg," *Canadian Journal of Physics*, Vol. 36, No. 3, pp. 271-288, 1958.

[Hob80] J. P. Hobson, "Performance of a combined magnetron pump-gauge at ultrahigh vacuum," *Surface Science*, Vol. 100, No. 1, pp. 273-280, 1980.

[Hum84] S. Humphries Jr, and C. S. Hwang, "Miniature Penning ionization gauge for pulsed gas measurements," *Review of Scientific Instruments*, Vol. 55, No. 10, pp. 1663-1665, 1984.

[Ins17] InstruTech® CCM501 Hornet™ cold cathode gauge. [Online].

http://www.instrutechinc.com/site/files/1082/124784/427504/756399/CCM501_Data_Sheet.pdf, Accessed Jul. 2017.

[Jau12] Y. Y. Jau, H. Partner, P. D. D. Schwindt, J. D. Prestage, J. R. Kellogg, and N. Yu, "Low-power, miniature $^{171}$Yb ion clock using an ultra-small vacuum package," *Applied Physics Letters.*, Vol. 101, No. 25, pp. 253518-1-4, 2012.

[Kag84] K. Kageyama, "Formative processes of cold-cathode Penning discharges at low pressures," *J. Appl. Phys.*, Vol. 55, No. 3, pp. 723-731, 1984.

[Ken96] B. R. F. Kendall, E. Drubetsky, "Starting delays in cold-cathode gauges at low pressures," *J. Vac. Sci. Tech. A*, Vol. 14, No. 3, pp. 1292-1296, 1996.

[Ken97] B. R. F. Kendall, and E. Drubetsky, "Cold cathode gauges for ultrahigh vacuum measurements," *Journal of Vacuum Science & Technology A: Vacuum, Surfaces, and Films*, Vol. 15, No. 3, pp. 740-746, 1997.

[Ken00] B. R. F. Kendall, and E. Drubetsky, "Compact wide-range cold-cathode gauges," *Journal of Vacuum Science & Technology A: Vacuum, Surfaces, and Films*, Vol. 18, No. 4, pp. 1724-1729, 2000.

[Kim09] B. Kim, R. N. Candler, R. Melamud, M. A. Hopcroft, S. Yoneoka, H. K. Lee, M. Agarwal, S. A. Chandorkar, G. Yama, and T. W. Kenny, "Hermeticity and diffusion investigation in polysilicon film encapsulation for microelectromechanical systems," *Journal of Applied Physics*, Vol. 105, No. 1, p. 013514, 2009.

[Kim17] Kimball Physics 1.33" spherical cube vacuum chamber. [Online].

http://www.kimballphysics.com/PDFs/mcf_specs_spherical_cubes.pdf, Accessed Jul. 2017.

[Kit11] J. Kitching, S. Knappe, E. Donley, "Atomic Sensors – A Review," *IEEE Sensors Journal*, Vol. 11, pp. 1749-1757, 2011.

[Kna08] S. Knappe, "3.18 - MEMS Atomic Clocks", in *Comprehensive Microsystems*, edited by Yogesh B. Gianchandani, Osamu Tabata and Hans Zappe, Elsevier, Oxford, pp. 571-612, 2008.

[Kna08-2] W. Knapp, D. Schleussner, and M. Wüest, "Investigation of ionization gauges with carbon nanotube (CNT) field-emitter cathodes," *Journal of Physics: Conference Series*, Vol. 100, No. 9, pp. 092007, 2008.

[Kob93] T. Kobayashi, H. Hojo, and M. Ono, "Pressure measurement from 1 atm to 0.01 Pa using a quartz oscillator," *Vacuum*, Vol. 44, No. 5-7, pp. 613-616, 1993.

[Kur17] Kurt J. Lesker® KJLC 423 series cold cathode gauges & 943 controller. [Online].

http://www.lesker.com/newweb/gauges/cold_cathode_kjlc_943.cfm, Accessed Jul. 2017.

[Kus09] M. J. Kushner, "Hybrid modelling of low temperature plasmas for fundamental investigations and equipment design," *Journal of Physics D*, Vol. 42, No. 19, p. 194013, 2009.

[Laf61] J. M. Lafferty, "Hot-Cathode Magnetron Ionization Gauge for the Measurement of Ultrahigh Vacua," *Journal of Applied Physics*, Vol. 32, No. 3, pp. 424-434, 1961.

[Las68] W. S. Lassiter, "Striking characteristics of the magnetron ionization gage in helium from 1.9 x $10^{-7}$ Torr to 7 x $10^{-10}$ Torr," NASA TN D-4681, Aug. 1968.

[Lie94] M. A. Lieberman, and A. J. Lichtenberg, *Principles of Plasma Discharges and Materials Processing*, John Wiley & Sons, New York, NY; 1994.

[Lie04] L. A. Liew, S. Knappe, J. Moreland, H. Robinson, L. Hollberg, and J. Kitching, "Microfabricated alkali atom vapor cells," *Applied Physics Letters*, Vol 84, pp. 2694-2696, 2004.

[LMR17] LMR-400 coax cable specifications. [Online].

https://www.timesmicrowave.com/documents/resources/LMR-400.pdf, Accessed Jul. 2017.

[Lut04] R. Lutwak, J. Deng, W. Riley, M. Varghese, J. Leblanc, G. Teplot, M. Mescher, D. Serkland, K. Geib, G. Peake, "The chip-scale atomic clock – Low-power physics package," *36th Annual Precise Time and Time Interval (PTTI) Meeting*, pp. 339-354, 2004.

[Ma15] Y. Ma, Y. Sui, T. Li, and Y. B. Gianchandani, "A Submillimeter Package for Microsystems in High-Pressure and High-Salinity Downhole Environments," *Journal of Microelectromechanical Systems*, Vol. 24, pp. 861-869, 2015.

[Mac16] Macor®. [Online].

http://glassfab.com/wp-content/uploads/2015/08/Corning-Macor.pdf, Accessed Jul. 2017.

[Mar17] A. H. Markosyan, S. R. Green, S. Deng, Y. B. Gianchandani and M. J. Kushner, "A Miniaturized Magnet-Less RF Electron Trap: I. Modeling and Analysis," *Journal of Vacuum Science and Technology B*, Vol.35, No. 4, 2017.

[Mas90] T. Masaki, K. Kawata, and T. Masuzawa, "Micro electro-discharge machining and its applications," *Proc. IEEE Micro Electro Mechanical Systems: An Investigation of Micro Structures, Sensors, Actuators, Machines and Robots*, Napa Valley, CA, Feb. 1990, pp. 21-26.

[Mau13] L. Mauri, E. Rizzi, M. Moraja, and M. Campaniello, "The discrete vacuum packaging reliability issue in MEMS," *2013 Microelectronics Packaging Conference (EMPC)*, pp. 1-4, 2013.

[Met51] G. H. Metson, "The physical basis of the residual vacuum characteristic of a thermionic valve," *British Journal of Applied Physics*, Vol. 2, No. 2, pp. 46-48, 1951.

[MKS17] MKS 903 inverted magnetron cold cathode vacuum transducer. [Online].

https://www.mksinst.com/docs/UR/903.pdf, Accessed Jul. 2017.

[Mou64] W. G. Mourad, T. Pauly, and R. G. Herb, "Orbitron ionization gauge," *Review of Scientific Instruments*, Vol. 35, No. 6, pp. 661-665, 1964.

[Mul09] T. Müller, M. Gilowski, M. Zaiser, P. Berg, C. Schubert, T. Wendrich, and E. M. Rasel, "A compact dual atom interferometer gyroscope based on laser-cooled rubidium," *The European Physical Journal D-Atomic, Molecular, Optical and Plasma Physics*, Vol. 53, No. 3, pp. 273-281, 2009.

[Nel12] K. Nelson, K. Salit, J. Kriz, D. Sandquist, and J. Sebby-Strabley, "Cold atom micro primary standard (CAMPS)," *Position Location and Navigation Symposium (PLANS), 2012 IEEE/ION*, pp. 1094-1098, 2012.

[Neo17] Neodymium Magnet Physical Properties. [Online].

https://www.kjmagnetics.com/specs.asp, Accessed Jul. 2017.

[Pan90] C. Pan, and H. Kelly, "Calculation of the electron-impact-ionization cross section of Helium including electron correlations," *Physical Review A*, Vol. 41, pp. 3624-3634, 1990.

[Pea90] N. T. Peacock, and R. N. Peacock, "The influence of the magnetic field strength upon the characteristic curve of a cold cathode ionization gauge," *Journal of Vacuum Science & Technology A: Vacuum, Surfaces, and Films*, Vol. 8, No. 3, pp. 2806-2809, 1990.

[Pea91] R. N. Peacock, N. T. Peacock, and D. S. Hauschulz, "Comparison of hot cathode and cold cathode ionization gauges," *Journal of Vacuum Science & Technology A: Vacuum, Surfaces, and Films*, Vol. 9, No. 3, pp. 1977-1985, 1991.

[Pen37] F.M. Penning, *Philips Technical Review*, Vol. 201, No. 2, 1937.

[Pen40] F. M. Penning, and N. V. Philips, "Method and device for measuring pressures," U.S. Patent 2197079, Apr. 1940.

[Pfe17] Pfeiffer Vacuum cold cathode gauge head IKR 050, FPM seal DN 25 ISO-KF. [Online].

https://static.pfeiffer-vacuum.com/productPdfs/PTR18500.en.pdf, Accessed Jul. 2017.

[Pho17] Photochemical Machining Process. [Online].

http://www.photofabrication.com/etching-process, Accessed Jul. 2017.

[Pri12] I. P. Prikhodko, S. A. Zotov, A. A. Trusov, and A. M. Shkel, "Foucault pendulum on a chip: Rate integrating silicon MEMS gyroscope," *Sensors and Actuators A: Physical*, Vol. 177, pp. 67-78, 2012.

[Pro17] ProJet® 3500 SD&HD Professional 3D Printers. [Online].

https://www.3dsystems.com/sites/default/files/projet_3500_plastic_0115_usen_web.pdf, Accessed Jul. 2017.

[Qia09] C. Qian, and W. W. Brey, "Impedance matching with an adjustable segmented transmission line," *Journal of Magnetic Resonance*, Vol. 199, pp. 104-110, 2009.

[Red03] P. A. Redhead, "Measurement of vacuum: 1950–2003," *Journal of Vacuum Science & Technology A: Vacuum, Surfaces, and Films*, Vol. 21, No. 5, pp. S1-S6, 2003.

[Red58] P. A. Redhead, "The Townsend discharge in a coaxial diode with axial magnetic field," *Canadian Journal of Physics*, Vol. 36, No. 3, pp. 255-270, 1958.

[Red59] P. A. Redhead, "The magnetron gauge: a cold-cathode vacuum gauge," *Canadian Journal of Physics*, Vol. 37, No. 11 pp.1260-1271, 1959.

[Red60] P. A. Redhead, "Modulated Bayard-Alpert Gauge," *Review of Scientific Instruments*, Vol. 31, No. 3, pp. 343-344, 1960.

[Red63] P. A. Redhead, "The effects of adsorbed oxygen on measurements with ionization gauges," *Vacuum*, Vol. 13, No. 7, pp. 253-258, 1963.

[Red65] P. A. Redhead, and J. P. Hobson, "Total pressure measurements below $10^{-10}$ torr with non-magnetic ionization gauges," *British Journal of Applied Physics*, Vol. 16, No. 10, pp. 1555-1565, 1965.

[Red66] P. A. Redhead, "New hot-filament ionization gauge with low residual current," *Journal of Vacuum Science and Technology*, Vol. 3, No. 4, pp. 173-180, 1966.

[RG17] RG 58 C/U coaxial cable datasheet. [Online].

https://www.pasternack.com/images/productpdf/rg58c-u.pdf, Accessed Jul. 2017.

[Sak94] G. L. Saksaganskii, *Getter and Getter-Ion Vacuum Pumps*, Harwood Academic, 1994.

[Sch12] D. R. Scherer, D. B. Fenner, J. M. Hensley, "Characterization of alkali metal dispensers and non-evaporable getter pumps in ultrahigh vacuum systems for cold atomic sensors," *Journal of Vacuum Science & Technology A*, Vol. 30, p. 061602, 2012.

[Sch14] D. R. Scherer, R. Lutwak, M. Mescher, R. Stoner, B. Timmons, F. Rogomentich, G. Tepolt, S. Mahnkopf, J. Noble, S. Chang, and D. Taylor, "Progress on a miniature cold-atom frequency standard," *The 46th Annual Precise Time and Time Interval Systems and Application Meeting*, pp. 154-163, 2014.

[Sch16] P. D. D. Schwindt, Y. Y. Jau, H. Partner, A. Casias, A. R. Wagner, M. Moorman, R. P. Manginell, J. R. Kellogg, and J. D. Prestage, "A highly miniaturized vacuum package for a trapped ion atomic clock," *Review of Scientific Instruments*, Vol. 87, No. 5: 053112, 2016.

[Sch67] W. Schuurman, "Investigation of a low pressure Penning discharge," *Physica*, Vol. 36, No. 1, pp. 136-160, 1967.

[Sch70] G. Schaumann, J. Völki, and G. Alefeld, "The diffusion coefficients of hydrogen and deuterium in vanadium, niobium, and tantalum by gorsky-effect measurements," *Physica Status Solidi (b)*, Vol. 42, No.1 pp. 401-413, 1970.

[Sei83] H. Seiler, "Secondary electron emission in the scanning electron microscope," *Journal of Applied Physics*, Vol. 54, No. 11, pp. R1-R18, 1983.

[Sgo06] S. Sgobba, "Materials for high vacuum technology, an overview," *CERN Technical Specification*, No. 004, pp. 117-143, 2006.

[Sma17] SmalTec EM203 Micro EDM Machine. [Online].

http://www.smaltec.com/resources/SmalTec_EM203_Specs.pdf, Accessed Jul. 2017.

[Spa03] D. Sparks, N. Najafi, S. Massoud-Ansari, "Chip-level vacuum packaging of micromachines using nanogetters," *IEEE Transactions on Advanced Packaging*, Vol. 26, pp. 277-282, 2003.

[Spa10] D. Sparks, N. Najafi, B. Newman, inventors; Integrated Sensing Systems, Inc., assignee; "Getter Device", U.S. patent 7,789,949. September 7, 2010.

[Spi91] C. A. Spindt, C. E. Holland, A. Rosengreen, and I. Brodie, "Field-emitter arrays for vacuum microelectronics," *IEEE Transactions on Electron Devices*, Vol. 38, No. 10, pp. 2355-2363, 1991.

[Sta16] Stainless Steel – Grade 304 (UNS S30400). [Online].

http://www.azom.com/article.aspx?ArticleID=965, Accessed Jul. 2017.

[Sto55] V. L. Stout, and M. D. Gibbons, "Gettering of gas by titanium," *Journal of applied physics*, Vol. 26, No. 12, pp. 1488-1492, 1955.

[Sug98] M. Sugawara, *Plasma Etching: Fundamentals and Applications*, Oxford University Press Inc., New York, NY; 1998.

[Tak02] K. Takahata, and Y. B. Gianchandani, "Batch mode micro-electro-discharge machining," *Journal of Microelectromechanical Systems*, Vol. 11, No. 02, pp. 102-110, 2002.

[Tip07] P. A. Tipler, and G. Mosca, *Physics for Scientists and Engineers,6th ed.*, W. H. Freeman and Company, New York, NY, 2007.

[Tru11] A. A. Trusov, A. R. Schofield, and A. M. Shkel, "Micromachined rate gyroscope architecture with ultra-high quality factor and improved mode ordering," *Sensors and Actuators A: Physical*, Vol. 165, No. 1 pp. 26-34, 2011.

[Ula15] F. T. Ulaby, and U. Ravaioli, *Fundamentals of Applied Electromagnetics, 7th ed.*, Pearson, Upper Saddle River, NJ, 2015.

[VAC17] VACOM® COLDION® product overview. [Online].

https://www.vacom.de/en/products/total-pressure-measurement/ionization-vacuum-gauge/cold-cathode-ionization-vacuum-gauge/1050-product-overview, Accessed Jul. 2017.

[Vel02] A. Vesel, and M. Mozetic, "Discharge characteristics of a magnetron cell in ultrahigh vacuum," *Vacuum*, Vol. 67, No. 3, pp. 629-633, 2002.

[Vel10] L. F. Velásquez-García, B. L. P. Gassend, and A. I. Akinwande, "CNT-based MEMS/NEMS gas ionizers for portable mass spectrometry applications," *Journal of Microelectromechanical Systems*, Vol. 19, No. 3, pp. 484-493, 2010.

[Wel01] K. M. Welch, *Capture Pumping Technology*, 2nd ed., Elsevier, 2001.

[Wil91] N. Wilson, and P. Bunch, "Magnetic permeability of stainless steel for use in accelerator beam transport systems," *IEEE Particle Accelerator Conference*, pp. 2322-2324, 1991.

[Wil04] S. Wilfert, and C. Edelmann, "Miniaturized vacuum gauges," *Journal of Vacuum Science & Technology A: Vacuum, Surfaces, and Films*, Vol. 22, No. 2, pp. 309-320, 2004.

[Wu12] G. Wu, D. Xu, B. Xiong, Y. Wang, Y. Ma, "Wafer-Level Vacuum Packaging for MEMS Resonators using Glass Frit Bonding," *Journal of Microelectromechanical Systems*, Vol. 21, No. 6, pp. 1484-1491, 2012.

[Zho11] H. Zhou, H.Q. Li, V. Sharma, and M.A. Schmidt, "A single-stage micromachined vacuum pump achieving 164 torr absolute pressure," *Proc. of IEEE Microelectromechanical Systems Conference 2011*, pp. 1095-1098, 2011.

[Zie03] F. Zielinski, J. M. Costantini, J. Haussy, and F. Durbin, "Helium depth profiling in tantalum after ion implantation and high-temperature annealing," *Journal of nuclear materials*, Vol. 312, No. 2, pp. 141-145, 2003.

[Zoo92] J. Zook, D. Burns, H. Guckel, J. Sniegowski, R. Engelstad, and Z. Feng, "Characteristics of polysilicon resonant microbeams," *Sensors and Actuators A*, Vol. 35, pp. 51-59, 1992